Transient reaction analysis for automotive catalyst

Yoshiyuki Sakamoto

Acknowledgements

Contents

Chapter 1 Introduction

1-1.Backgoroud

 The complexity of automotive catalysts is usually larger than that of other industrial catalysts in the both views of reaction and material (Figure 1). Automotive catalysts have to purify harmful exhaust gases involving nitrogen oxides, carbon dioxides, hydrocarbon and water. The catalyst is exposed to unstable condition for temperature, gas flow rate and gas composition. The catalyst is consisting of several precious metals and support material. These materials are designed in nanometer size and contain often additives saying another word promoter. Hierarchical structures are built up from the powders designed in nanometer size to honeycomb structure in millimeter size through coated layers in micrometer size.
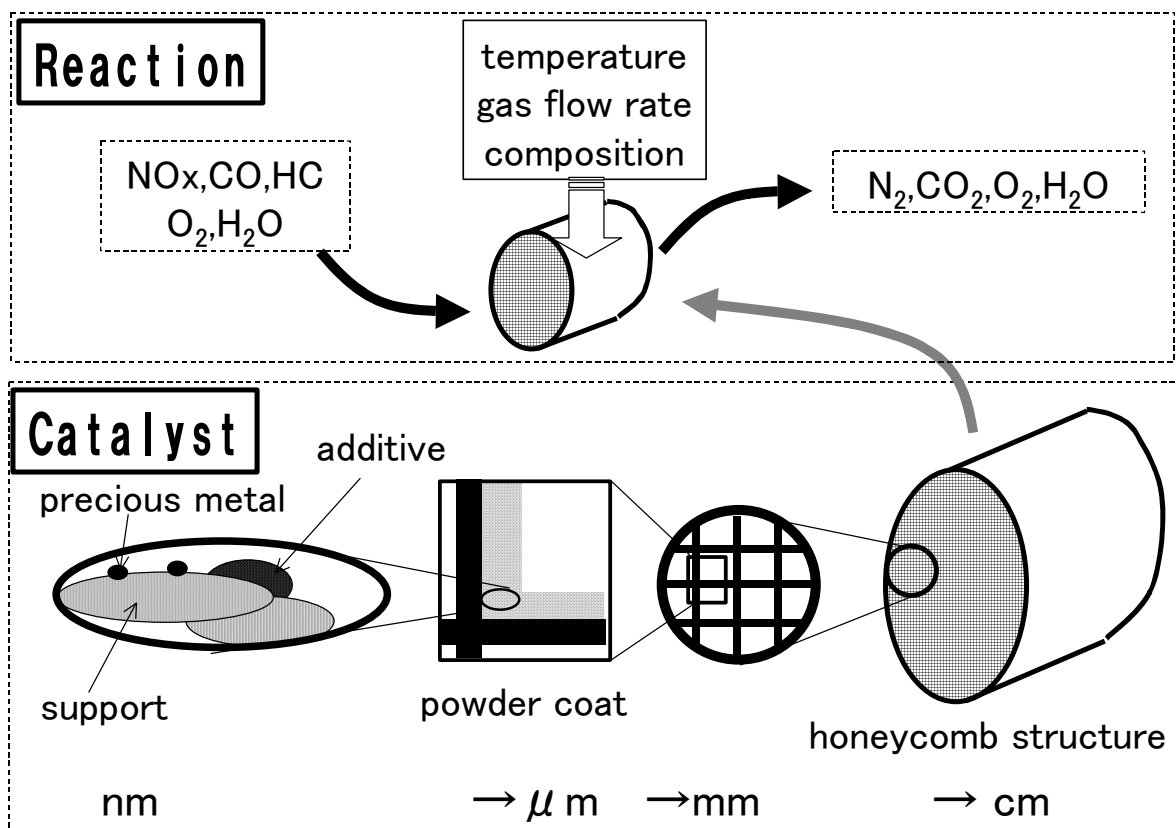
Figure 1　Reactions and hierarchic structure of automotive catalysts.

 Three way catalysts (TWC) are the typical successful examples of automotive catalysts, which are widely used all over the world. TWC can remove three main harmful components of hydrocarbons (HC), carbon monoxide (CO) and nitrogen oxides (NOx) simultaneously through oxidation and reduction reaction as the following (1)-(5) reactions.

 Oxidation

 $CO + 1/2O_2 \rightarrow CO_2$ (1)

$$C_xH_y + (x + y/4)O_2 \rightarrow xCO_2 + y/2H_2O \qquad\qquad (2)$$
Reduction
$$NO + H_2 \rightarrow 1/2N_2 + H_2O \qquad\qquad (3)$$
$$NO + CO \rightarrow 1/2N_2 + CO_2 \qquad\qquad (4)$$
$$(2x + y/2)NO + C_xH_y \rightarrow (x+y/4)N_2 + xCO_2 + 2/yH_2O \qquad\qquad (5)$$
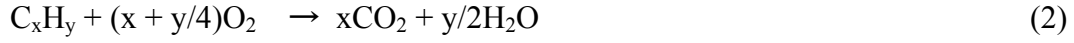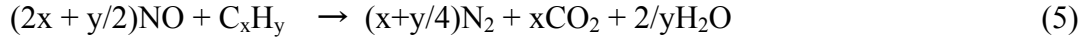
Figure 2 shows the influence of the air-to-fuel (A/F) ratio on the conversion for HC, CO and NO[1]. TWC has a unique ability to clean up exhaust gas involving the pollutants at the stoichiometric conditions (A/F=14.6). TWC purifies almost harmful gases through oxidations and reductions from (1) to (5) reaction. By operating the feedback control of A/F at 14.6 (Active system in Figure 2), conversions higher than 95% for HC, CO and NO can be obtained.
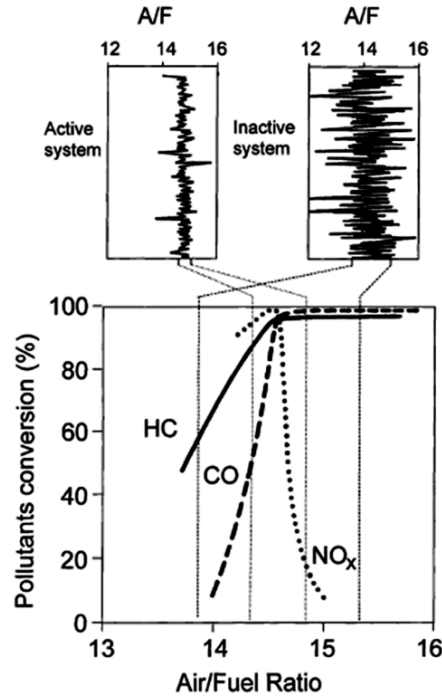
Figure 2　Influence of the A/F ratio on the catalytic efficiency of three-way catalysts[1].

It is worth to analyze not only the static but also the perturbation for a catalytic system as similar as electrical and mechanical other systems. A heterogeneous catalytic system like as automotive catalysts has several buffers; surfaces or crystallites of initial metal/additive particle, interface between metal particles and support/additive, secondary particles, slurry coated layer and catalytic converter itself. Theses buffers are sometimes compared with capacitors of an electric circuit. Here we call the transient response of the catalytic system for the dynamic change of atmosphere to "transient reaction". The time scale of the transient reaction will be mainly decided by the buffer size and gas flow rate. For example, the time scale concerning the initial particle around nanometer region will be

millisecond or less, and the time scale concerning the catalytic converter may be second or more.

We would like to explain briefly the importance of transient reaction analysis using as an example of oxygen storage material cerium oxide. It is usually difficult to control the engine condition accurately at the stoichiometric conditions however state of arts technologies combined gas sensing and controlling a fuel to supply an engine are used. The exhaust gas condition will be changed dynamically by such factors as the engine stroke of intake, compression, power and exhaust, variations of cylinder, start-up engine and acceleration and deceleration of car. The catalysts mounted just below engines will be exposed to fluctuations on the millisecond. The oxygen storage materials of cerium oxide can maintain the catalytic surface stoichiometric condition by reactions (6)-(9).

Oxidized condition
$$CeO_{2-x} + 0.5xO_2 \quad \rightarrow \quad CeO_2 \tag{6}$$
Reduced condition
$$CeO_2 + \quad xH_2 \quad \rightarrow \quad CeO_{2-x} + \quad xH_2O \tag{7}$$
$$CeO_2 + 0.25xCO \quad \rightarrow \quad CeO_{2-x} + 0.5xH_2O \tag{8}$$
$$CeO_2 + 0.5xC_yH_z \quad \rightarrow \quad CeO_{2-x(y+z/4)} + 0.5xyCO_2 + 0.25xzH_2O \tag{9}$$
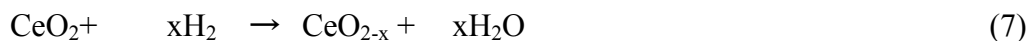
On the reduced condition, cerium oxides release the oxygen, which react with the reducing gas of H_2, CO and HC. Conversely, on the oxidized condition, cerium oxides store extra oxygen in order to promote the reaction of NO with HC and CO. The reaction of the oxygen release and storing should be evaluated for the purpose of developing effective oxygen storage materials.

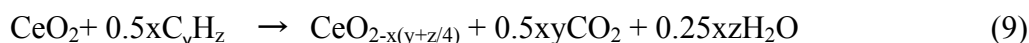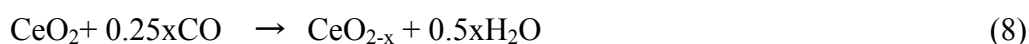In order to understand the complex automotive catalysts, it is effective to simplify reactions and materials. Modeling using single crystals simplify the complexities of real catalysts such as the precious metal dispersed catalysts. The single crystal surfaces are usually well defined by surface analysis. The ultra vacuum condition is adapted to many surface analysis techniques; Auger electron spectroscopy (AES), high-resolution electron energy loss spectroscopy (HREELS), low-energy electron diffraction (LEED), reflection absorption infrared spectroscopy (RAIRS), surface-enhanced Raman spectroscopy (SERS), UV photoelectron spectroscopy (UPS) and X-ray photoelectron spectroscopy (XPS). The surface science techniques combining single crystal samples and ultra vacuum systems have given us useful information about automotive catalysts.

CO oxidation of the reaction (1) is a very basic reaction for the catalytic research. Oh et al.[2] compared CO_2 formation rate per Rh atom on the single crystal surface of Rh(111), and Rh(100) with Rh dispersed catalysts (Figure 3). There is no obvious difference between single crystal and metal dispersed catalyst under the condition of CO and O_2 pressure of 10 mbar. The single crystal sample can simulate the real catalyst of metal dispersed catalyst very well on this case.

3
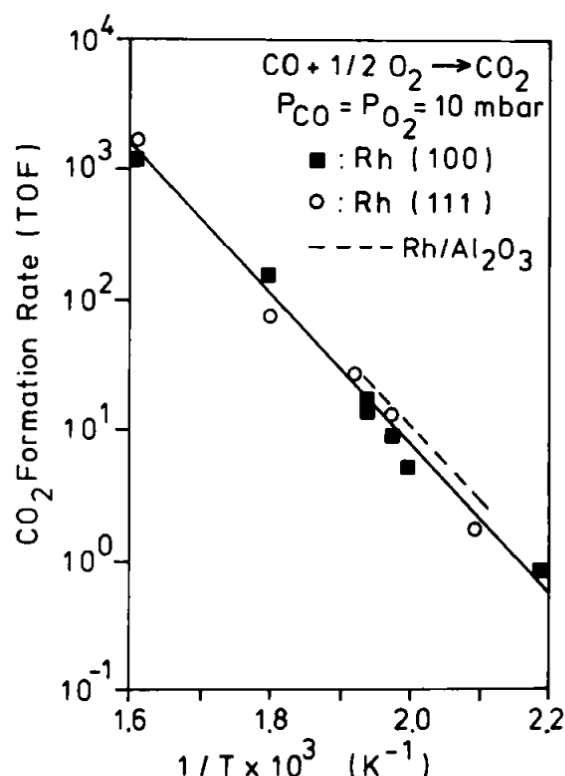
Figure 3 Arrhenius plots of CO oxidation reaction rates (turnover frequencies) on Rh showing a comparison between two [(111) and (100)] Rh single-crystal surfaces and supported Rh catalysts. P_{O_2}, = Pco = 10 mbar. The activation energy is ca. 126 kJ mol^{-1} in all cases [2].

Nevertheless successes of the surface science, it is well known that there are the gaps so-called "pressure and material gaps" between a fundamental surface science and a practical catalyst research[3,4]. The reason for this is because the gaps seem to arise from the way of taking a measurement. The former likes a combination of an ultrahigh vacuum system and a single crystal; the latter likes a combination of relatively high-pressure conditions and a powder catalyst with precious metal deposited.

It seems to be successful to use single crystals as models of real catalyst on the case of $CO+O_2$ reaction on Rh as shown in Figure 3. The same authors reported the different kinetic behavior for the NO+CO reaction on Rh(111), Rh(100) and Rh/Al$_2$O$_3$ of Rh dispersed catalyst [2]. It was found the obvious differences between single crystal and metal dispersed catalyst on NO+CO reaction. Figure 4 shows the NO+CO reaction on Rh is sensitive for the surface structure. The authors speculated that the rate-determining steps were the formation of N_2 for Rh (111) and NO dissociation for Rh/Al$_2$O$_3$. Similar tendency of the differences of the activation energy also reported on the case of NO+CO reaction on Pd[5]. There are good examples for material gaps between the single crystal and the real catalyst of metal dispersed catalyst.
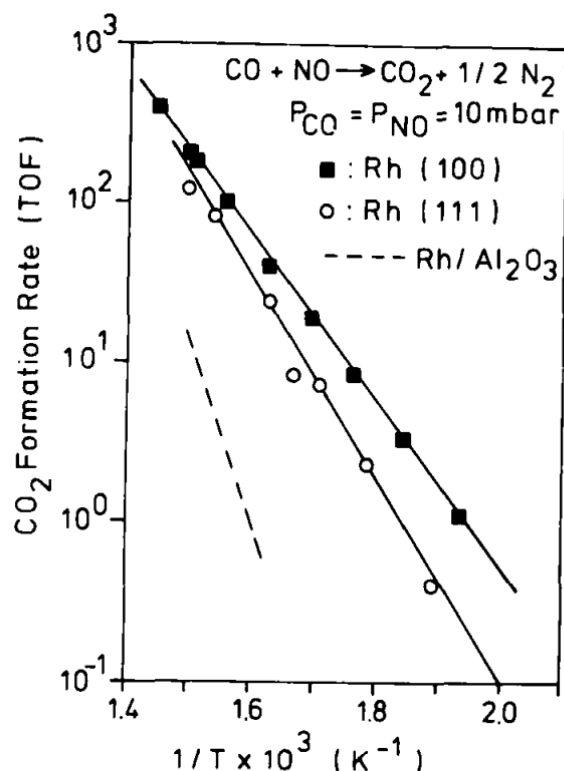
Figure 4 Comparison of the specific rates of the NO-CO reaction on Rh(111), Rh(100), and Rh/A1$_2$0$_3$ at P$_{CO}$ = P$_{NO}$ = 1 mbar [2].

Recently T. Shimada et al. also reported a pressure gap about the NO adsorption state on Pt(111)[6]. They measured NO adsorption on Pt(111) under various pressures of NO (up to 1 Torr) at room temperature using ambient pressure X-ray photoelectron spectroscopy (AP-XPS), near-edge X-ray absorption fine structure (NEXAFS) and scanning tunneling microscopy (STM) . Under 10^{-7} Torr, molecular NO occupies the most stable fcc-hollow sites and partially occupies the energetically unfavorable atop sites. NO reversibly desorbs from the atop sites after evacuation. On the other hands, at NO pressures higher than 10^{-6} Torr, irreversible adsorption of atomic oxygen takes place via NO dissociation, leading to the formation of NO + O domains.

Considering bridging these gaps and to simplify the actual phenomenon, we have been developing a new apparatus using an ultra high vacuum system for transient reaction analysis. Using pulsed valves technology, our apparatus can make various conditions of the automotive catalyst surface even in a vacuum chamber by supplying a large amount of gas to the surface. For the purpose of analysis for transient reactions with automotive catalysts, we plan to build a new method to measure them directly in millisecond time scale.

1-2.Purpose and Abstract

The main purpose of this study is to build a new apparatus and method, which enable transient reaction analysis both of real and model catalysts for automotive exhaust purification.

This thesis consists of ten chapters and the contents after second chapter are shown as follows.

In Chapter 2, the apparatus was described from the both views of hardware and software.

In Chapter 3, this new method was applied to evaluate the amount of oxygen storage in/release from catalysts on a millisecond scale per CO pulses.

In Chapter 4, the release and reduction of NOx in a NOx storage-reduction (NSR) catalyst were studied with a transient reaction analysis on the millisecond range.

In Chapter 5, the effect of precious metals and NOx storage materials were investigated using the analysis method in chapter 4.

In Chapter 6, a NOx storage and reduction catalyst for automotive exhaust gas was investigated using a model catalyst consisting of a Pt/Ba thin film on a silicon substrate.

In Chapter 7, in order to elucidate the mechanism for the preferential oxygen pumping on Pt–Au electrode for multi-electrode zirconia-based amperometric NO x sensors, the NO decomposition performance of different zirconia cells with various electrodes was investigated.

In Chapter 8, the contents from Chapter 2 to 7 were summarized.

[1] J.Kaspar, P.Fornasiero, N.Hickey, Catal. Today 77(2003) 419.
[2] S. H. Oh, G. B.Fisher, J. E. Carpenter, D. W. Goodman, J. Catal. 100(1986) 360.
[3] D.W. Goodman, Surface Science 299/300 (1994) 837.
[4] D.W. Goodman , Journal of Catalysis 216 (2003) 213.
[5] D. R. Rainer, S. M. Vesecky, M.Koranne, W. S. Oh, D.W. Goodman, J . Catal. 167 (1997) 234.
[6] T. Shimada,   B. S. Mun, I. F. Nakai, A. Banno, H. Abe,Y. Iwasawa, T. Ohta, H. Kondoh J. Phys. Chem. C, 114(2010)17030.

Chapter 2

Design and construction of a new apparatus

2-1. Introduction

Although the transient response of monolithic automobile catalysts in flow reactor measurements is usually no shorter than several seconds, this is caused by a large amount of microscopic 'migration' and 'storage' combined in series and /or in parallel. An elemental catalytic surface will present much faster transient responses.

The TAP (temporal analysis of products) system has successfully measured transient responses of catalyst in millisecond range[1,2]. The TAP system employs a dynamic vacuum system that attained this millisecond respnce with sufficient signal intensity by supplying high does of reactant gas pulse by pulsed valves and by high-speed evacuation with a 10" oil diffusion pump of 5300 l/s. This high dose-dynamic evacuation philosophy enables robust measurement of practical catalysts grains in a small reactor. To get a good signal to noise ratio in such dynamic vacuum system, a differential pumping system is employed for the decor ambient, Unfortunately. TAP system is not designed for planar samples. On the contra, the conventional molecular beam scattering experiments (MBS) are designed for planar samples and measurement of transient reaction has been done in sub-millisecond to millisecond range [3,4]. A well-qualified small amount of chopped molecular beam is prepared by differential pumping and supplied onto the sample surface in a UHV chamber statically pumped down by sputter-ion pumps with cold shroud. In contrast to TAP, the detector is usually located close to the sample without special differential pumping beside the cold shroud. Thus MBS is designed with the low doze-static evacuation philosophy for a delicate experiment on clean single crystal surface. However, it is too delicate to measure artificially designed catalytic surface comprising varieties of components. MBS for transient measurement uses a quadrupole mass spectrometer as in TAP system. Therefore, transient behavior of more than one mass species cannot be measured simultaneously. This is a fatal disadvantaged for analysis of actual reaction on automotive catalysts where plural species and plural reaction passes are concerned.

A new toll should have robustness and tolerance for wide variety of samples including planar versions of actual automotive catalyst. Therefore the high dose dynamic evacuation philosophy of TAP is more favorable than the low dose static evaluation philosophy of MBS. However, oil diffusion pump could be contamination source for a planar sample in contrast to the closed reactor system of TAP. Employment of planar sample also leads to loss of signal intensity.

Automotive catalyses sometimes show dependence of the history of former gas exposures whose origin is a subject of nonlinear dynamics [5]. Thus, artificial sequential exposure to plural gas species will be promising means for transient reaction analysis. Since

it is rather difficult to introduce plural molecular beam sources into the limited space, pulsed valves seems to be more favorable for gas sources.

2-2. Instrument design

Some required specifications for our transient reaction analysis of automotive catalysts is shown below.

(1) High pressure on the catalyst surface
(2) High sensitivity
(3) Time resolutions of measurements on the millisecond scale
(4) Ability to measure various gas components at once
(5) Ability to measure actual automotive catalysts

According to the above requisites, a system with pulsed valves to supply reactant species onto the planar sample surface, a contamination-free large cryopump for dynamic evacuation, and a time of flight mass spectrometer is designed. Signal intensity estimation was performed on a geometry where a pulsed valve is located at a distance of 50 mm from a 10 × 10 mm planar sample at the polar angle of 60 degree from the substrate normal and the TOF ionization region 5 × 5 × 5 mm is located at a distance of 125mm from the sample along the surface normal. If typical gas of 1×10^5 Pa and 300 K is injected through 0.5 mm aperture for 0.2 ms, no less than 1×10^{16} molecules per pulse come out, supplying 1×10^{14} molecules per cm2 onto the sample after 0.0663 ms with pulse broadening 0.005 ms. The reaction products that departed from the sample surface simultaneously shows an arrival time distribution at the ionization region with the full width of half maximum of 0.2 ms because of thermal velocity distribution. This means this system gives time resolution than 0.2 ms. Then we assumed 1×10^{14} molecules of reaction product per cm2 per pulse is emitted with a cosine distribution with respect to the surface normal, with a thermal velocity distribution at 600 K and in a constant rate during the 10 ms after the pulse. The 10 ms train of molecules which go through the ionization region is 4.76 m long with a square cross section 5 × 5 mm and contains 5.1×10^{10} molecules. Then a pulse of 1.56×10^{10} electrons of 100 eV generated by an electron gun can ionize 236.5 molecules of reaction products while the background signal corresponds 25.1 molecules when the background pressure is 1.33×10^{-7} Pa. Taking the detection efficiency of TOF mass system around 50% into consideration, the 118 counts per mass spectrum is very critical whether we could get meaningful data. At least it is necessary to accumulate data by repeating measurements.

Based on this estimation, the vacuum system and the data acquisition processing were developed. The system comprise (a)a dynamic vacuum system in which 2-4 pulsed valve can supply sub-ms gas pulses of plural kinds directly to catalytic surfaces held in UHV system at given intervals (typically 10 ms) and which can be pumped down again to 5×10^{-7} Pa level within 5s, (b) a TOF with 5 KHz periodic electron gun to ionize transient

Figure 1. Our newly developing apparatus (" Time-resolved Time-of-flight Mass-spectrometer with Molecular-Pulse-Probe Reaction Analysis at Surface of Catalyst" (TMPRAS; TM+). TM+ has four pulse valves, an ultra high vacuum system and Time of flight mass spectroscopy (TOF).

products ejected from catalytic surfaces just after the gas pulse injections. The detailed features of the vacuum system and the data acquisition system reported.

Figure 1 shows the apparatus schematic. It consists of three differential pumped chambers that are designed to minimize the effect of the dynamic gas flow created the abrupt gas injections from the pulsed valves. The first chamber (10^{-8}Pa) is a high conductance expansion chamber. A 14" cryopump is located under the 4 pulsed valves so as to pump out the injected molecules at products emitted isotopically from the surface of the planar catalyst in the first chamber are sampled by a skimmer located at the normal direction of the catalysts plane. Being collimated by the pass through the second chamber (10^{-7} Pa), the extracted reaction product beam finally enters the electron impact ionizer of the TOF system in the ionization chamber (10^{-8}Pa). In the ionization chamber, a tandem turbo molecular pump is used mainly to reduce the background gas pressure which contributes to the noise level. Behind the ionizer on the axis of the reaction product beam, a titanium sublimation pump with a liquid nitrogen cold baffle/panel is used to eliminate the contribution of the reaction products reflected at the chamber wall in the signal. To reduce the chances of air exposure of the ionization chamber, a specially designed small gate valve was developed and located at the entrance of the ionization chamber. The total distance between the sample surface and the

ionizer was reduced as much as possible to 125mm. This limits the minimum time resolution to be no less than 0.2 ms because of thermal velocity distribution.

A COMSTOCK TOF mass spectrometer with a 1 m flight tube was tuned to detect a 1-150 mass in 20×10^{-6}s. Since the signal sensitivity is more important than the mass resolution for our applications, a liner TOF system was employed instead of the recently prevailing angular-reflection system. The principal weak point inherent to the liner TOF system to give a ghost signal intensity in the foot of the intense mass peaks was successfully overcome by the data processing described below.

The flow of the data acquisition process is as follows. A personal computer (PC) creates master trigger signals (TTL) for a digital storage oscilloscope (DSO), the ionization gun (IG) for electron impact ionization and 4 pulsed valves (Figure 2). The experimental conditions can be set on the PC. The signal from the micro channel plate (MCP) is transferred to the 1Mbyte memory in DSO after A-D conversion. Here, the mass spectra triggered by the different timings of pulsed electron impact ionizations are stored in the different segments in the DSO memory. The data in the DSO memory were then transferred and added to the previously stored data in each segment of the PC.

In the typical example of measurement of NO reduction with H_2 on Pt films, data fro 100 cycles were accumulated to improve the signal to noise ratio. Here, one cycle stands for the series of data acquisition procedure which tool no more than 5 s. At the start of each cycle, we generated two pulses. One is a trigger for the H_2 gas and the other is a trigger for NO gas at 10 ms after the first trigger. A train of the IG trigger pulses at 5 kHz is also generated at the beginning of each cycle. These two pulsed valve were actuated for about 0.2ns to initiate reactions on the surface of the Pt film, and after that, 200 TOF spectra were sequentially recorded in the memories of the DSO every 0.2ms. The 200 TOF spectra measured for 40 ms in one cycles gave 1.6 Mbyte data. Then they were transferred to PC memories. It took about 500 s to complete 100 cycles.

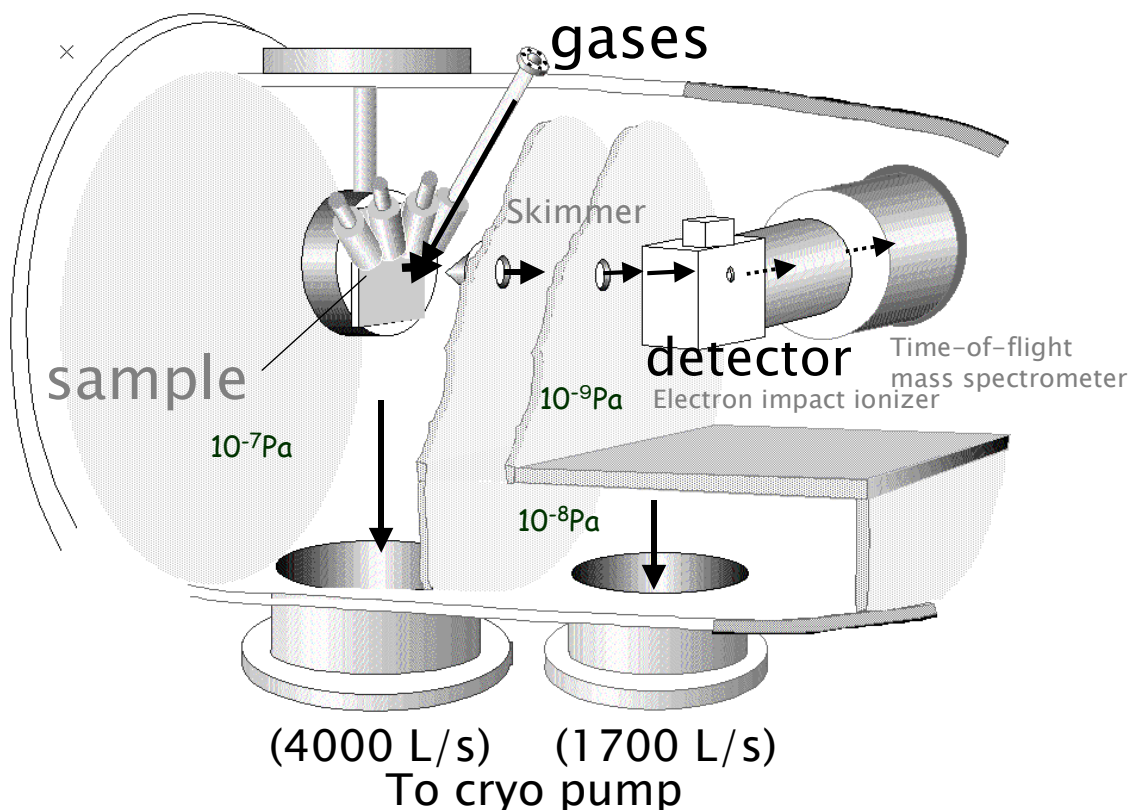Our apparatus needs four pulsed valves, an ultra high vacuum system and Time of flight mass spectroscopy (TOF) because of the above requirements (Fig. 2). We call our newly developed apparatus " Time-resolved Time-of-flight Mass-spectrometer with Molecular-Pulse-Probe Reaction Analysis at the Surface of a Catalyst (TMPRAS; TM+)
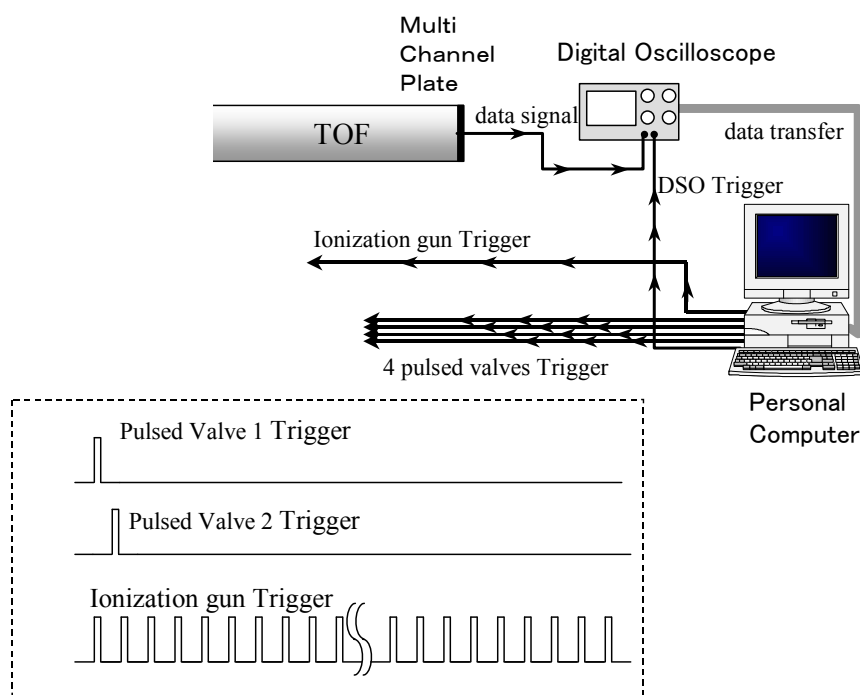
Figure 2 schematic diagram of electric wiring.

2-3..Performance of the system

Figure 3 shows the average of 20 measurements of the time profile of the pulsed gas (charged 3 kg/cm^2 with NO, operated the open time of the pulse valve for 0.5, 1.0 and 2.0 ms) reflected from the inert model sample of a fused silica plate with 50mm squarer and 1mm thickness after the gas injection. The open time shorter than 0.5 ms was found to make sufficiently narrow initial gas probes. After the gas injection, the pressure of each chamber rose quickly, but within 5 s it returned to the base pressure.
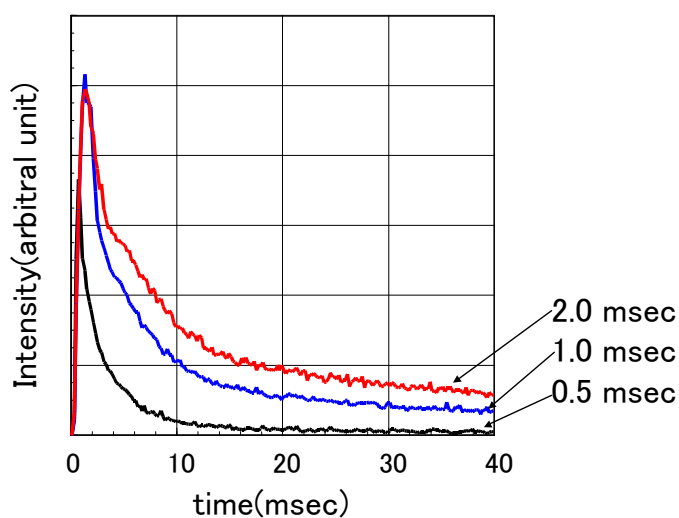
Figure 3 Time profiles of the pulsed gas reflected from quartz plate. The numeric character of 0.2,0.5,and 1.0 msec represent the operated pulse width.

11

CO oxidation on Pt is one of the most popular reaction for catalyst reaction. We tried to measure the CO oxidation on the Pt/γ Al$_2$O$_3$ catalyst as a test. The Pt/γ Al$_2$O$_3$ catalyst was made of Pt loaded γ Al$_2$O$_3$ powder; the substrate was 50mm square size alumina plate. After this sample was set in the TM+, pulsed CO and O$_2$ were injected on to the catalyst. Figure 4 shows the two-dimensional variations in the TOF mass spectra about CO oxidation reaction when pulsed CO and O$_2$ were injected at the same time. At the room temperature, the CO$_2$ peak (m/e=44) was not detected [Fig. 4(a)], however, after heating the catalysts to 673K, the CO$_2$ peak was detected [Fig. 4b)]. From this analysis of the CO oxidization reaction on Pt/γ Al$_2$O$_3$, it is found that the TM+ is a powerful tool to analyze the transient reaction on practical catalyst, which has a large amount of surface area.

Figure 5 shows the three-dimensional representation of NO+H$_2$ reaction on Pt film in the TOF mass spectra as a function of the ionization timing. When the mass peaks such as N$_2$ and H$_2$ were plotted vs. time, the time profile of the reaction products may be obtained easily. Since a large amount of gas was injected at one time by pulsed valves, neutral particles created in the acceleration region of the flight tube hit the MCP causing noises.
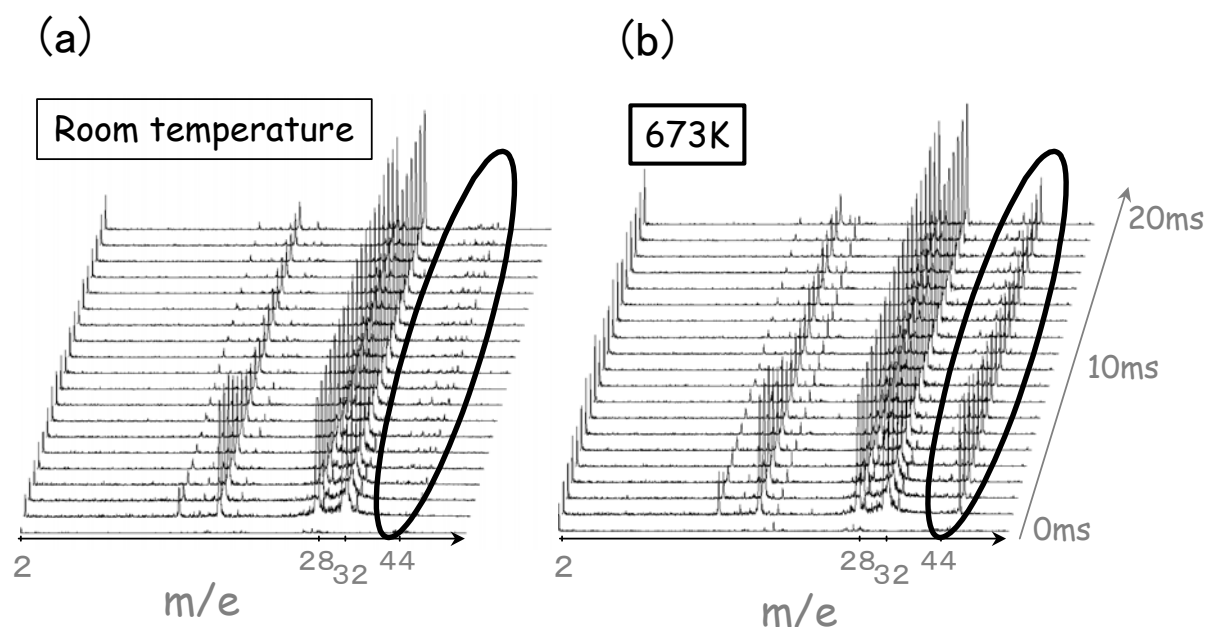
Figure 4. Three-dimensional representation of variation in TOF spectra about CO oxidation reaction on Pt/γ Al$_2$O$_3$.
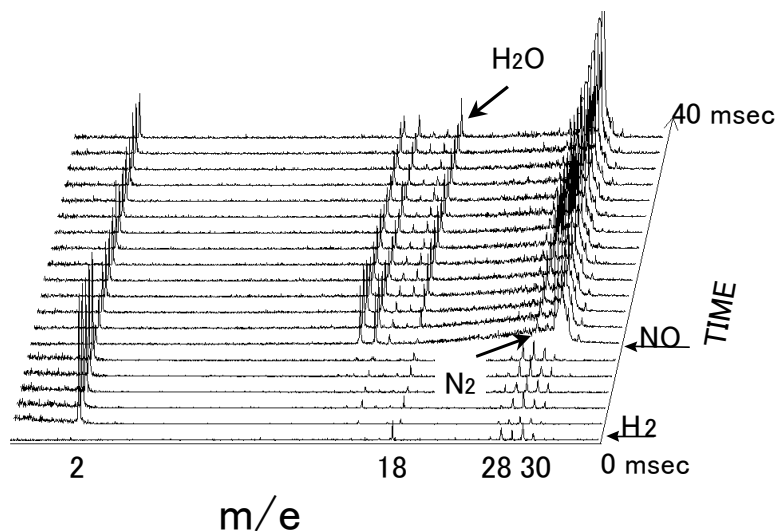
Figure 5 Three-dimensional representation of variation in TOF spectra

A typical TOF mass spectrum is shown in the insert in Figure6(a). Three peaks were identified as the mass number 27, 28 and 29 according to their time of flight. The mass signal of 28 consisted of the time of flight from 6.66×10^{-6} to 6.72E-6 s (region A in the insert). In figure 6(a), there should be no signal in the time of flight from 6.60×10^{-6} to 6.66 $\times 10^{-6}$ s (region B in the insert). However, if we took the time profile of that range, a very similar profile to that of the mass number 28 was obtained and is shown in Figure 6(a). A similar profile as in the region B was obtained in the region C.
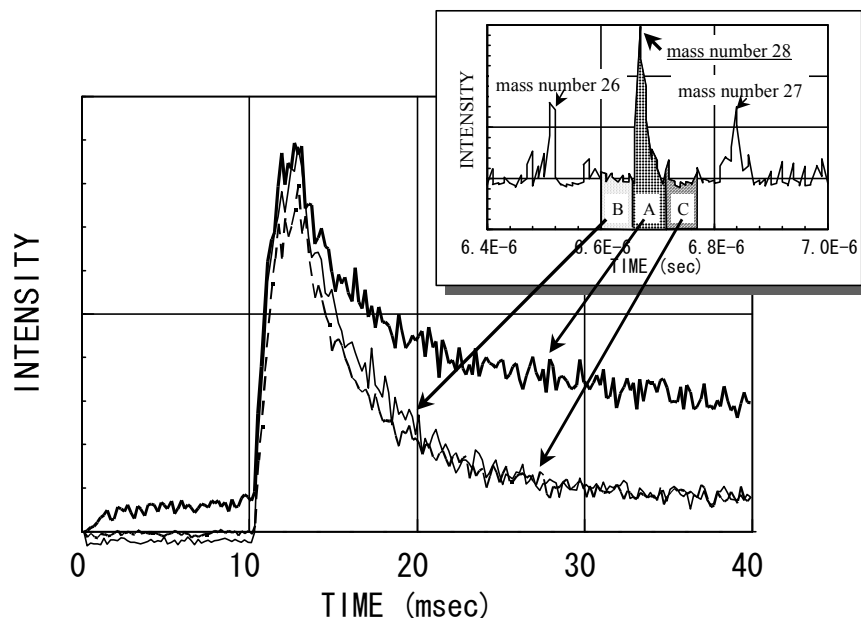
Figure 6 Time profiles of the area integrated in three regions A,B and C.

Thus, the noise mentioned above was contained in all of the TOF mass signals. After the subtraction of the average level of the B and C regions from the signal intensity in region A, we could get the true signal time profiles as shown in Figure 7. The solid line shows the time profile of N_2, the broken line shows the one of H_2O.
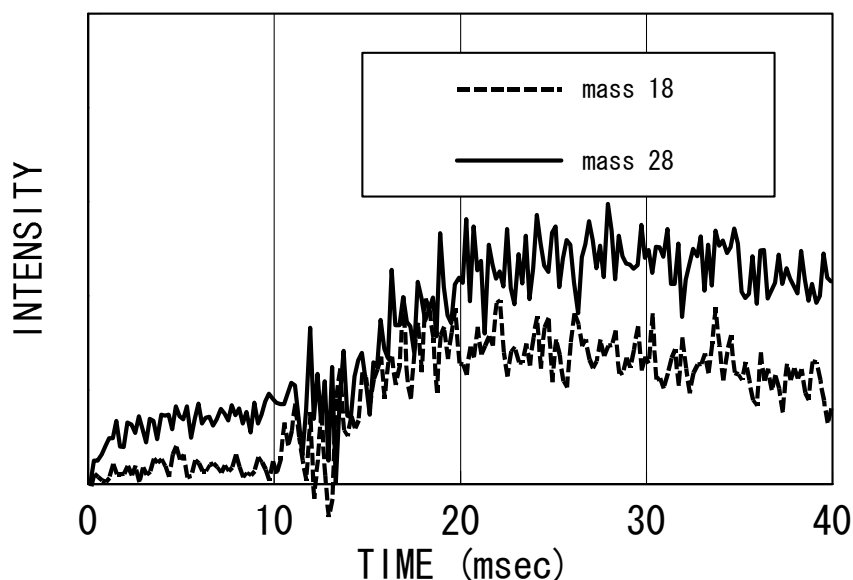
Figure 7 Time profile of mass 18 and 28 peaks.

Figure 8 presents a result of a H_2 pulse injection followed by a NO pulse injection after 10 ms to a 50×50 mm planar Al_2O_3 catalyst impregnated with Pt and Ba. It is shown that N_2 generation and sluggish H_2O generation synchronize with the NO injection. With constant O_2 leak, the profiles change into Figure 8(b). The H_2O generation synchronized with H_2 injection can be attributed to the reaction with adsorbed O_2. Figure 8(c) presents a result of a NO pulse injection followed by a H_2 pulse injection. It is shown that NO reduction to N_2 in the first 10 ms goes separately with H_2O production. Indicating direct reduction on Pt. With constant O_2 leak, the profiles change into Figure 8(d). The N_2 generation in the first 10 ms is gone. The evidence of NO_2 migration and storage has been obtained in a different mode using three pulsed valves and will be reported elsewhere in the near future. Here, we should stress that the effects of pulse order NO and H_2, and the constant leak of oxygen, are clearly elucidated with sufficient signal to noise ratio by only 100 times data accumulation for 12 min.

The system is also equipped with two sputter deposition sources as sample preparation means in a separate vacuum chamber connected with the system by a gate valve. Figure 2 presents the catalytic activity of a sputter deposited Pt thin film transported through the gate valve without air exposure in CO oxidation and that with 5 min air exposure. Surface poisoning by air exposure is clearly observed.

14
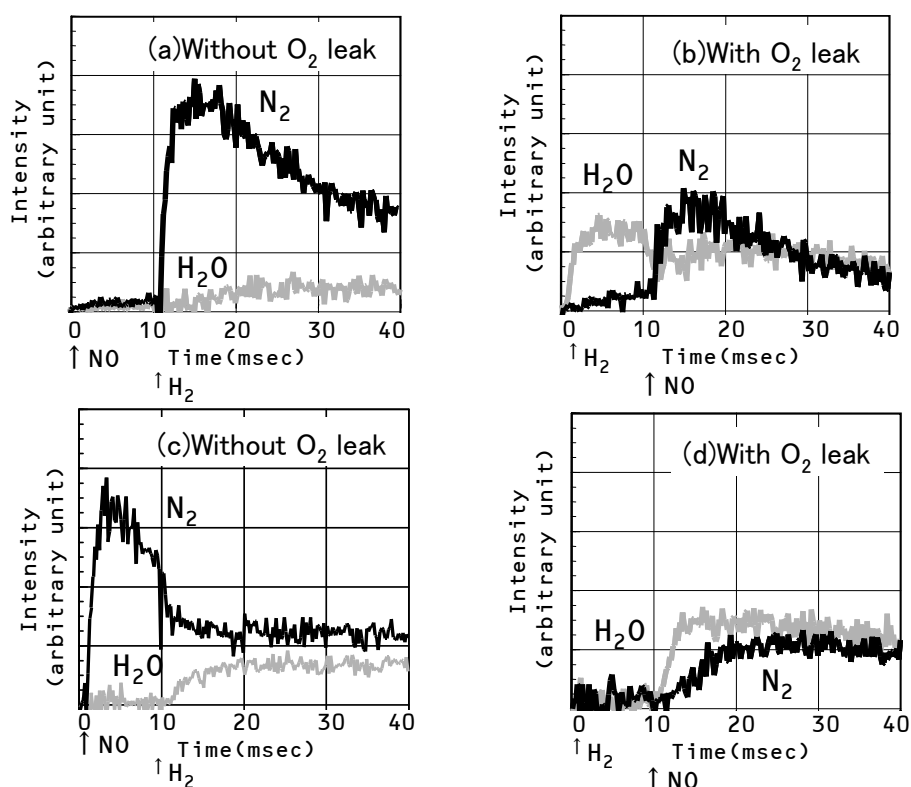
Figure 8 (a,c)Transient N_2 and H_2O production from 50×50 mm planar Al_2O_3 catalyst impregnated with Pt and Ba triggered by sequential injections of H_2 and NO pulse as indicated by thin an thick lined arrows respectively(b,d) at533K. These results under the constant O_2 leak.

2-4.Summary

A new research toll for the transient analyses of surface catalytic reactions on planar samples was developed. A simple liner TOF system was found to get sufficient signal intensity with help of (1) employment of pulsed valves to supply sufficient amounts of gas molecules to the planar sample, (2)the geometrical design of the vacuum system including a three stages differential pumping vacuum system, and (3)the background noise subtraction by data processing. The features in instrumentation, data acquisition and data processing are described with a typical example of NO+H_2 reaction on a Pt film at 673K, the change of the reaction products such as N_2 and H_2O were detected in ms range with sufficient signal intensity.

References

[1]J.T. Gleaves, J.R. Ebner, and T.C. Kuechler, , Catal. Rev. Sci., 30(1988) 49.

[2]J.T. Gleaves, G.S. Yablonskii, P. Phanawadee, and Y. Schuurman, Applied Catalyst A: General, 160 (1997) 55.

[3]K. Karahashi, J. Matsuo and S. Hijiya, Appl. Surf Sci., 60/61 (1992) 126.

[4]K. G. Nakamura and M. Kitajima, Appl. Phys. Left., 65(1994) 2445.

[5]J. E. Tuner, B. C. Sales, and M. B. Maple, Surf. Sci., 103(1981) 54.

Chapter 3

Evaluation of oxygen release from Pt/CeO$_2$ catalysts

3-1.Intoroduction

Ceria is one of the most important materials for the automotive three-way catalyst reaction (TWCR) because of its oxygen storage/release capacity (OSC). OSC is usually defined as the amount of oxygen stored in and released from the catalysts (1–5). It is reported that the OSC could be significantly improved by the doping of Zr and Y into ceria (6–10). It was reported that the evaluation of Pt/Ce$_6$Zr$_3$Y$_{0.5}$O$_{19.5}$ by the mode-simulating dynamometer indicated a high catalytic activity (1). The doping of Y into ceria–zirconia solid solution could improve the transient catalytic activity that was closely related to the OSC, but the doping did not improve the OSC in this case. The result of a conventional OSC measurement did not support the engine tests (11). In a conventional measurement by a thermal gravimeter (TG), OSC is investigated on a time scale of seconds and its absolute quantity is usually described in weight. However, the exhaust-gas compositions in an engine tail pipe simultaneously change according to the engine operating cycle on a millisecond time scale. Therefore, the gases that pass through a catalytic converter closely coupled to engines are not under steady-state conditions but drastically change on a millisecond scale.

Only a limited number of studies have been presented on the OSC on a millisecond scale (12–14). If a micro reactor system filled with pellet-type catalysts is used to measure the OSC as the standard catalytic reactivity measurement, the diffusion process, especially, the desorption process of the reaction products, spoils the time resolution of the products variation on the catalytic surface. Therefore, the results will not describe the exact features of the amount of oxygen storage in/release from catalysts on a millisecond scale (MS-OSC). On the other hand, the surface science approach, employing an ultrahigh vacuum and planar catalyst, is ideally suited for helping to understand surface phenomena because the complication due to diffusion process is negligible (15, 16). By employing this surface science approach in our newly developed apparatus (17), MS-OSC was measured with allows use to directly consider the MS-OSC as the amount of CO$_2$ without diffusion effects. The first objective of this study is to develop the MS-OSC measurement method of a catalyst on a planar substrate. The second objective is to investigate the relation between the MS-OSC and the other properties such as conventional OSC measurement, TWCR, Pt particle size, and support particle size.

3-2.Experimantal

3.2.1. Catalyst Preparation

The CeO$_2$–ZrO$_2$ support, with the composition CeO$_2$: ZrO$_2$ =1 : 1 in molar ratio, was prepared by the precipitation method in which aqueous ammonia was rapidly added to the

solution of $Ce(NO_3)_3$ and $ZrO(NO_3)_2$ until the pH reached 10. The resulting precipitation was filtered, dried at 110°C overnight, and then calcined in air for 1 h at 500°C. The calcined support is denoted as the C_5Z_5 support. The $CeO_2–ZrO_2–Y_2O_3$ support of the composition, $CeO_2 : ZrO_2 : Y_2O_3 = 46.5 : 46.5 : 7.0$ in molar ratio, was prepared by the same method. The obtained support is denoted as $C_{46.5}Z_{46.5}Y_{7.0}$. The $CeO_2–ZrO_2$ support of the composition, $CeO_2 : ZrO_2 = 5 : 1$ in molar ratio, was prepared by the precipitation–impregnation method in which aqueous ammonia was rapidly added to the solution of CeO_2 powder and $Zr(NO_3)_2$ until the pH reached 10. The obtained support is denoted as C_5Z_1.

The Pt/C_5Z_1, Pt/C_5Z_5, and $Pt/C_{46.5}Z_{46.5}Y_{7.0}$ catalysts were prepared as follows. In a typical preparation, the C_5Z_5 support was impregnated with an aqueous nitrate solution of $Pt(NH_2)_2(NO_2)_2$, followed by calcining at 250°C for 1 h in air, and then cooling to 25°C to prepare the Pt/C_5Z_5 powdered catalyst. The Pt/C_5Z_5 and $Pt/C_{46.5}Z_{46.5}Y_{7.0}$ powdered catalysts were prepared using the same method. The Pt loading amount was 0.1 wt% for the catalysts. A slurry was prepared by adding the powdered catalyst to deionized water and then reducing the amount of water by evaporation. The obtained slurry was wash-coated onto a planar cordierite substrate (50mm×50mm×1 t) and then dried at 110°C for 1 h to obtain the fresh planar catalysts for MS-OSC.

The powdered catalysts were pressed, crushed, and then sieved to form 0.3–0.7-mm pellets for the conventional measurement of the OSC and TWCR using the laboratory reactor. Some pellets and planar catalysts were heated at 1000°C for 2 h in the gas flow whose composition was changed from 1% O_2/N_2 to 1% H_2/N_2, and vice versa, every 5 min to obtain the thermally aged catalysts. To investigate the influence of the H_2 reduction on fresh and aged planar catalysts, the catalysts were heated in a gas flow composed of 5% H_2/N_2 at 500°C for 1 h to obtain the H_2-reduced planar catalysts.

To investigate the influence of the amount of Pt in the $Pt/C_{46.5}Z_{46.5}Y_{7.0}$ catalyst on MS-OSC, fresh and aged planar catalysts with compositions of 0.01, 0.1, and 1.0 wt% $Pt/C_{46.5}Z_{46.5}Y_{7.0}$ were prepared using the same method as mentioned earlier.

To investigate the influence of support deterioration, Pt thin-film catalysts of about 5-nm thickness were sputter deposited on planar cordierite substrates.

3.2.2. MS-OSC Measurement

Figure 1 shows a schematic of the apparatus to measure MS-OSC (16, 17). It consists of three pumped chambers. The interior of the chambers is kept at a high vacuum: the first chamber at about 10^{-6} Pa, the second chamber at $\sim 10^{-7}$ Pa, and the third chamber at $\sim 10^{-8}$ Pa. A planar catalyst holder and four gas-pulsed valves are arranged in the first chamber to inject the feed gas on the planar catalyst.
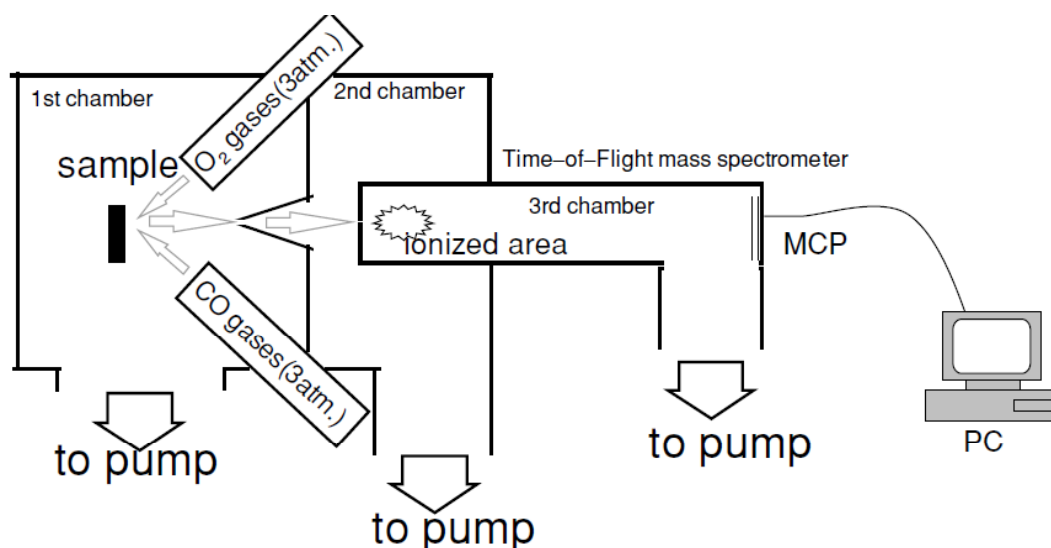
FIG. 1. Schematic of the apparatus used to measure MS-OSC.

The measurement procedure of the MS-OSC measurement is indicated as follows. Each catalyst was placed in the first chamber as shown in Fig. 1. The reaction products emitted from the catalyst were sampled through a skimmer located in a direction normal to the catalyst plane. The extracted reaction product beam, which was collimated by the pass through the second chamber ($\sim 10^{-7}$ Pa), finally entered into the electron impact ionizer of the time-of-flight (TOF) mass spectrometer in the third chamber (10^{-8} Pa). The ionized reaction products were detected by the TOF mass spectrometer on a millisecond scale.

Figure 2 shows the time profile of the average of 30 measurements for a pulsed gas (charged with 3 kg/cm^2 O$_2$, operated for 1.0, 1.5, 2.0, 2.5, and 3.0 ms of open time of the pulsed valve) reflected from the inert model catalyst of a fused silica plate (50 mm×50 mm× 1 t) after the gas injection. When the open times were shorter than 0.5 ms, they were found to make sufficiently narrow initial fast profiles.
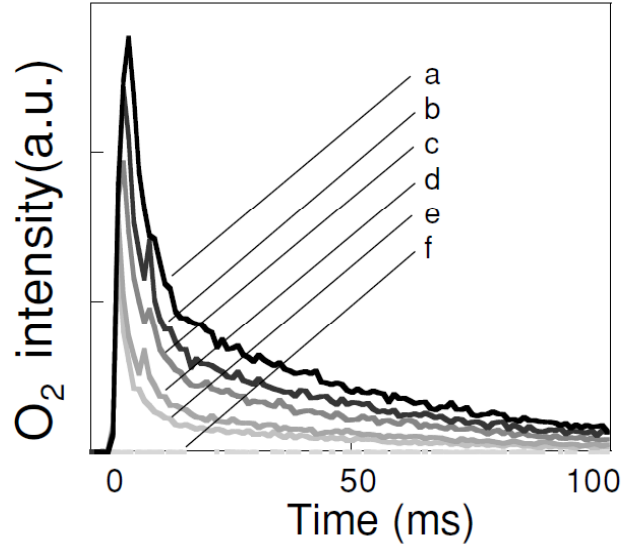
FIG. 2. O_2 emission profiles of a planar quartz sample after O_2 pulse injection. The open time of the O_2 pulse valve is indicated as follows: (a) 3.0 (b) 2.5 (c) 2.0 (d)1.5 (e) 1.0, and (f) 0.0 ms.

After the gas injection, the pressure of each chamber rose quickly, but within 5 s it returned to the base pressure. The pulse width of the pulsed gas became greater than that of the corresponding open time of the pulsed valve, because these shapes were measured as the reflections from the surface of the planar catalyst. Figure 3 shows the integrated amount of O_2 intensity in Fig. 2 as a function of the detecting time. As shown in Fig. 3, the pulse width of O_2 was in proportion to the integrated amount of O_2. The amount of each O_2 pulse injection was about 0.1 cc when the pulse width was set at 1 ms.
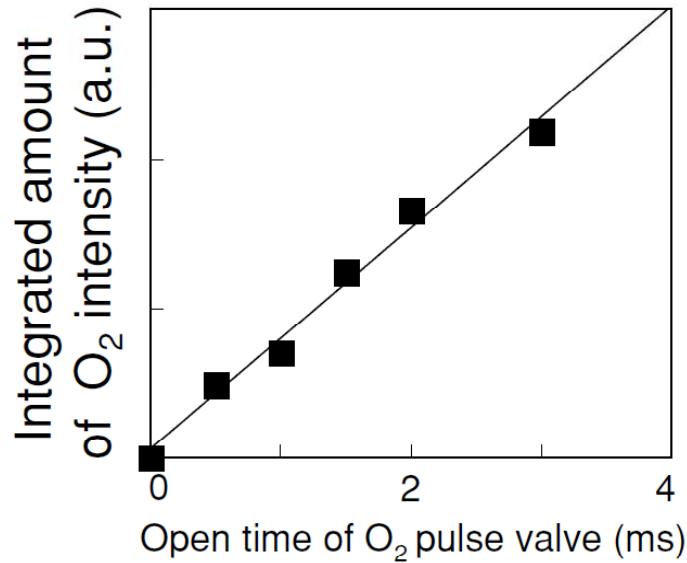
FIG. 3. Integrated amount of O_2 intensity in Fig. 2 as a function of open time of O_2 pulse valve.

Figure 4 shows the procedure for MS-OSC measurement. The surface temperature of all the planar catalysts was kept at 270℃ for all MS-OSC measurements. As a pretreatment CO was supplied to the surface of the planar catalysts until no more CO_2 was observed. After the pretreatment, the pulsed O_2 was supplied to the catalyst. The open time of the pulsed valve to inject O_2 was 0.3 to 4.0 ms. After 5 s, the pulsed CO, whose open time was set to 2.0 ms for the pulsed valve to inject CO, was supplied twice to the planar catalyst. CO reacted with the O_2 stored and adsorbed in the catalyst to form CO_2; the formed CO_2 was released from the catalyst. This procedure was repeated 30 times to improve the signal-to-noise ratio. The integrated amount of CO_2 per two CO pulses intensity released from the planar catalyst is defined as MS-OSC. Another experiment concerning MS-OSC was done using the same procedure except that H_2 was pulsed instead of CO and that the temperature of the catalyst was 500∘C.
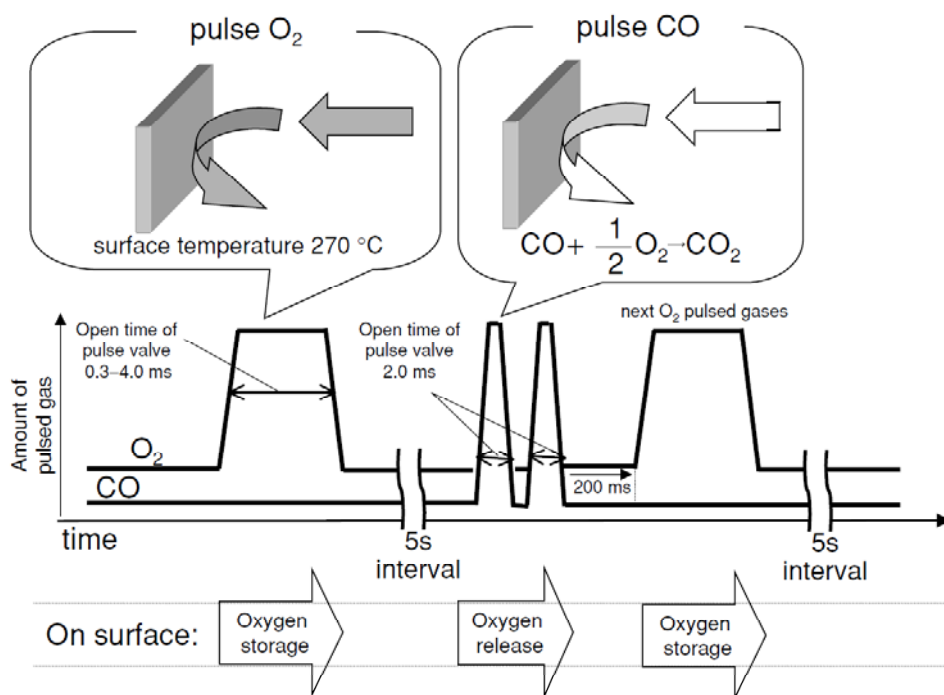
FIG. 4. Procedures for MS−OSC measurement.

3.2.3. Conventional OSC Measurement

Figure 5 shows the method for the conventional measurement of the OSC using a TG. The pellet catalyst was first exposed to a feed stream of 50%O_2/N_2 at 500∘C for 4 min. The catalyst was then exposed to 20% H_2/N_2 at 500∘C. In this process oxygen atoms that were stored in the reactor with H_2 form H_2O, which thus causes a weight loss of the catalyst. By measuring the weight loss, the evaluated amount of oxygen atoms from the catalyst was calculated to obtain the OSC.
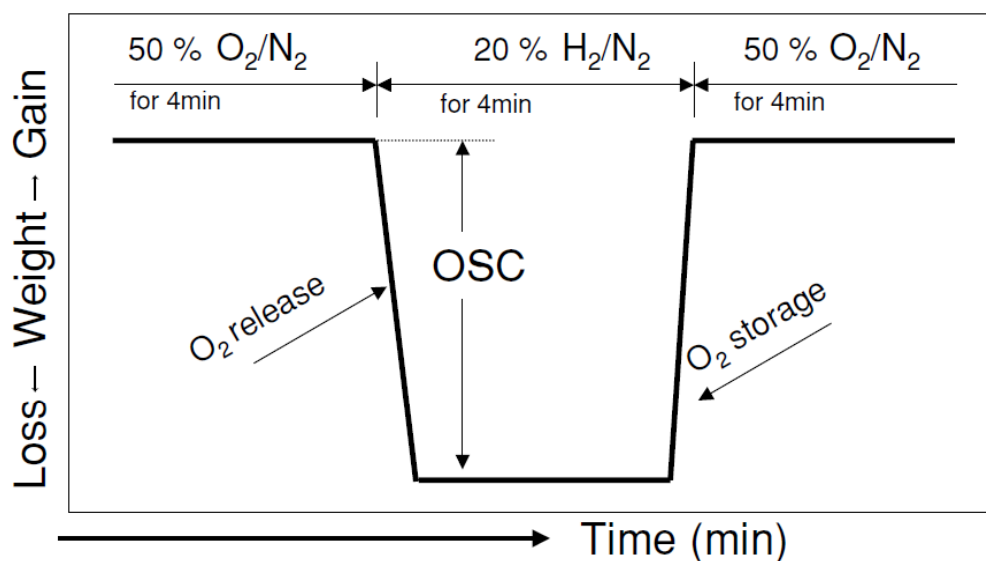
FIG. 5. Conventional OSC measurement by TG apparatus.

3.2.4. Three-Way Catalyst Reactivity Measurement

To investigate the TWCR for each light-off test, thermally aged catalysts were evaluated using a previously developed laboratory reactor (18). The catalytic activity data were obtained using a conventional fixed-bed flow reactor at atmospheric pressure. A quartz tube with an inner diameter of 18 mm was chosen as the reactor tube. A 1-cm3-pellet catalyst was placed at the middle part of the reactor. The upper part of the catalyst bed was packed with 7 cm3 of inactive SiC beads (3-mm o.d. in size) for preheating the atmosphere. The gas leaving the reactor was introduced into a condenser to remove the water vapor. The remaining components were continuously analyzed by several means: nondispersive infrared spectrometry for CO and CO_2, flame ionization for hydrocarbons (HC), magnetic susceptibility for O_2, and chemiluminesence for NOx . They were all attached to a Horiba MEXA-8120 gas analyzer. The atmosphere compositions and reaction conditions used in this study were as follows. The simulated stoichiometric mixture (simulated exhaust gas) consisted of 10.0% CO_2, 0.70% CO, 0.23%H_2, 1600 ppm C3H6, 1200 ppmNO, 0.64%O_2, 3 vol%H_2O, and the balance ofN_2. This mixture simulates the stoichiometric ratio of air to fuel (A/F=14.6). The evaluation atmosphere was periodically changed every 2 s around the stoichiometric atmosphere with a 4% A/F (from A/F=14.0 to 15.2) amplitude, which is defined as the difference from the evaluation atmosphere to the stoichiometric atmosphere. This amplitude was produced by additional O_2 or [3CO+H_2] injection (19). Catalysts were exposed to the simulated exhaust gas at 3.3 l/min while the temperature was decreased from 500 to 100∘C at the rate of 5 ℃/min and the space velocity was about 200,000 h−1. The

conversion data were measured at temperatures from 500 to 100°C. The TWCR was expressed as the temperature at 50% conversion of NO, CO, and HC.

2.5. Measurement of Pt and Support Particle Sizes and Surface Area of the Catalyst

To determine the particle size of the Pt and support, the XRD measurement was carried out using a RIGAKU RU-3L X-ray diffractometer with Co $K\alpha$ radiation. The particle sizes were calculated using Sherrer's equation (20). The surface area of the catalysts was measured by the BET method with N_2 adsorption.

3-3.Result

3.3.1. MS-OSC

Figures 6a, 6b and 6c show the time profile of the transient CO_2 production from the aged 0.1 wt% Pt/C_5Z_1, Pt/C_5Z_5, and $Pt/ C_{46.5}Z_{46.5}Y_{7.0}0$ catalysts, respectively, by sequential injections of CO and O_2 pulses. The temperature of these catalysts was 270°C. The CO pulsed gas was supplied to the catalyst at 0 and 100 ms. O_2 stored in the catalyst was released as CO_2 when the CO gases were supplied to the catalysts. Comparing these three catalysts, it was found that the greatest amount of CO_2 was released from the $Pt/ C_{46.5}Z_{46.5}Y_{7.0}$ catalyst thus indicating the highest activity.

Figure 7 shows the MS-OSC (the integrated amount of CO_2 per two CO pulses in Fig. 6) for the three kinds of catalysts as a function of the open time of the O_2 pulse valve. The integrated amount of CO_2 roughly corresponds to that of O_2 as shown in Fig. 3. Therefore, the amount of generated CO_2 was found to be proportional to the amount of O_2 stored on the catalysts.
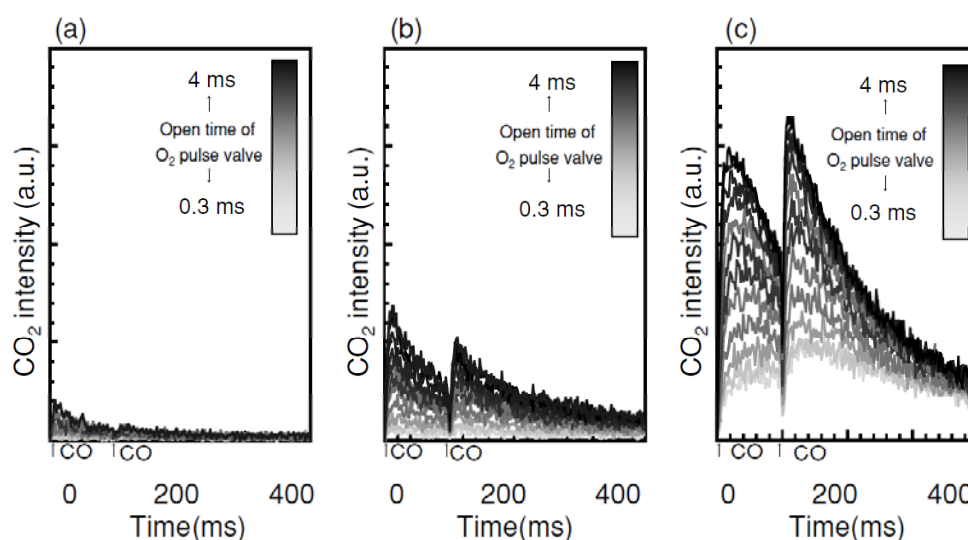
FIG. 6. Transient CO_2 production from aged 0.1 wt% Pt/C_5Z_1, Pt/C_5Z_5, and $Pt/C_{46.5}Z_{46.5}Y_{7.0}$ planar catalysts by sequential injection of two CO pulses as indicated by the two arrows: (a) 0.1 wt% Pt/C_5Z_1 (b) 0.1 wt% Pt/C_5Z_5, and (c) 0.1 wt% $Pt/C_{46.5}Z_{46.5}Y_{7.0}$ catalysts.
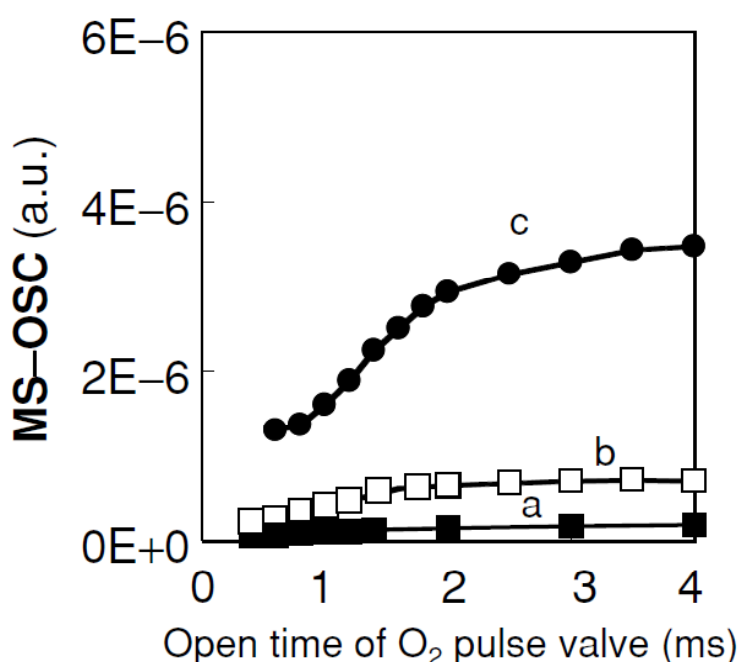
FIG. 7. MS–OSC (integrated amount of CO_2 per two CO pulses in Fig. 6) of aged 0.1 wt% $Pt/C_{46.5}Z_{46.5}Y_{7.0}$, Pt/C_5Z_5, and Pt/C_5Z_1planar catalystsas a function of open time of O_2 pulse value: (a) $Pt/C_{46.5}Z_{46.5}yY7.0$(b) Pt/C_5Z_5, and (c) Pt/C_5Z_1.

Figures 8a and 8b, respectively, show the MS-OSC of the fresh and aged 0.1 wt% $Pt/C_{46.5}Z_{46.5}Y_{7.0}$ and 0.1 wt% Pt/C_5Z_5 catalysts before and after heating in flowing 5% H_2/N_2 gas at 500°C for 1 h. H_2 reduction for the fresh catalyst was found to increase with the intensity of MS-OSC. On the other hand, H_2 reduction for the aged catalyst was less closely related to the increasing amount of MS-OSC.

Figure 9 shows the MS-OSC of fresh 0.01, 0.1, and 1.0 wt% Pt/ catalysts. The MS-OSC of the catalysts was increased with increasing amount of Pt. Figures 10a and 10b, respectively, show the MS-OSC of the catalysts consisting of the $C_{46.5}Z_{46.5}Y_{7}0$ and C_5Z_5 support and Pt thin film deposited on it up to 5mmin thickness, before and after the heat treatment at 500°C in the flowing gas of 5% H_2/N_2. Here, the interfacial area between Pt and the support remained unchanged for each catalyst, because the same amount of Pt was evaporated on each support by the sputter method (20).
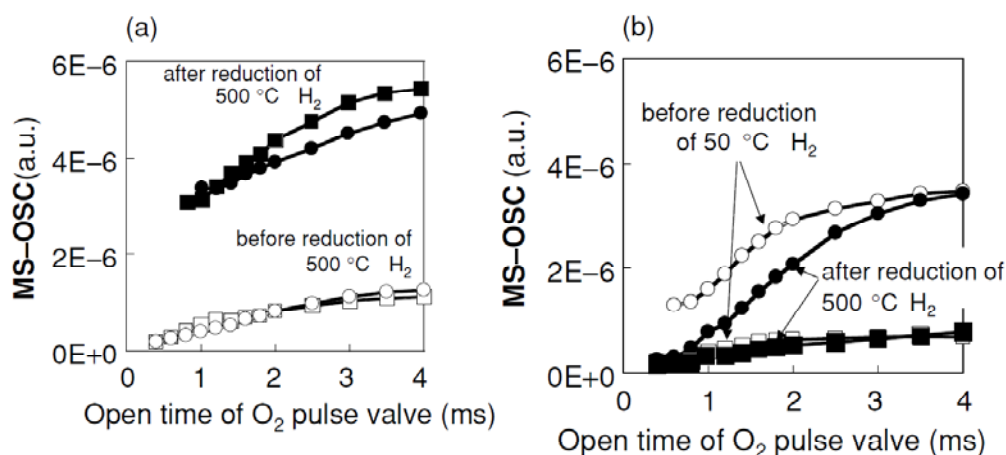
FIG. 8. MS−OSC of (a) fresh and (b) aged Pt/C46.5Z46.5Y7.0 and Pt/C$_5$Z$_5$ planar catalysts before and after H$_2$ reduction at 500℃ as a function of pulse width (open time of oxygen pulse valve). Aged catalysts are obtained by heating fresh catalysts at 1000℃: , 0.1 wt% Pt/C$_{46.5}$Z$_{46.5}$Y$_{7.0}$ planar catalysts before H$_2$ reduction at 500℃; , 0.1 wt% Pt/C$_5$Z$_5$ planar catalyst before H$_2$ reduction at 500°C; , 0.1 wt% Pt/C$_{46.5}$Z$_{46.5}$Y$_{7.0}$ planar catalysts after H2 reduction at 500°C; and , 0.1 wt% Pt/C$_5$Z$_5$ planar catalyst after H$_2$ reduction at 500°C.
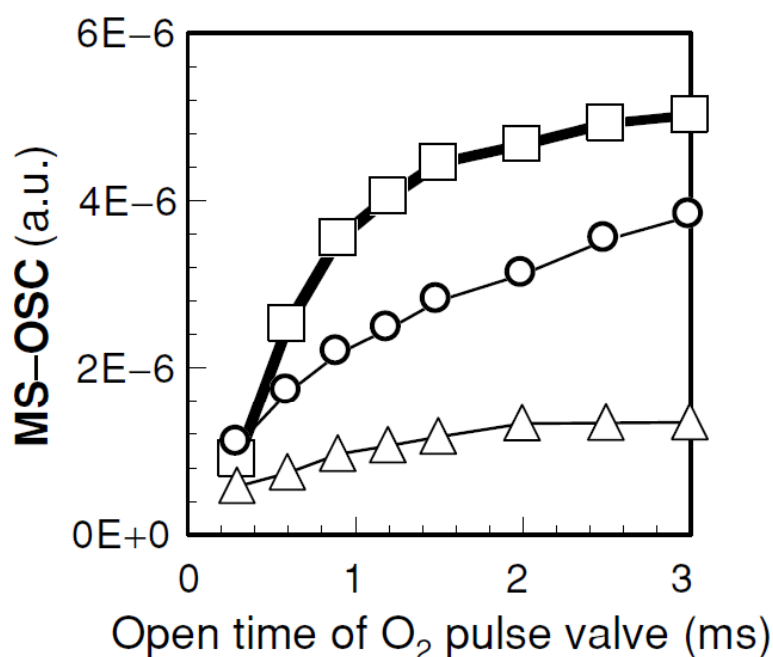
FIG. 9. Effect of Pt amount on MS−OSC of fresh Pt/C46.5Z46.5Y7.0 catalysts: , 0.01 wt% Pt; , 0.1 wt% Pt; and , 1.0 wt% Pt.

Initially, both catalysts showed almost the same MS-OSC as shown in Fig. 10a; however, after the heat treatment of the support itself, the MS-OSC of the catalyst on the C$_{46.5}$Z$_{46.5}$Y$_{7.0}$ support was greater than that on the C$_5$Z$_5$ support as shown in Fig. 10b.
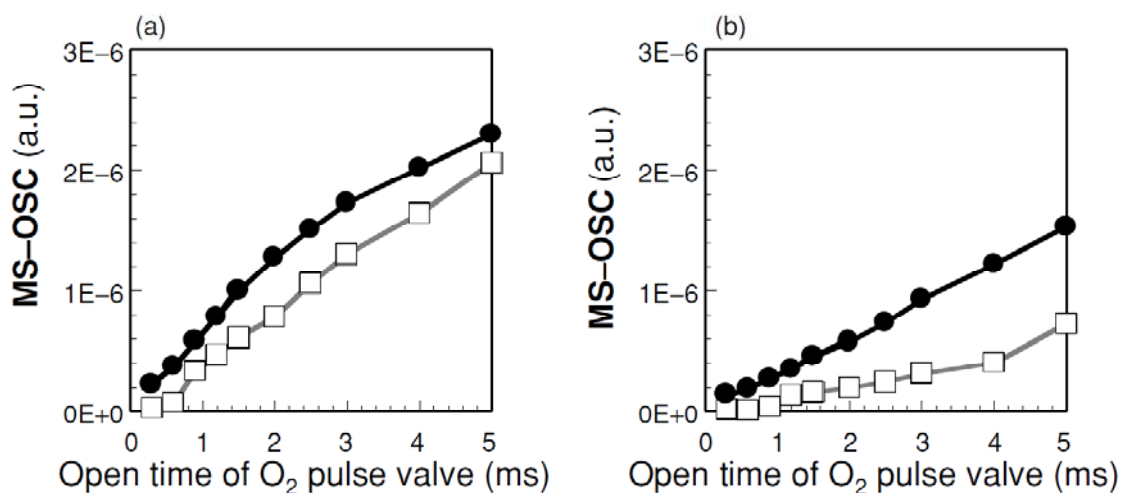
FIG. 10. MS–OSC of catalyst consisted of a sputter-deposited Pt thin film in 5-nm thickness on $C_{46.5}Z_{46.5}Y_{7.0}$ and C_5Z_5 supports (a) before and (b) after heated at 500°C in flowing 5% H_2/N_2: , 0.1 wt% Pt/$C_{46.5}Z_{46.5}Y_{7.0}$ planar catalysts; and , 0.1 wt% Pt/C_5Z_5 planar catalyst.

3.3.2. Conventional OSC

Figure 11 shows the conventional OSC of the aged 0.1 wt% Pt/C_5Z_1, 0.1 wt% Pt/C_5Z_5, and 0.1 wt% Pt/ $C_{46.5}Z_{46.5}Y_{7.0}$ pellet catalysts. The OSC of the Pt/C_5Z_5 pellet catalyst was the greatest among these three catalysts.
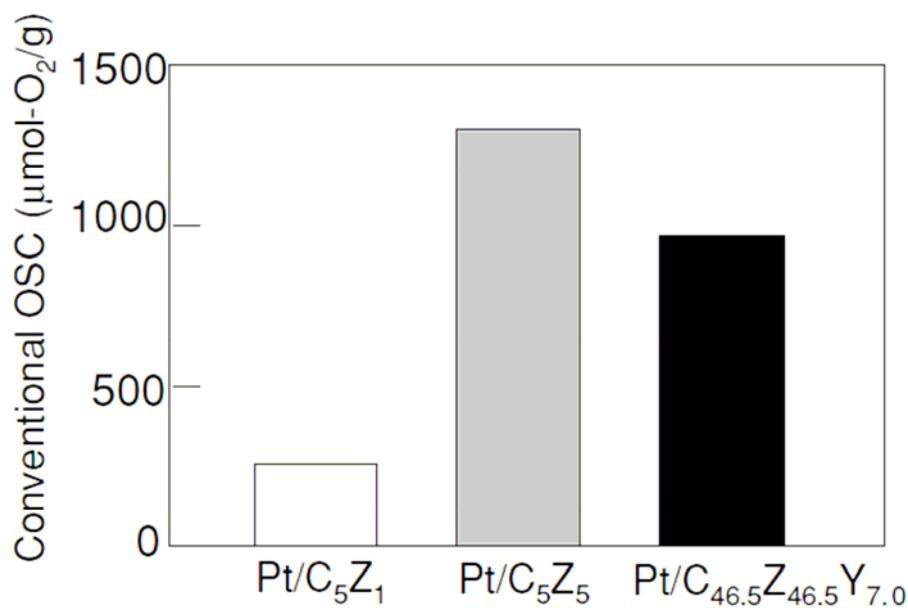
FIG. 11. Conventional OSC of aged pellet catalysts.

3.3. Catalytic Activity

Figure 12 shows the temperature at 50% conversion (T50) of NO, CO, and HC on the aged 0.1 wt% Pt/C_5Z_5 and 0.1 wt% $Pt/C_{46.5}Z_{46.5}Y_{7.0}$ pellet catalysts. The aged $Pt/C_{46.5}Z_{46.5}Y_{7.0}$ catalyst was found to have a lower T50 indicating a higher TWCR than that of the Pt/C_5Z_5 catalyst.
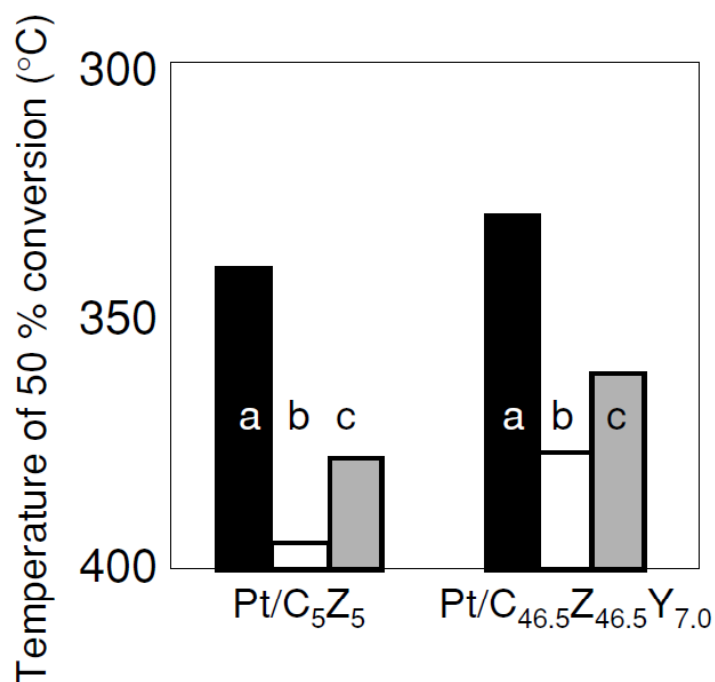
FIG. 12. Temperature at 50% conversion of NO, CO, and HC for aged pellet catalysts with 0.1 wt% Pt heated at 1000°C: (a) NO, (b) CO, and (c) HC.

3.3.4. The Particle Size of Pt and Support and Surface Area

Figures 13a and 13b, respectively, show the particle size of the supports and Pt particles of the aged 0.1 wt% Pt/ $C_{46.5}Z_{46.5}Y_{7.0}$ and 0.1wt%Pt/C_5Z_5 powdered catalysts. The support particle size of the aged 0.1 wt% Pt/ $C_{46.5}Z_{46.5}Y_{7.0}$ catalyst was greater than that of the aged Pt/C_5Z_5 catalyst as shown in Fig. 13a. However, the Pt particle size of the Pt/ $C_{46.5}Z_{46.5}Y_{7.0}$ catalyst was smaller than that of the Pt/C_5Z_5 catalyst as shown in Fig. 13b. The Pt crystallite of the aged Pt/ $C_{46.5}Z_{46.5}Y_{7.0}$ catalyst was so small that a Pt diffraction line could not be detected. Fig. 13c shows the surface area of the 0.1 wt% Pt/C46.5Z46.5Y7.0 and 0.1 wt% Pt/C_5Z_5 powdered catalysts. The surface area of Pt/C46.5Z46.5Y7.0 was higher than the one for Pt/C_5Z_5 in both the fresh and aged catalysts.
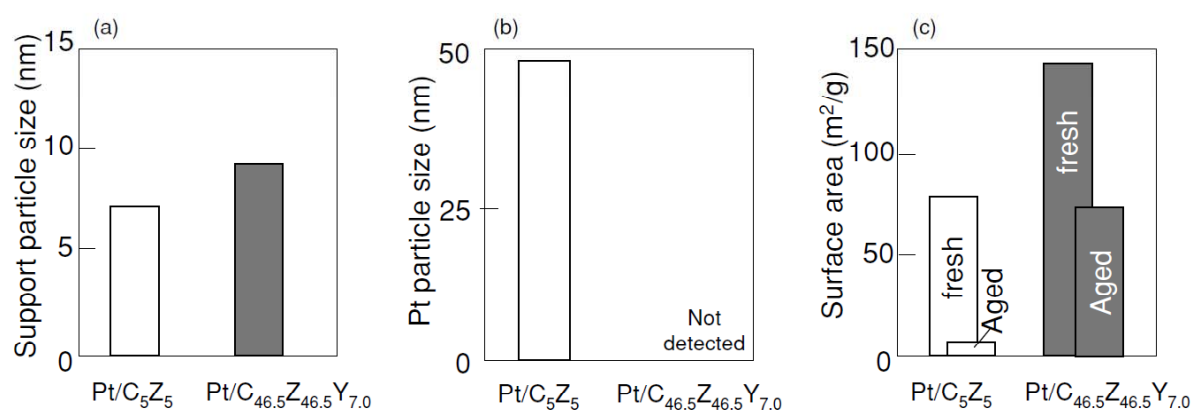
FIG.13. Mean particle size for aged powdered catalysts and surface area for fresh and aged powders: (a)support particle size (b)Pt particle size, and (c) surface area.

3-4. DISCUSSION

To determine the best conditions where the OSC of ceria is fully utilized in the automotive catalyst, it is important to understand the OSC phenomenon on a millisecond time scale. Oxygen storage was considered to occur very fast not only on the Pt-catalyzed ceria but also on pure ceria, whereas the oxygen release was considered to be slow (21). In particular, the response of oxygen release toward the pulsed CO must be connected to the limiting factor for the purification of exhaust gases from an automobile.

The intensity of the MS-OSC signal is the response of O_2 release at CO pulses. The result obtained in this study corresponded to the results of other measurements such as the TWCR (Fig. 12), Pt particle size (Fig. 13b) and also the result of engine tests (11). Therefore, MS-OSC is thought to be a suitable measure for comparing the OSC in real engine emissions.

The wash-coat thickness of all samples was measured to be almost 500 μm. It was roughly estimated that the ratio of the amount of oxygen storage and release to the total amount of OSC measured by a conventional method was about 1/100 - 1/1000. The oxygen storage and release reaction was considered to occur at the surface. Surface roughness may affect MS-OSC on the surface. Figure 13c indicated that the surface area of the fresh Pt/$C_{46.5}Z_{46.5}Y_{7.0}$ was almost two times greater than that of the fresh Pt/C_5Z_5. However, MS-OSC of these samples was almost the same(Fig. 8a); nevertheless, the Pt particle size on both supports was very small. It was considered that the surface roughness factor must be a minor condition in these cases.

Here, the cause of the $C_{46.5}Z_{46.5}Y_{7.0}$ catalyst being thermally more stable than the Pt/C_5Z_5 catalyst is discussed. The loss of OSC is caused by several factors: growth of the particle size of CeO_2 (22, 23), loss in surface area of CeO_2(24, 25), structure changes in the oxides (26, 27), and loss of contact force between the precious metal and CeO_2 (8, 28, 29). Also, the addition of ZrO_2 to CeO_2 and Y2O3 leads to an improvement in the OSC (8, 30–32). The thermal stability prevents the loss in surface area of the $C_{46.5}Z_{46.5}Y_{7.0}$ and Pt particles sintering on $C_{46.5}Z_{46.5}Y_{7.0}$. On the other hand, the intensity of the MS-OSC signal is found to depend significantly on the physical state of the Pt particles. The intensity of MS-OSC signal becomes higher as shown in Figs. 6 and 9 for the following cases: when the size of the Pt particles becomes small (Figs. 7 and 13b), and when the amount of pulsed oxygen is increased (Figs. 6 and 9). The loss of the MS-OSC signal intensity should be caused mainly by the poor interface between the Pt particle and ceria component.

Figure 10 shows another cause of the loss of MS-OSC intensity. The amount of Pt and particle size of the Pt/$C_{46.5}Z_{46.5}Y_{7.0}$ and Pt/C_5Z_5 catalysts are supposed to be almost the same (20). However, the intensity of CO_2 in the MS-OSC measurement for the Pt/$C_{46.5}Z_{46.5}Y_{7.0}$ catalyst was higher than that of the Pt/C_5Z_5 catalyst. This result is responsible for the exact cause as to the why $C_{46.5}Z_{46.5}Y_{7.0}$ support may be thermally more stable than the C_5Z_5 support.

3-5. CONCLUSIONS

The faster response of the OSC plays a more important role than the slower response of the conventional OSC on three-way catalysts to purify exhaust gases under transient atmosphere in a real engine. We have developed a new method to measure the fast response of the OSC, which we call the MS-OSC method. By measuring the MS-OSC, the following results were obtained:

1. The MS-OSC measurement is based on the principle of the fast detection of reaction products on catalyst surfaces following CO and O_2 injections using pulsed valves by TOF mass spectrometry.

2. MS-OSC is regarded as the response of CO_2 released from the catalyst by CO pulsed on a millisecond scale.

3. MS-OSC significantly depends on the Pt particle size of the Pt catalyst with the ceria component.

4. MS-OSC is in good agreement with the engine test results (11).

REFERENCES

[1] Taylor, K. C., *Catal. Rev. Sci. Eng.* **35**(1993) 457.

[2] Gandhi, H. S., Piken, A. G., Shelef,M., and Delosh, R. G., SAE Paper 760201 (1976).

[3] Schlatter, J., SAE Paper 780199 (1978).

[4] Yao, H. C., and Yao, Y. F. Y., *J. Catal.* **86**(1984) 254.

[5] Fisher, G. B., Thesis, J. R., Casarella, M. V., and Mahan, S. T., SAE Paper 931034 (1993).

[6] Miyoshi, N., Matsumoto, S., Ozawa, M., and Kimura, M., SAE Paper 891970 (1989).

[7] Ozawa, M., Kimura, M., and Isogai, A., *J. Alloys Compd.* **193**(1993) 73.

[8] Matsumoto, S., Miyoshi, N., Kanazawa, T., Kimura, M., and Ozawa, M., *in* "Catal. Sci. and Tech." (S. Yoshida, N. Tabezawa, and T. Ono, Eds.), Vol. 1, p. 335. Kodansha-VCH, 1991.

[9] Yamada, K., Tanaka, H., Aozasa, A., Matui, H., and Motoyama, M., *J. Alloys Comp.* **193**(1993) 298.

[10] Suda, A., Sobukawa, H., Suzuki, T., Kandori, T., Ukyo, Y., and Sugiura, M., *J. Ceram. Soc.* **109**(2001) 177.

[11] Tanaka, H., Tan, I., Yamada, K., and Yamamoto, M., ASATA 98ATE018 (1998).

12] Vidal, H., Bernal, S., Kaspar, J., Pijolat, M., Perrichon, V., Blanco, G., Pintado, J. M., Baker, R. T., Colon, G., and Fally, F., *Catal. Today* **54**(1999) 93.

[13] Nibbelke, R. H., Nievergerd, A. J. L., Hoebink, J. H. B. J., and Marin, G. B., *Appl. Catal.*, *B* **19**, 245 (1998).

[14] Holmgen, A., and Anderson, B., *J. Catal.* **178**(1998) 14.

[15] Altman, E. I., and Gorte, R. J., *Surf. Sci.* **195**(1988) 392.

[16] Motohiro, T., Kizaki, Y., Sakamoto, Y., Higuchi, K., Tanabe, T., Takahashi, N., Yokota,

Y., Doi, H., Sugiura, M., and Noda, S., *Appl. Surf. Sci.* **121/122**(1997) 323.

[17] Motohiro, T., Kizaki,Y., Sakamoto,Y., Higuchi, K.,Watanabe,Y., and Noda, S., *Appl. Surf. Sci.* **121/122**(1997) 319.

[18] Muraki, H., Yokota, K., and Fujitani, Y., *Appl. Catal.* **48** (1989) 93.

[19. Shinjoh, H., Takahashi, N., Yokota, K., and Sugiura, M., *Appl. Catal.,B* **15**, 189 (1989).

[20. Cullity, B. D., *in* "Elements of X-ray Diffraction" (M. Cohen, Ed.),2nd ed., p. 285. Addison–Wesley, Reading, MA, 1987.

[21. Holmgren, A., and Andersson, B., *J. Catal.* **178**(1998) 14.

[22. Cordatos, H., Bunluesin, T., Stubeenrauch, J., Vohs, J. M., and Gorte,R. J., *J. Phys. Chem.* **100**(1996) 785.

[23]Zhang, Y., Anderson, S., and Muhammaed, M., *Appl. Catal., B* **6**(1995) 325.

[24]Hakonen, M. A., Aita, E., Lahtl, A., Luoma, M., and Maunula, T., SAE paper 910846 (1991).

[25]Trovarelli, A., deLeitenburg,C., DolCetti,G., and Lorca, J. L., *J. Catal.* **151**(1995) 111.

[26]Bunluesin, T., Cordatos, H., and Gorte, R. J., *J.Catal.* **157**(1995) 222.

[27] Bunluesin, T., Grorte, R. J., and Graham, G. W., *Appl. Catal., B* **14**(1997) 105.

[28] Nunan, J. G., Robota, H. J., Cohn, M. J., and Bradley, S. A., *J. Catal.* **133**(1992) 309.

[29] Kalakkad, D. S., Datye, A. K., and Robota, H. J., *J.Catal.* **148**(1994) 729.

[30] Hori, C. E., Permana, H., Simon Ng, K. Y., Brenner, A., More, K., Rahmoeller, K. M., and Belton, D., *Appl. Catal., B* **16**(1998) 105.

[31]Murata, T., Hasegawa, T., Aozasa, S.,Matsui, H., and Motoyama, M., *J. Alloys Compd.* **193**(1993) 298.

[32]Fornasiero, P., Monti, R. D., Rao, G. R., Kaspar, J., Meriani, S.,Trovarelli, A., and Graziani, M., *J. Catal.* **151** (1995) 168.

Chapter 4

Transient analysis of the release and reduction of NOx using a Pt/Ba/Al$_2$O$_3$ catalyst

4-1. Introduction

Lean-burn and diesel engines have great potentials in overcoming the problems of environmental pollution and fuel economy. However, conventional three-way catalysts are ineffective in removing NOx from the exhaust gas of these engines, which contains a large amount of oxygen. One effective method that solves this problem is the use of a NOx storage-reduction (NSR) catalyst [1–5].

NSR catalysts remove NOx by alternating the composition of the exhaust gas between lean and rich. During the lean period of operation, the catalyst stores NOx as species of nitrites and nitrates. A short pulse of rich gas is injected so that the stored NOx is released and reduced to N$_2$. It is generally accepted that this NSR process can be separated into five elemental reactions [6,7]:

(1) NO oxidation to NO$_2$ [8,9].
(2) NOx storage on the catalyst surface [10,11].
(3) Evolution of reductant.
(4) NOx release from the storage site.
(5) NOx reduction to N$_2$.

Despite the general acceptance of this process, the detailed mechanisms are not fully understood, especially the release and reduction of NOx. From a practical point of view, it has been reported that at relatively low temperature the NOx storage capacity is sufficient, but that the rate of NOx release and reduction, sometimes called the NOx regeneration, is slow and insufficient [12]. Analysis of the NOx regeneration is more difficult than that of NO oxidation and NOx storage, because the regeneration accompanied by pulse injection of rich gas is completed in an extremely short period. Another reason for this difficulty is that the main reaction product is N$_2$, which is a significant constituent in real exhaust gases and is usually used for the diluent gas in the laboratory.

Although some studies of transient reaction have been done using He as a diluent gas [10,13–15], it seems that with this even to obtain the time profile of the main product, N$_2$. The aim of the present study is to develop a method to obtain the time profile of N$_2$ with millisecond resolution. Moreover, we would like to improve our understanding of the NOx regeneration process.

Motohiro et al. developed a dynamic vacuum system for transient reaction analysis

of a flat type catalyst on a millisecond timescale (which is essentially a time-resolved time-of-flight mass spectrometry with molecular-pulse-probe for reaction analysis at the surface of catalysts named TM+ since the output raw data is essentially the amount of reaction product cations (+) mapped on the time (T) and mass (M) space) [16–18]. The TM+ system has also blanched out to analyze the transient reaction of a pellet type catalyst [19,20] by reference to the TAP (temporal analysis of products) reactor [21]. We applied both reactor systems in our NSR analysis.

4-2. Experimental

4.2.1. Preparation of a Pt/Ba(NO$_3$)$_2$/cordierite plate for analyzing the decomposition of Ba(NO$_3$)$_2$

Pt and Ba were chosen, respectively, as the precious metal and the NOx storage component for our study because they are well-accepted materials for NSR catalysts. We prepared two kinds of samples for our study, a flat sample and a pellet sample. The latter is described in the next section. The flat sample, 5 nmPt/Ba(NO$_3$)$_2$/cordierite, was fabricated starting with a square cordierite plate, 50 mm on a side and 5 mm thickness. A saturated solution of Ba (NO$_3$) $_2$ (Wako Pure Chemical Industries) of 5 cm^3 was dropped onto the plate, which was then dried in vacuum at room temperature overnight. The resultant sample was then placed in an ultra high vacuum chamber and was sputter-coated with platinum at the amount equivalent to 5 nm in thickness. The resultant sample named 5 nmPt/Ba(NO$_3$)$_2$/cordierite plate was deemed to be a model NSR catalyst, saturated with sites for NOx storage.

4.2.2. Preparation of a pellet type Pt/Ba/Al$_2$O$_3$ catalysts for NSR analyses

Pellets of Pt/Ba/$_{Al2O3}$ catalyst were prepared using a two step wet impregnation method. Firstly, powdery γ-Al$_2$O$_3$ (Nikki Universal, 150 m^2/g) was wet impregnated with Pt(NH$_3$)$_2$(NO$_2$)$_2$ (Tanaka Precious Metals). This material was filtered, washed, dried at 393 K for 12 h, and calcined at 573 K for 3 h in the air. We call this a Pt/Al$_2$O$_3$ sample. Secondly, a portion of this sample was stirred into an aqueous solution containing Ba(CH$_3$COO)$_2$ (Wako Pure Chemical Industries) and the excess water was removed by heating while continually stirring, The resultant powder was dried at 393 K for 12 h and calcined at 773 K for 3 h in the air. The amount of Pt and Ba per 120 g γ-Al$_2$O$_3$ was 2 g and 0.2 mol, respectively. The powder sample was pressed and sieved to make pellets of 0.7–1.0 mm   diameter.

4.2.3. Transient reaction analysis of a flat type catalyst

A flat plate sample of 5 nmPt/Ba(NO$_3$)$_2$/cordierite was placed in the TM+ apparatus shown in Fig. 1. The apparatus was equipped with four pulsed valves, two cryopumps for vacuum chambers placed sample, and two turbo pumps for differentially pumped down chambers and time-of-flight mass spectrometer (TOF-MS). The sample was fixed in a holder with a flat heater and the surface temperature was maintained at 350 °C. Pulses of pure H$_2$ gas

with a volume of 0.2 cm^3 and pulse width of 1 ms were supplied to release and reduce the Ba(NO$_3$)$_2$ in the sample. The reason for choosing H$_2$ was because this is the most effective gas for regeneration of stored NOx at low temperature [22] and because its simple mass peaks of H$_2$ and prospective products makes the analysis of the mass spectra easy. The chambers were kept under high vacuum: the first chamber, where the samples were placed, was at about 10^{-6} Pa; the differential chamber at 10^{-7} Pa, and the chamber for TOF-MS at 10-^{8} Pa. The intensity of each mass peak was calibrated using mass spectral data [23].

The measurement procedure was as follows. After injecting pulse of H$_2$, a part of the reaction products emitted from the catalyst was sampled through a skimmer located in the direction normal to the plane surface of the catalyst. The reaction products were ionized and detected by the TOF-MS on a millisecond scale. This procedure of H$_2$ gas pulsing and detection of the gas products was repeated 100 times with a period of 5 s in order to improve the signal to noise ratio by averaging the accumulated data. The amount of reaction products and NOx in the sample decreased gradually as the progress of Ba(NO$_3$)$_2$ decomposition by H$_2$ gas pulsing because NOx was not supplied to the sample during the measurement. The averaging data were the result of the averaging of the products for 100 times of the measurement, though the amount of the products of each measurement was decreased as the progress of Ba(NO$_3$)$_2$ decomposition. The elemental ratio of the sample surface was measured by X-ray photoelectron spectroscopy (XPS) before and after the H$_2$ pulsing experiment.

4.2.4. Transient reaction analysis of a pellet type catalyst

A 0.2 g pellet of Pt/Ba/Al$_2$O$_3$ catalyst was inserted into a quartz tube with a 4.5 mm internal diameter and a length of 38 mm, as shown in Fig. 2. Silica wool was stuffed into both ends of the quartz tube. A simplified schematic diagram of the TAP-type reactor apparatus is shown in Fig. 2 [19,20], which is installed in the TM+ system mentioned in Section 2.3. The quartz tube containing the catalyst was installed in this vacuum system, which was evacuated to 10^{-7} Pa. The tube was then heated with an external heater up to a preset temperature. For this analysis, we used three valves for the gas pulses, one each for pure O$_2$, NO and H$_2$ gases. The amount of gas in the pulse could be controlled either by the pulse width or by the backpressure of the valve. In this case, the amount of gas was controlled by the backpressure of the valve. The measured pulse width was broader than 1.0 ms preset by a pulsed valve controller because of a gas diffusion effect; nevertheless all the pulse widths were set to 1.0 ms by a pulsed valve controller. The amount of O$_2$ and NO was fixed at about 0.8 and 1.0 cm3 per pulse, respectively. The amount of Ba for NOx storage was calculated to be 3×10^{-7} mol per 0.2 g catalyst, whereas the amount of NO was 3×10^{-4} mol per pulse. Thus, the amount of NO was altogether sufficient for the amount of Ba. The amount of H$_2$ was varied from 0.1 to 0.4 cm^3 per pulse by changing the backpressure of the valve.

The measurement procedure used for this analysis was similar to that used for TM+ type analysis of the flat type catalyst in Section 2.3, and was as follows. After maintaining the catalyst at a preset temperature, an O$_2$ pulse was injected to the catalyst followed by a NO

pulse injection with an interval of 100 ms. This procedure models the NOx storage step, which involves oxidation of NO into NO_2 and storage of NOx. H_2 was injected to the catalyst 5 s after the injections of O_2 and NO pulses in order to bring about NOx regeneration. The NOx storage step was repeated again 200 ms after the H_2 injection. The NOx storage and regeneration was repeated 30 times in order to improve the signal to noise ratio as was done for the analysis of the flat type catalyst. The reactant and product gases were detected for 200 ms after the O_2 pulse injection and for 200 ms after the H_2 pulse injection. In order to accumulate data after the reaction stabilized, the same measurement procedure was repeated 30 times as a pretreatment.
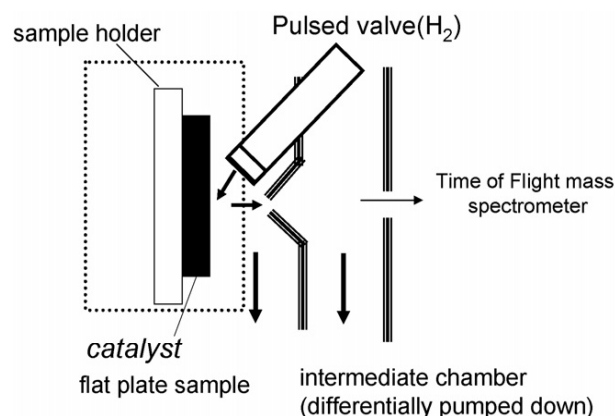
Fig. 1. TM+ apparatus for a flat plate sample. Pulses of reactant gases are supplied through valves. The catalyst sample is set in ultra high vacuum conditions. The gases are analyzed with time-of-flight mass spectrometry through a differentially pumped-down intermediate chamber.
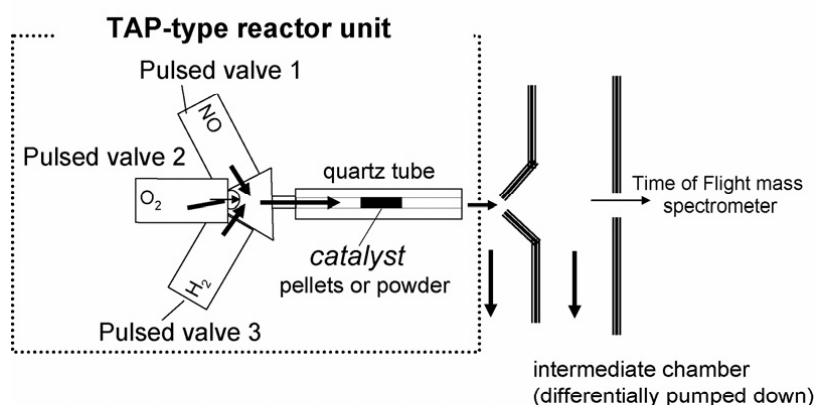
Fig.2. TAP-type reactor apparatus for NSR analysis. Pulses of the reactant gases, NO, O_2 and H_2, are supplied through three separate valves. Catalyst in the form of pellets or powder is placed into a quartz tube. The gases are analyzed in the same way as shown in Fig. 1.

4-3. Results

4..3.1. Ba(NO₃)₂ decomposition analysis

H_2O, NH_3, N_2 and NO were detected with H_2 injection to the flat sample of the 5 nmPt/Ba(NO₃)2/cordierite in the TM+ type measurement as shown in Fig. 3, however N_2O and NO_2 were not detected. When the Ba(NO₃)₂/cordierite without Pt was also analyzed to investigate the role of Pt, none of these products were detected. This indicated clearly that Pt was necessary to release NOx from Ba(NO₃)₂ by H_2. This essential role of Pt for regeneration of NOx was also elucidated recently by an analysis with in situ Fourier Transform Infrared spectroscopy [24]. It was found that both NOx storage and regeneration needs Pt because the role of Pt of NO oxidation to NO_2 in NOx storage process has been well known [25].

The surface elemental composition of the 5 nmPt/ Ba(NO₃)₂/cordierite was measured using XPS before and after the above experiment as shown in Table 1. The reduction in the N/Ba ratio after the experiment confirmed the decomposition of Ba(NO₃)₂. When comparing the surface elemental composition before and after the measurement, it was found that the percentage of Pt decreased while the percentage of Ba increased. It is considered that the sintering of the Pt particles and encapsulation of the Pt particles cause the compositional change. The Pt in the Ba(NO₃)₂/cordierite was unstable and easily sintered into large particles. The phenomenon of the encapsulation of Pt particles by Ba has been observed after the reduction of a barium-based NSR catalyst [26].
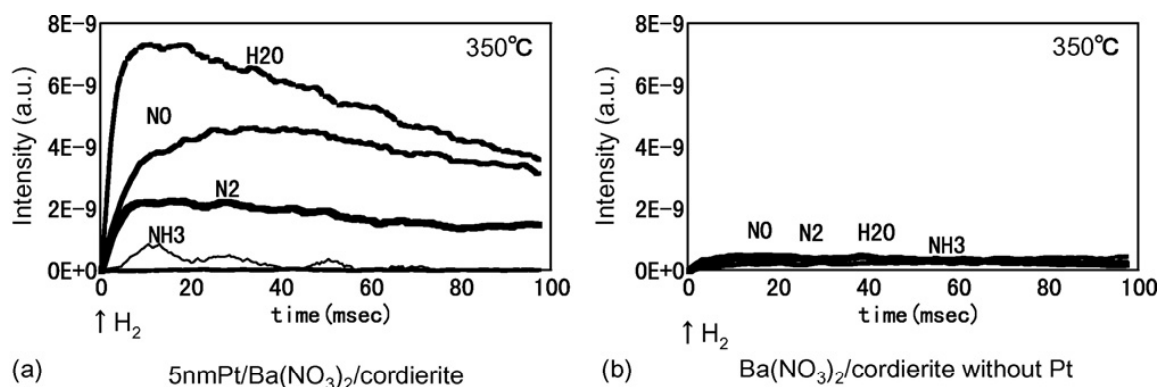
Fig. 3. Time profiles of the gas products generated as a result of Ba(NO₃)₂ decomposition from supplying pulses of H_2 gas to: (a) a flat type sample of 5 nmPt/Ba(NO₃)₂/cordierite ($2MgO_2Al_2O_35SiO_2$) and (b) a flat type sample of Ba(NO₃)₂/ cordierite without Pt at 350 ° C in TM+ type measurement.

Table 1 Surface elemental composition measured with XPS before and after the $Ba(NO_3)_2$ decomposition experiment of 5nmPt/$Ba(NO_3)_2$/cordierite

	Surface elemental composition (%)					N/Ba ratio
	Pt	Ba	N	C	O	
Before	36	3.1	4.0	36	21	1.29
After	15	9.1	4.5	32	40	0.49

4.3.2. Comparison of Pt/Ba/Al₂O₃ with Pt/Al₂O₃ in the TAP type analyses

The results of TAP-type analyses of NSR using the pellet samples of Pt/Ba/Al$_2$O$_3$ and Pt/Al$_2$O$_3$ at 310 °C are shown in Fig. 4. When comparing the profile of NO and O$_2$ of Pt/Ba/ Al$_2$O$_3$ to the one of Pt/Al$_2$O$_3$ (Fig. 4(a and c)), both the signal intensities of NO and O$_2$ of Pt/Ba/Al$_2$O$_3$ were less than the one of Pt/Al$_2$O$_3$. The product gases with H$_2$ injection as the result of NSR reaction were found in the case of Pt/Ba/Al$_2$O$_3$. These results indicated that the NOx was stored in Pt/Ba/Al$_2$O$_3$ and the NSR reaction took place only in the case of Pt/Ba/Al$_2$O$_3$. In our experiment of Pt/Al$_2$O$_3$, the adsorption of NOx on the Pt and Al$_2$O$_3$ [27,28] was not found.

Even though a large amount of NO and H$_2$O were observed in the TM+ type experiment using the 5 nmPt/ Ba(NO3)2/cordierite sample (Fig. 3), NO was not observed here but a small amount of H$_2$O was. We suppose that almost all the NO was reduced to N$_2$ or NH$_3$ immediately and that the H$_2$O desorbed very slowly because of the strong affinity for alumina support. Therefore, the rate-limiting step during the rich phase is the decomposition of barium nitrate [29].
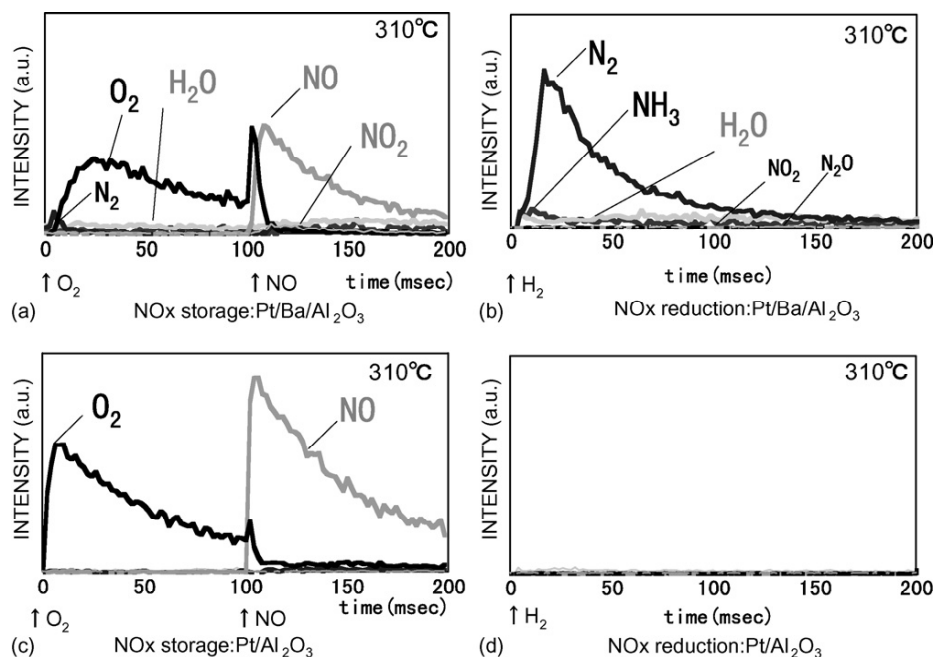
Fig. 4. TAP–type NSR analysis of Pt/Ba/Al$_2$O$_3$ and Pt/Al$_2$O$_3$ at 310 °C : (a) NOx is stored in the Pt/Ba/Al$_2$O$_3$; (b) the stored NOx is reduced by the 0.2 cm^3 pulses of H$_2$ gas, which is supplied 5 s after the NOx storage procedure; (c and d) Pt/Al$_2$O$_3$ does not show the activity of NSR.

4.3.3. Influence of the amount of H$_2$

The influence of the amount of H$_2$ was investigated at 310 °C (Fig. 5). The amounts and ratios of the product and reactant gases changed in response to the increase in the amount of H$_2$ from 0 to 0.4 cm^3. NO and O$_2$ decreased and NH$_3$ increased with the amount of H$_2$ injection on the case between 0 and 0.3 cm^3 H$_2$ injection. In the case of 0.4 cm^3 H$_2$ injection (Fig. 5(j)), the amount of NH$_3$ increased and the amount of N$_2$ decreased in comparison with the result in Fig. 5(i).

We would like to just refer N$_2$ and N$_2$O after the injection of NO. In the case of 0.3 and 0.4 cm3 H$_2$ injection, N$_2$ and N$_2$O were found after the injection of a NO pulse as shown in the magnified views in Fig. 5(d and e). When NO was injected, some of the injected NO was reduced to N$_2$ and N$_2$O at the Pt surface, which was still reduced or absorbed hydrogen despite the previous injection of O$_2$. This reaction was same as NOx selective reduction and NOx direct reduction.
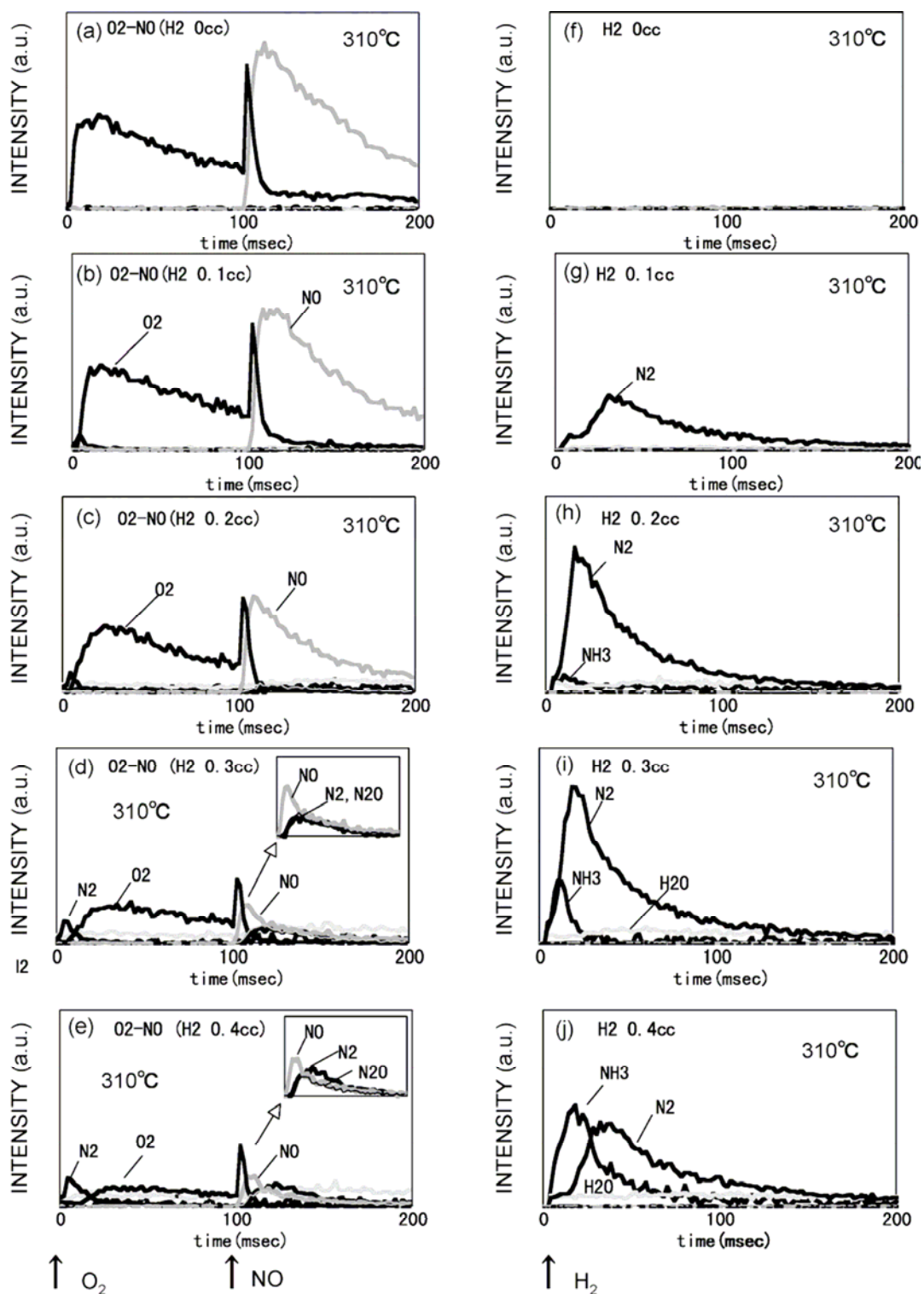
Fig. 5. Effect of the amount of H_2 on the NSR of Pt/Ba/Al$_2$O$_3$ at 310 °C. NO decreases and NH$_3$ increases with increasing amount of H_2.

4.3.4. Influence of temperature

We also investigated the influence of the amount of H_2 on both the products and reactants associated with NOx storage and regeneration at temperatures of 440, 360, 310, 270 and 230 °C. In Fig. 6, the results are displayed in such a manner that the temperature varies in the vertical direction and the amount of H_2 varies in the horizontal direction. The N_2 intensity and the half of the NH_3 intensity were plotted against time. The leading edge of the time profile is generally steeper with increasing H_2 gas volume and increasing temperature. The ratio of NH_3 to N_2 also increases in the same way. We will discuss the rate of NOx release and reduction, and the formation of NH_3 in the next section.

The amount of reduced NOx was calculated at each temperature by subtracting NO profile of each amount of H_2 injection from the NO profile of 0 cm^3 of H_2 injection (Fig. 7). In the case of 0.3 and 0.4 cm^3 H_2 injection, the results agree with the previously known fact that the amount of NOx storage is largest around 350 °C [11,30].
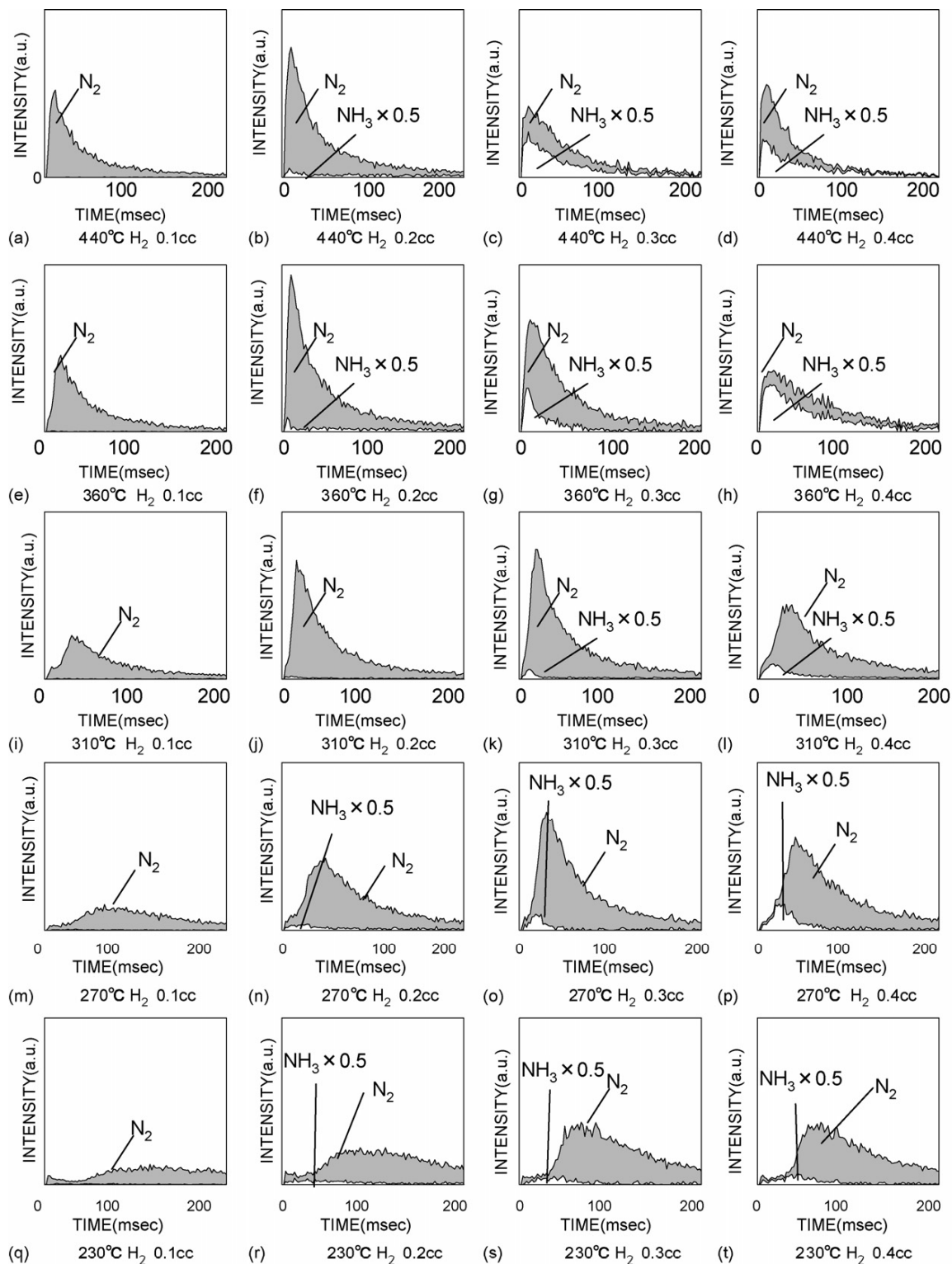
Fig. 6. Effect of temperature and amount of H$_2$ gas pulse on the time profiles of N$_2$ and NH$_3$ after supplying pulses of H$_2$ gas to Pt/Ba/Al$_2$O$_3$.
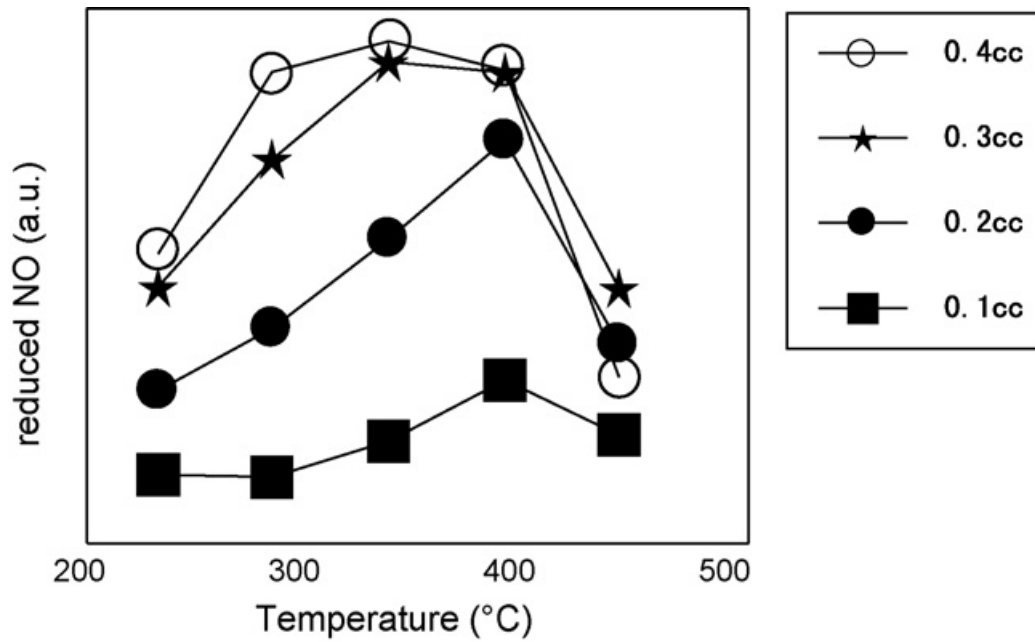
Fig. 7. Amount of reduced NOin the NSR analysis of Pt/Ba/Al$_2$O$_3$. The amount of reduced NO was calculated from the NO profile obtained from the analysis. The profiles are very similar to those of previously reported studies of NSR catalysts by conventional method.

4-4. Discussion

A NSR reaction with H$_2$ gas was investigated on a millisecond time scale using a flat 5 nmPt/Ba(NO$_3$)$_2$/cordierite catalyst and a pellet of Pt/Ba/Al$_2$O$_3$. Instead of the direct comparison of the NOx regeneration rate, we compared the profiles of [N$_2$ + NH$_3$/2]: the sum intensity of N$_2$ and half of NH3. The profiles at each temperature were chosen so as to give almost the same amount of reduced NOx, namely, 0.3, 0.2, 0.2, 0.2 and 0.3 cm^3 at 440, 360, 310, 270 and 230 °C, respectively (Fig. 8(a)). The [N$_2$ + NH$_3$/2] increased as the temperature increases from 230 to 360 °C as described in the previous section and shown in Fig. 7. It was found that the NOx regeneration rate became faster with increasing temperature, as shown by the leading edge of the normalized peak values becoming more rapid as the temperature increases (Fig. 8(b)). To make the difference of the NOx regeneration rate clearer, we tried to fit theoretical curves obtained from a simple reaction model to the [N$_2$ + NH$_3$/2] profiles with a least square method. We assumed a two-step reaction model, whose formula was described as follows [31];

$$dC/dt = K_1 \cdot K_2/(K_1-K_2)C_0(\exp(-K_2t)-\exp(K_1t))$$

Here, t stands for time and dC/dt stands for the intensity: [N$_2$ + NH3/$_2$]. The K$_1$ stands for the

41

rate constant of the first step reaction and the K_2 stands for the one of the second step. C_0 is considered as the concentration of the stored NOx. If we assume the first step as NOx release and the second step as NOx reduction, we are able to have the each rate constant. An example of the fitting was shown in Fig. 9(a). The fitting seems to be successful. This fitting was performed to other time profiles of 0.3 cm^3 of H_2 injection. As shown in Fig. 9(b), the temperature dependences of K_1, K_2 and the amount of reduced NO for 0.3 cm3 H_2 injection. The rate constant of K_1 and K_2 increased with increase in temperature from 230 to 440 °C, while the temperature dependence of the amount of reduced NOx shows a maximum value around 300 °C. From this analysis, we suppose that the amount of reduced NOx was decreased above 360 °C because of the decrease of the NOx storage reactivity in Pt/Ba/Al$_2$O$_3$. If we assume the first step as NOx release and the second step as NOx reduction as mentioned above, it is considered that the rate constant of NOx release and NOx reduction between 230 and 310 °C are almost the same. When the temperature increase over 360 °C, the rate constant for NOx release was found to be larger than the one for NOx reduction. When the temperature was increased to 440 °C, a large amount of NH$_3$ was yielded. This NH3 formation may be connected with the small rate of NOx reduction over 360 °C. At last, we would like to discuss NO storage reaction in NSR reaction and NH$_3$ formation in NOx regeneration. It is clear that the profiles of O$_2$ and NO are different in the NOx storage process shown in Fig. 5. The leading edge of the O$_2$ profile became gentler as the amount of H$_2$ increased, but the leading edge of the NO profile remained stable. This difference may indicate the difference between the reaction mechanisms of O$_2$ and NO with Pt/Ba/Al$_2$O$_3$, i.e., O$_2$ reacted with Pt/Ba/Al$_2$O$_3$ very fast and NO did not. When O$_2$ is injected to the Pt/Ba/ Al$_2$O$_3$, the surface reduced by H$_2$ can adsorbed O$_2$ immediately. However, NO needs to react with dissociated oxygen for NOx storage [32–34] and therefore the rate of NO reaction was not faster than the one of O$_2$ reaction.
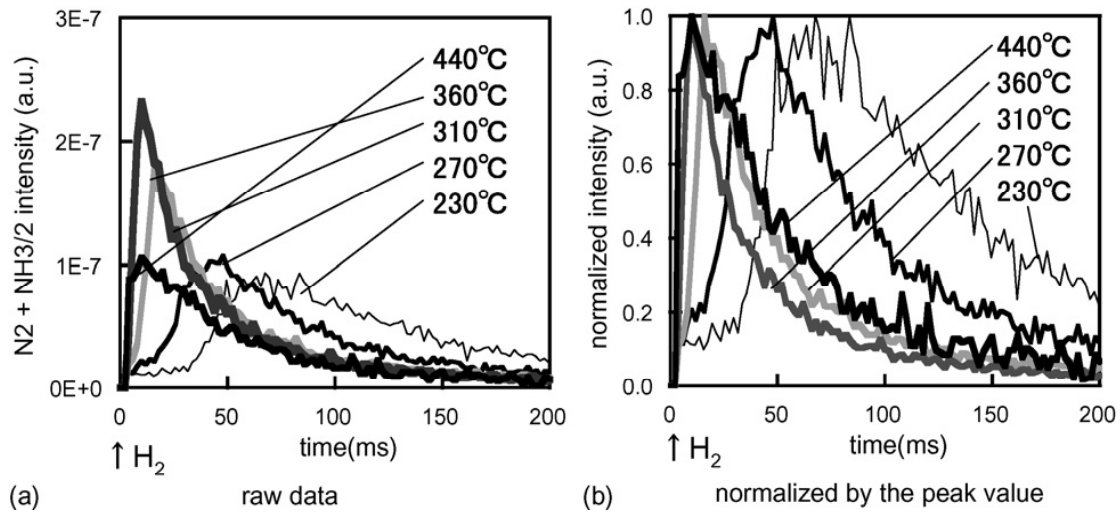
Fig. 8. Comparison of the $N_2 + NH_3/2$ profile (a) raw data and (b) normalized by the peak value.

A detailed report on NOx regeneration in a NSR catalyst was recently published [35]. Although the report focused mainly on the effect of different reducing agents and precious metals, NH_3 formation in NOx regeneration is also discussed. The result of the discussion showed that the amount of NH3 increased as the temperature increased, which is the same as the result found in this work (Fig. 6). Another analysis showed that the generation of N_2 and the subsequent generation of NH_3 [36] accompany the introduction of H_2. The order in which these gases were generated is opposite to our result. The difference may be presumably due to the difference in the methods of H_2 introduction, i.e., pulsed injection in our case and step injection in the reference [36] in which the time profile of induced H_2 increases rapidly and then becomes stable. NH_3 formation tends to occur when the ratio of H_2 to NO increases [37]. In our study, the H_2/NO ratio is high just after H_2 pulse injection because the H_2 concentration is considered to be highest at that time and decreases rapidly from then on. On the other hand, in the study using a step profile for H_2, the H_2/NO ratio is low just after injection because a large amount of NO exists in the catalyst and the H_2/NO ratio is considered to increase gradually from then on. We regard this as the reason why the order of N_2 and NH_3 generation was different between the two works. The formation of NH_3 and intermediate gases caused by CO and hydrocarbons [38] has often been discussed. This can be neglected in our case, because these reducing agents were not used in this study. However, the NH_3 may play an important role in NOx release and reduction. Further analysis is necessary such as using NH3 directly as a reducing agent for stored NOx.
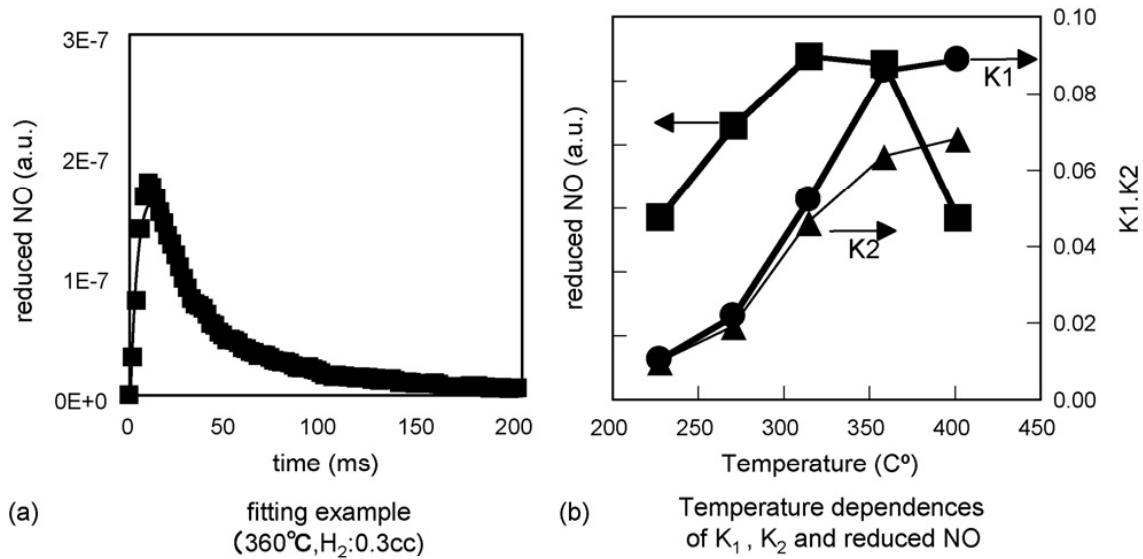
43

(a) fitting example
(360°C,H₂:0.3cc)

(b) Temperature dependences
of K₁, K₂ and reduced NO

Fig. 9. Temperature dependences of the speed of NOx regeneration and the amount of NOx reduced using the data of 0.3 cm^3 of H$_2$ injection: (a) a fitting example of N$_2$ + NH$_3$/2 profile at 360 $^\circ$C and (b) temperature dependences of K$_1$, K$_2$ and reduced NO: the same data in Fig. 7.

4-5. Conclusions

NOx regeneration in an NSR catalyst with H$_2$ gas was investigated on a millisecond time scale. As for the gases produced as a result of NOx regeneration, NO, N$_2$, NH$_3$ and H$_2$O, were detected from a flat 5 nm Pt/Ba(NO$_3$)$_2$/cordierite catalyst, though no products were detected from Ba(NO$_3$)$_2$/ cordierite. It was found that Pt plays an important role in the NSR reaction and that NO was produced from decomposition of Ba(NO$_3$)$_2$ in the catalyst.

A NSR reaction using a pellet of Pt/Ba/Al$_2$O$_3$ as the catalyst was also investigated. The results were different from the analysis using the flat catalyst in which only a small amount of H$_2$O was detected because of the strong affinity for alumina support. NO was not observed since it was reduced into N$_2$. For a large amount of H$_2$ injection, a large amount of NH$_3$ was detected. Analysis both of the N$_2$ profile and their leading edges showed that the rate of NOx regeneration increased with temperature and the amount H$_2$. We can analyze the NOx regeneration process to separate two steps of the NOx release and reduction by a detailed analysis of the time profiles using a two-step reaction model. From the result of the analysis, it is found that the rate constant for NOx release increased as temperature increase.

References

[1] N. Miyoshi, S. Matsumoto, K. Katoh, T. Tanaka, J. Harada, N. Takahashi, K. Yokota, M. Sigiura, K. Kasahara, SAE Tech. Papers Ser. 950809, 1995.

[2] W. Bo¨gner, M. Kra¨mer, B. Kreutzsch, S. Pischinger, D. Voigtla¨nder, G. Wenninger, F. Wirbeleit, M.S. Brogan, R.J. Brisley, D.E. Webster, Appl. Catal. B 7 (1995) 153.

[3] N. Takahashi, H. Shinjoh, T. Iijima, T. Suzuki, K. Yamazaki, K. Yokota, H. Suzuki, N. Miyoshi, S. Matsumoto, T. Tanizawa, T. Tanaka, S. Tateishi, K. Kasahara, Catal. Today 27 (1996) 63.

[4] E. Fridell, M. Skoglundh, S. Johansson, B. Westerberg, A. To¨rncrona, G. Smedler, Stud. Surf. Sci. Catal. 116 (1998) 537.

[5] H. Hirata, I. Hachisuka, Y. Ikeda, S. Tsuji, Si Matsumoto, Top. Catal. 16/ 17 (2001) 145.

[6] W.S. Epling, L.E. Campbell, A. Yezerets, N.W. Currier, J.E. Parks, Catal. Rev. Sci. Eng. 46 (2) (2004) 163.

[7] W.S. Epling, J.E. Parks, G.C. Campbell, A. Yezerets, N.W. Currier, L.E. Campbell, Catal. Today 96 (2004) 21.

[8] L. Olsson, B. Westerberg, H. Persson, E. Fridell, M. Skoglundh, B. Andersson, J. Phys. Chem. B 103 (1999) 10433.

[9] P. Denton, A. Giroir-Fendler, H. Praliaud, M. Primet, J. Catal. 189 (2) (2000) 410.

[10] S. Salasc, M. Skoglundh, E. Fridell, Appl. Catal. B 36 (2002) 145.

[11] H. Mahzoul, J.F. Brilhac, P. Gilot, Appl. Catal. B 20 (1999) 47.

[12] J. Sjo¨blom, K. Papadakis, D. Creaser, C.U.I. Odenbrand, Catal. Today 100 (2005) 243.

[13] L. Lietti, P. Forzatti, I. Nova, E. Tronconi, J. Catal. 204 (2001) 175.

[14] D. James, E. Fourre´, M. Ishii, M. Bowker, Appl. Catal. B 45 (2003) 147.

[15] N.W. Cant, M.J. Patterson, Catal. Today 73 (2002) 271

[16] T. Motohiro, Y. Kizaki, Y. Sakamoto, K. Higuchi, Y. Watanabe, S. Noda, Appl. Surf. Sci. 121/122 (1997) 319.

[17] T. Motohiro, Y. Kizaki, Y. Sakamoto, K. Higuchi, T. Tanabe, N. Takahashi, K.Yokota, H.Doi, M. Sugiura, S.Noda, Appl. Surf. Sci. 121/122 (1997) 323.

[18] Y. Sakamoto, Y. Kizaki, T. Motohiro, Y. Yokota, H. Sobukawa, M. Uenishi, H. Tanaka, M. Sugiura, J. Catal. 211 (2002) 157.

[19] T. Nakamura, Y. Sakamoto, K. Saji, J. Sakata, Sens. Actuators B 93 (2003) 214.

[20] M. Uenishi, H. Tanaka, M. Taniguchi, I. Tan, Y. Sakamoto, S. Matsunaga, K. Yokota, T. Kobayashi, Appl. Catal. A 296 (2005) 114.

[21] S.O. Shekhtman, G.S. Yablonsky, S. Chen, J.T. Gleaves, Chem. Eng. Sci. 54 (1999) 4371.

[22] S. Poulston, R.R. Rajaram, Catal. Today 81 (2003) 603.

[23] A. Cornu, R. Massot, Complication of Mass Spectral Data, second ed., Heyden & Son, 1975.

[24] Y. Su, M.D. Amiridis, Catal. Today 96 (2004) 31.

[25] R. Burch, T.C. Watling, Stud. Surf. Sci. 116 (1998) 199.

[26] P.T. Fanson, M.R. Horton,W.N. Delgass, J. Lauterbach, Appl. Catal. B 46 (2003) 393.

[27] T.J. Toops, D.B. Smith, W.P. Partridge, Appl. Catal. B 58 (2005) 245.

[28] D. Uy, K.A. Weigand, A.E. O'Neill, M.A. Dearth, W.H. Weber, J. Phys. Chem. B 106

(2002) 387.

[29] E. Fridell, M. Skoglundh, B. Westerberg, S. Johansson, G. Smedler, J. Catal. 183 (1999) 196.

[30] S. Matsumoto, Catal. Today 29 (1996) 43.

[31] K. Ohkubo, Y. Igari, S. Tomoda, I. Kusunoki, Surf. Sci. 260 (1992) 44.

[32] E. Fridell, H. Persson, B. Westerberg, L. Olsson, M. Skoglundh, Catal. Lett. 66 (2000) 71.

[33] L. Olsson, E. Fridell, M. Skoglundh, B. Andersson, Catal. Today 73 (2002) 263.

[34] X. Li, P. Vernoux, Appl. Catal. B 61 (2005) 267.

[35] H. Abdulhamid, E. Fridell, M. Skoglundh, Appl. Catal. B 62 (2005) 319.

[36] L. Castoldi, I. Nova, L. Lietti, P. Forzatti, Catal. Today 96 (2004) 43.

[37] Y.J. Mergler, B.E. Nieuwenhuys, Appl. Catal. B 12 (2–3) (1997) 95.

[38] T. Lesage, C. Verrier, P. Bazin, J. Saussey, M. Daturi, Phys. Chem. Chem. Phys. 5 (2003) 4435.

Chapter 5

Effect of precious metals and NOx storage materials on hydrogen reduction of stored NOx

1. Introduction

To protect the global environment, a worldwide reduction in CO_2 emissions is required. High fuel-efficiency lean-burn engine technology is a promising method for alleviating the CO_2 emission problem in automotive applications. However, the emissions from lean-burn engines include NOx production under oxygen-rich conditions, and the reduction of NOx is extremely difficult under such conditions. On the basis of the considerable research conducted on various methods, a NOx storage and reduction (NSR) catalyst for automobiles was put into practical use in 1994 by the Toyota Motor Corporation [1,2].

An NSR catalyst has the ability to reduce NOx, even under oxygen-excess conditions, using two operations: first is the storage of NOx using alkali or alkali earth materials under oxygen-rich conditions, and second is the reduction of stored NOx under oxygen-poor conditions produced by a short-period, rich pulse of reducing gases. The alternate repetition of these storage and reduction operations results in the reduction of NOx to nitrogen. To develop efficient NSR techniques with low fuel cost, it is necessary to investigate the reaction mechanisms involved. It is suggested that the reduction of stored NOx is the rate limiting step in the overall NSR process at low temperature [3]. The evaluation of the rate at which stored NOx is reduced requires measurement of the time profiles of the products produced during the reduction process. However, it is difficult to measure these products because the reaction is usually very fast and the main product is gaseous nitrogen, which is also a normal emission product from engines and is used as a model gas in laboratory tests.

We previously reported the comparison results of NOx reduction processes with $Pt/Ba/Al_2O_3$ and $Pt/K/Al_2O_3$ catalysts by analyzing the NOx reduction using a temporal analysis of products (TAP) reactor [4,5]. The TAP method was developed by Gleaves et al. [6] and is widely recognized as an effective method for transient reaction analysis [7]. From our analysis, we found that the reduction rate of stored NOx using $Pt/K/Al_2O_3$ was faster than that using $Pt/Ba/Al_2O_3$, and the ratio of N_2 to NH_3 produced in the reaction was affected by different catalysts. The NOx storage process in potassium has also been studied [8,9,10,11]. Potassium-containing materials show strong potential as NOx storage materials (NSMs) and as a NOx selective-reduction catalyst [12].

Many scientists have studied the effect of precious metals (PMs) on NSR activity in order to improve the performance of NSR catalysts. In particular, Abdulhamid et al. studied the effect of different reducing agents (H_2, CO, C_3H_6, and C_3H_8) on the reduction of stored NOx

47

over PM/BaO/Al$_2$O$_3$ catalysts (PM = Pt, Pd, or Rh) [13]. The reduction of stored NOx was shown to be strongly affected by the type of PM used. Su et al. compared Pt/BaO/Al$_2$O$_3$ and Pd/BaO/Al$_2$O$_3$ catalysts for NSR and found that the latter exhibited higher overall NOx reduction activity at temperatures between 523 K and 623 K [14]. It was suggested that this result was due to the higher effectiveness of Pd in promoting the reaction with C$_3$H$_6$, which leads to an improved NOx storage reaction and higher storage capacity.

These results have motivated us to investigate the effect of combining different PMs (Pt, Rh, and Pd) and NSMs (Ba, K, and Na) for NSR processes in order to design an efficient NSR catalyst. In this investigation, a TAP reactor was employed for the analysis.

2. Experimental

Sample preparation and analysis of the NSR catalysts were conducted using previously reported methods [5]. Nine catalysts were prepared for NSR analysis: PM/NSM/Al$_2$O$_3$ (PM = Pt, Rh, Pd; NSM = Ba, K, Na). The catalysts were prepared using a two-step wet impregnation method. In the first step, powdered γ-Al$_2$O$_3$ was wet-impregnated with a PM salt solution. The material was filtered, washed, dried at 393 K for 12 h, and then calcined at 573 K for 3 h in air. In the second step, the sample was stirred into an aqueous solution containing alkali earth or alkali metal salts, and the excess water was removed by heating with continuous stirring. The resultant powder was dried at 393 K for 12 h and then calcined at 773 K for 3 h in air. The amounts of PM and alkali earth/alkali metal were 2.0 g and 0.2 mol per 120 g γ-Al$_2$O$_3$, respectively. The powder sample was then sieved and uniaxially pressed at 10 MPa to form pellets of diameter 0.7–1.0 mm. The PM dispersion ratio and surface area of each sample were evaluated using CO adsorption and Brunauer, Emmett, and Teller (BET) surface area measurement methods.

Pellets containing 0.2 g of catalyst were inserted into a quartz tube (id: 4.5 mm, length: 38 mm). Silica wool was then plugged into both ends of the tube, and the tube was inserted into the reactor. After the NSR catalyst sample was set, O$_2$, NO, and H$_2$ were separately injected in series as pulsed gases into the tube (Figure 1), and the reactants and products were detected using time-of-flight mass spectrometry (TOF-MS). The duration that the pulse valve was maintained in the open position was usually controlled from sub milliseconds to a few milliseconds. First, an O$_2$ pulse was injected to oxidize the surface of the catalyst, and after 100 ms, an NO pulse was injected. We then determined whether the catalyst was sufficiently oxidized by evaluating the N$_2$ production during NO pulsing. The O$_2$ and NO pulses caused the formation of NOx that was stored in the catalyst. H$_2$ was used as a reductant for stored NOx, because H$_2$ is a more effective reductant than CO or hydrocarbons [15,16]. A pulse of H$_2$ was injected 5 s after the NO pulse; this time period was considered sufficient to clear any excess and weakly adsorbed gases from the catalyst under ultra vacuum conditions because neither of the reactant gases could be detected after 5 s. This sequence was repeated at 5 s intervals as a pretreatment until the reactant profiles stabilized. The data obtained from the last 30 sequences were averaged to increase the signal-to-noise ratio. The amounts of O$_2$, NO,

and H$_2$ were fixed at approximately 3.5×10^{-6}, 4.5×10^{-6}, and 7×10^{-6} mol/pulse, respectively. The amount of NSM that was available for NOx storage was calculated to range from 1×10^{-4} to 2×10^{-4} mol per 0.2 g of catalyst, which was sufficient given the amount of supplied gas.

While the TOF spectra were measured every 2.0 ms in our previous report [4,5], the time resolution was improved to 0.25 ms in the current study in order to analyze the details of the NSR process. The Y-axis values were estimated as molecules/millisecond by using the method described in our previous paper [17], although the standard Ar supplied pulse gas was not used in this experiment. The time profiles of the products were measured at intervals of 40 K as the temperature was decreased from 718 K to 503 K.
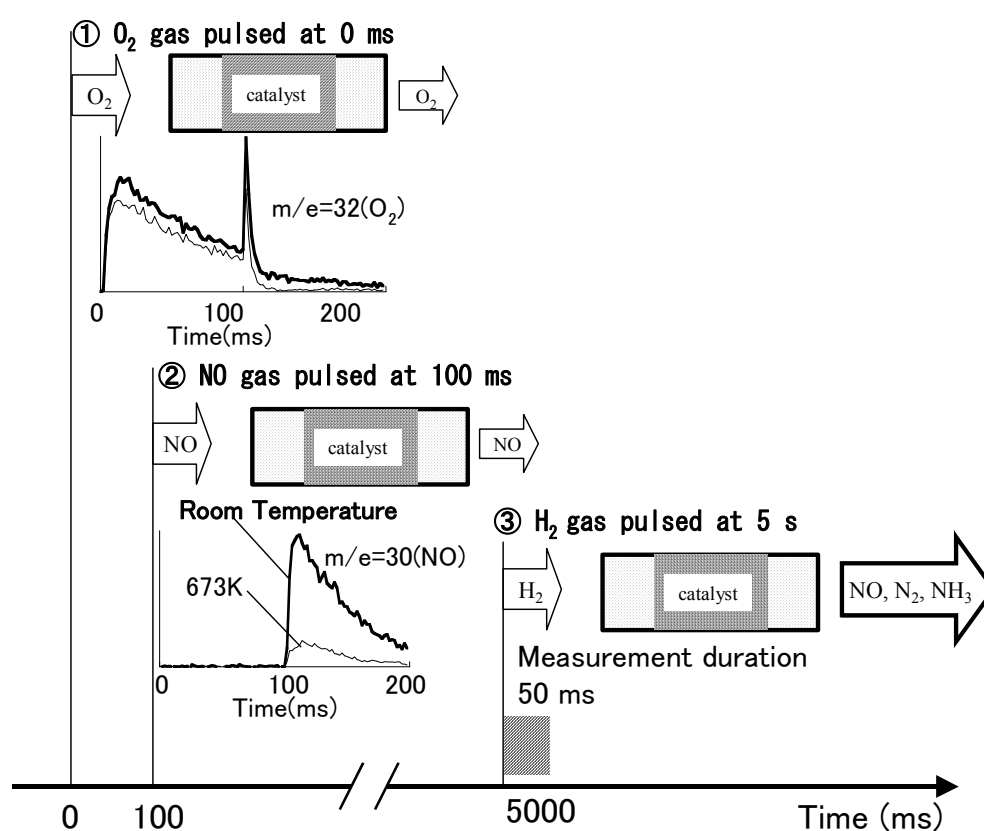
Figure 1. Schematic illustration of the experimental method. Gas pulses are passed through a catalyst in a quartz tube. An O$_2$ pulse, followed 100 ms later by a NO pulse, is supplied to the catalyst during the NOx storage process. Five seconds after the NOx storage process is complete, a H$_2$ pulse is supplied to initiate NOx reduction. Portions of the reactant and product gases are detected using a time-of-flight mass spectrometer.

3. Results

Table 1 shows the PM dispersion ratio and BET surface area of each sample. The PM dispersion ratio was nearly the same for each type of PM. The BET surface area for all of the samples was between 102 m^2/g and 130 m^2/g. These results indicate that the NSM does not affect the PM dispersion ratio or the BET surface area. The loaded amount of PM for each sample was 2.0 g per 120 g γ-Al_2O_3. Given the molar weight (Pt: 195, Rh: 103, Pd: 106) and the dispersion ratio of the PMs (Table 1), the surface area of Rh was approximately two times larger than those of Pt and Pd, except for Rh-K. The largest surface area for Rh in Rh–Ba and Rh–K was expected to exhibit higher catalytic activity.

The time profiles of N_2, NH_3, and NO production are shown in Figures 2, 3, and 4, respectively. It is clear that the amount and time profile of each product were very different for different combinations of PM and NSM. All of the profiles became sharper as the temperature increased. N_2O and NO_2, which are considered to be products of NSR, were not detected in the experiment. This result may be due to the low oxygen concentration because the selectivity of N_2O and NO_2 decreases with decreasing O_2 concentration in the presence of a Pt–Ba catalyst [18].

The time profiles of N_2 for the Pt-based catalysts at identical temperatures became sharper in the increasing order of Pt–Ba (Figure 2(a)), Pt–K (Figure 2(d)), and Pt–Na (Figure 2(g)). The formation rate of N_2 products with Pt–K is higher than that with Pt–Ba (Figure 2(d)) [4]. Therefore, it is suspected that the variation is caused by the difference in the decomposition temperatures of $Ba(NO_3)_2$, KNO_3, and $NaNO_3$, which are 592, 400, and 380 °C, respectively.

The relationship between the type of PM and the time profile of N_2 is also of interest. For Pt–Ba (Figure 2(a)), Rh–Ba (Figure 2(b)), and Pd–Ba (Figure 2(c)) with the same NSM but different PM, the production rate of N_2 in Pt–Ba was found to be the fastest. The N_2 production rate of both Pt–Ba and Pd–Ba began to decrease at approximately 10 ms, which was considered to be due to the production of NH_3. Furthermore, an increase in the NH_3 yield can be observed in Figures 3(a) and (c). Of the three catalysts, only Rh–Ba yielded NO. Both Pt–Ba and Pd–Ba exhibited high N_2 and very low NO production rates. In contrast, Rh–Ba displayed a lower N_2 and a higher NO production rate. In addition, no NH_3 production was observed for Rh–Ba. It should be noted that only the Rh-based catalysts produced significant amounts of NO. Only Rh–K did not produce N_2 and NH_3. The lowest dispersion ratio of Rh–K among the Rh-containing catalysts may result in very low levels of N_2 and NH_3 production. The details of the reactivity and selectivity are discussed in the following section.
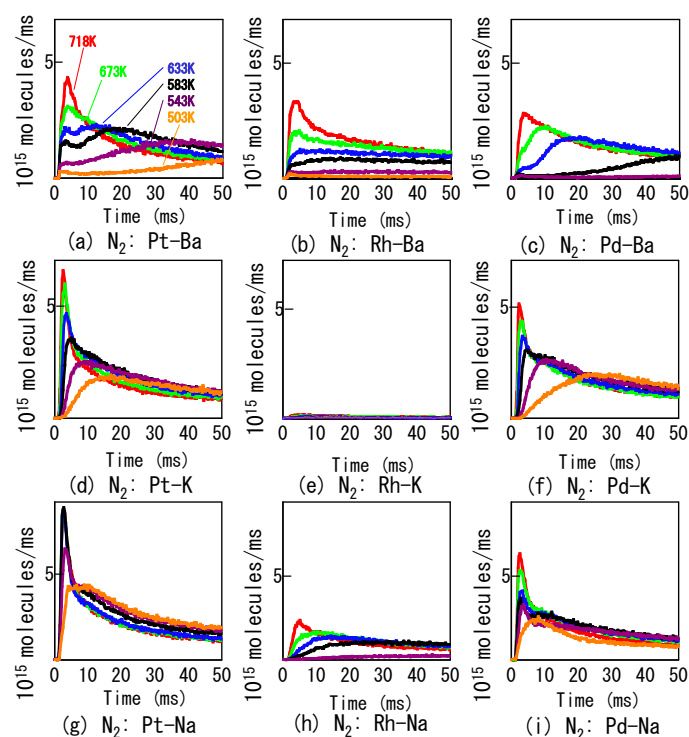
Figure 2. Temperature-dependent time profiles of N_2 production for different NSR catalysts. All profiles became sharper as the temperature increased.
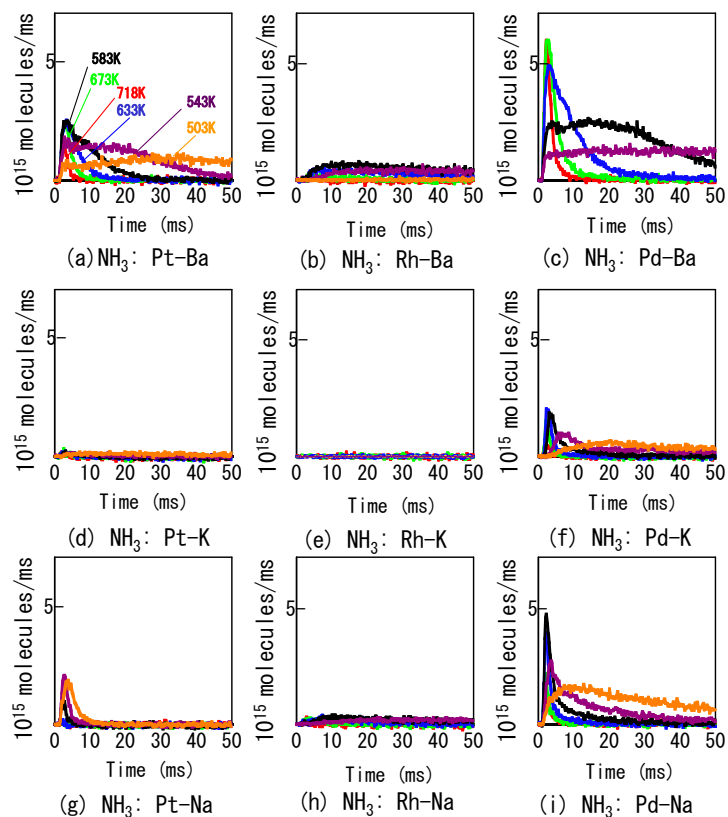

Figure 3. Temperature dependence of the time profiles for the production of NH_3 for different NSR catalysts.
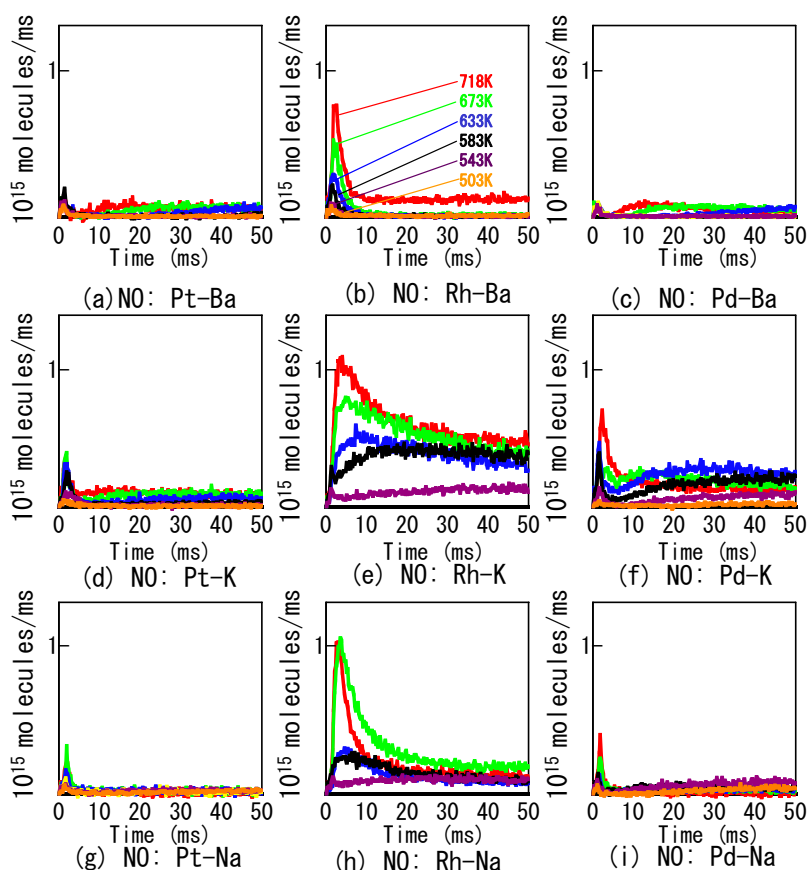
Figure 4. Temperature dependence of the time profiles for the production of NO for different NSR catalysts.

4. Discussion

The two main points of discussion are

1) the selectivity of products during the reduction of stored NOx and

2) the reduction rate of stored NOx.

The reduction scheme for stored NOx (the regeneration process) is shown in Figure 5. The reactions yielding N_2O and NO_2 were neglected because neither product was detected in the experiments. The production of H_2O was also ignored because the H_2O signals were very weak, and the profiles were broadened because of strong adsorption. The supplied hydrogen from the pulsed valve reacts on the PM and NSM via routes R_1, R_4, and R_6. The activated hydrogen generated in R_1 spills over via R_2 and reacts with stored NOx in the NSM via R_3. The reacted NOx species are then converted to gas phase NH_3, N_2, and NO. Some of the reacted species then spill over to the PM via R_5 for reduction on the PM via R_6.

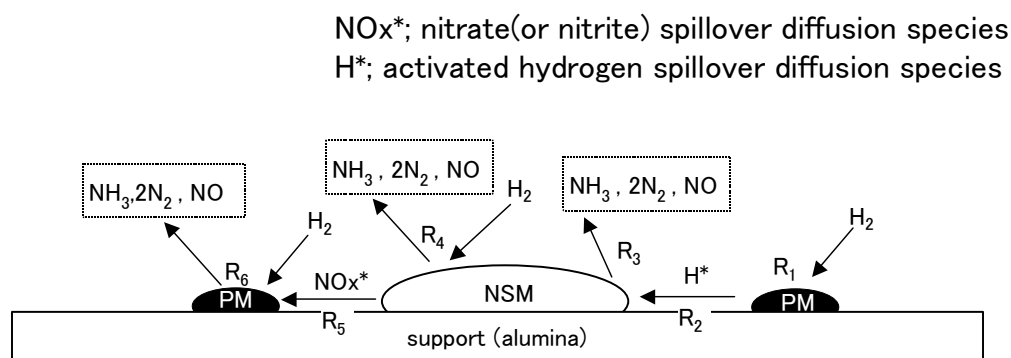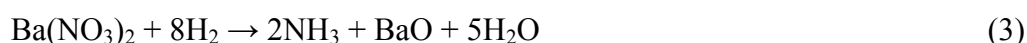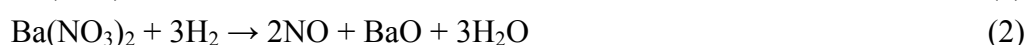Figure 5. Model for the analysis of NOx storage and reduction.

On the basis of the above model, the reduction rate of stored NOx and the selectivity of the products during the reduction were determined by the following factors:

A) The H_2 dissociation ability of the PM,

B) the ease of reduction of the NSM nitrate/nitrite (decomposition temperature),

C) the NOx concentration in the NSM, and

D) the interface area between the PM and NSM.

If the H_2 dissociation ability of the PM is higher, the selectivity for NH_3 and the reduction rate will increase. If the ease of reduction of the NSM nitrate/nitrite is enhanced, the selectivity for NH_3 will decrease and the reduction rate will increase. If the NOx concentration in the NSM is increased, the selectivity for NH_3 will decrease and the reduction rate will increase. If the interface area between the PM and NSM is larger, the reduction rate will increase. The production rate of NOx* and H* spillover species will determine the reduction rate of stored NOx, and its ratio will decide the selectivity of the products.

First, the reduction of stored NOx (the regeneration process) in the case of the Pt–Ba catalyst, which is the most popular of the NSR catalysts, was considered based on the model. The reduction of stored NOx on a Pt–Ba catalyst was not initiated by the thermal release of NOx in the gas phase, but occurred through a Pt-catalyzed reduction of adsorbed NOx species [19] as shown in Eqs. (1)–(3), via R_3 and R_4 in Figure 5. In addition, it has been suggested that the NS site is converted to BaO rather than to $Ba(OH)_2$ during long-term soaking of the Pt–Ba catalyst in NO + H_2 [20].

$$Ba(NO_3)_2 + 5H_2 \rightarrow N_2 + BaO + 5H_2O \qquad (1)$$
$$Ba(NO_3)_2 + 3H_2 \rightarrow 2NO + BaO + 3H_2O \qquad (2)$$
$$Ba(NO_3)_2 + 8H_2 \rightarrow 2NH_3 + BaO + 5H_2O \qquad (3)$$

The reactions yielding N_2O and NO_2 were neglected because neither product was detected in the experiments. NO and NH_3 formed by the Pt-catalyzed reduction of adsorbed NOx species (Eqs. (2) and (3)) can be converted to N_2, NH_3, and H_2O, as shown in Eqs. (4)–(6), via R_6 in Figure 5.

$$2NO + 5H_2 \rightarrow 2NH_3 + 2H_2O \qquad (4)$$
$$6NO + 4NH_3 \rightarrow 5N_2 + 6H_2O \qquad (5)$$
$$2NO + 2H_2 \rightarrow N_2 + 2H_2O \qquad (6)$$

NH_3 reacts negligibly with NO in the presence of H_2 [21]. Thus, reaction (5) may be neglected in the initial stages of the experiment, because a large amount of hydrogen is supplied for a very short time. Therefore, the produced NH_3 passes through without reacting with NO.

It is believed that similar reactions occurred for all of the catalysts. To more clearly compare the selectivity, data from Figures 2, 3, and 4 were combined to prepare time profiles of $NH_3 + 2N_2 + NO$ at 718 K and 583 K, as shown in Figures 6 and 7, respectively.

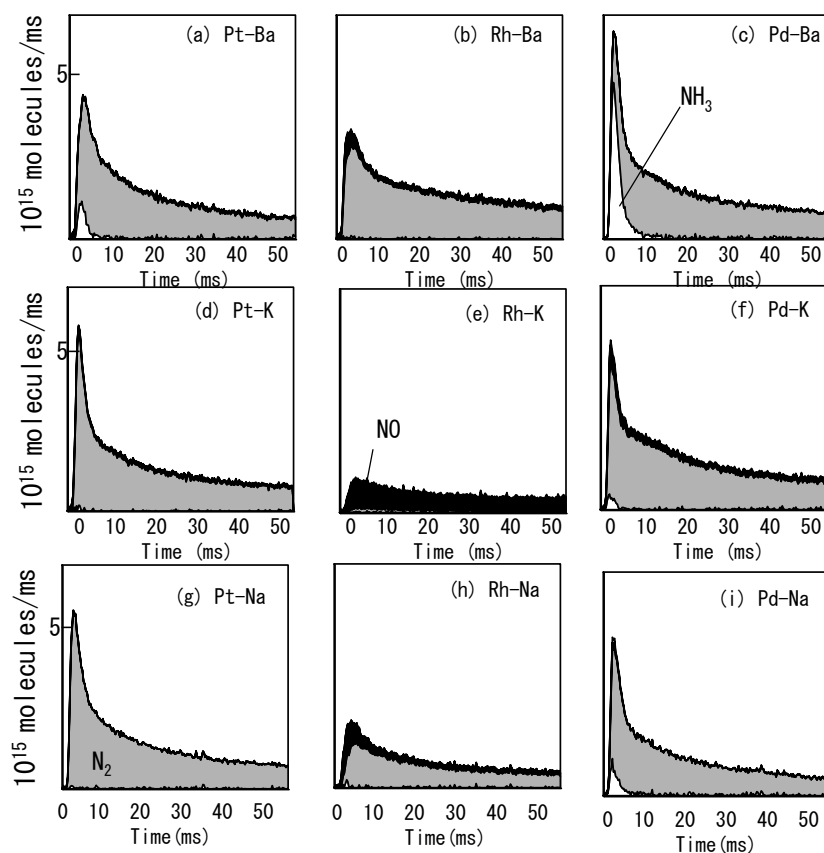Figure 6. Time profiles for the sum of the $NH_3 + 2N_2 + NO$ production at 718 K.

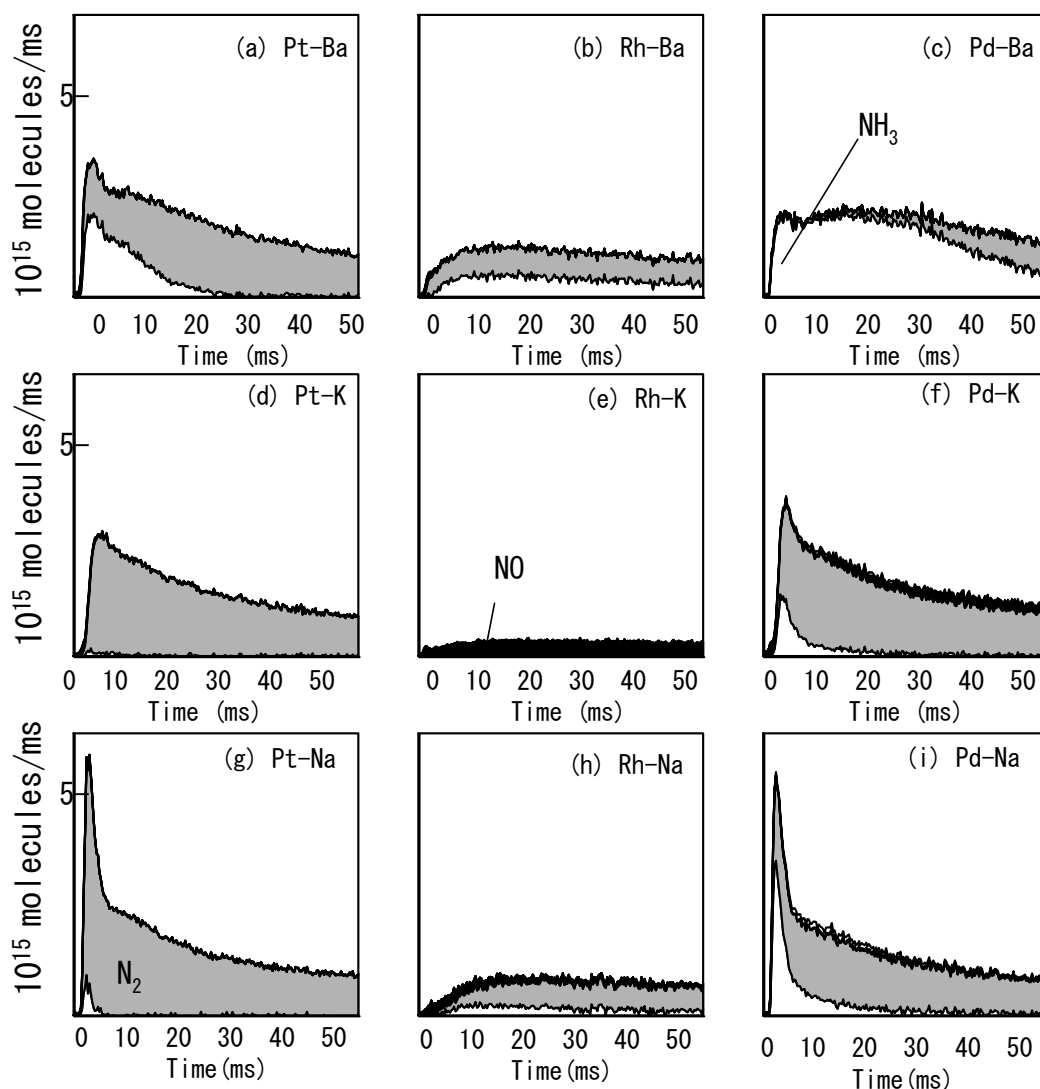Figure 7. Time profiles for the sum of the $NH_3 + 2N_2 + NO$ production at 583 K

Epling et al. investigated NH_3 formation with NSR catalysts using both lean and rich inlet gases [22]. They reported that NH_3 is readily formed at temperatures below 648 K when sufficient or excess H_2 is present with N-species on the catalyst for the amount of stored NOx [23]. The generated NH_3 acts as a reductant and reacts with the nitrate decomposition products on the PM sites via the known selective catalytic reduction reaction [24]. In the present study, NH_3 was detected during H_2 pulsing when the ratio of H_2 to stored NOx was high; however, NH_3 was not detected at high temperatures, which is also consistent with the results reported by Epling et al. [22].

It is clear that catalysts that include Pt or Pd have similar tendencies for NSR; however, the Rh-based catalysts behave differently, as exemplified by Rh–K that exhibited very different selectivity such that no NH_3 was produced (Figure 3(e)). The difference between the activities of the Rh-based and Pt/Pd-based catalysts for NH_3 formation is consistent with previous reports [13,25]. According to the model in Figure 5, the reasons for low NH_3 selectivity of the Rh-containing catalysts are the low H_2 dissociation ability of the PM, ease

of reduction of the NSM nitrate/nitrite, and high NOx concentration in the NSM. Our previous analysis of the NO + H_2 reaction on a PM without NSM in this reactor indicated the low selectivity for NH_3 of Rh [26]. From this fact, the low H_2 dissociation ability of Rh is considered as a key factor. The main route that yields N_2 is R_5, which involves NOx spillover from the NSM to PM. The low yield of NH_3 for Rh–K may thus be due to the low dispersion of Rh. The lower decomposition temperature of K and Na compared with Ba also increases the amount and rate of NOx* production. Therefore, It is believed that NH_3 formation for K and Na is less than that for Ba because the ratio of NOx* to H* increases.

Next, the reduction rate of stored NOx was reviewed. Figure 8 shows the temperature dependence of the combined time profiles for $NH_3 + 2N_2 + NO$ production. The NSR time profiles were analyzed using a simple model of a two-step process [4]. Two reaction steps can be proposed at the initial stage of the regeneration reaction: a nitrate (or nitrite) diffusion limiting process and an activated hydrogen spillover limiting process. For the nitrate (or nitrite) diffusion limiting process, when H_2 is pulsed, nitrate or nitrite is released, and the released NO is reduced to N_2 or NH_3 on the PM surface. On the other hand, for the activated hydrogen spillover limiting process, when H_2 is pulsed, hydrogen is activated on the PM surface and the activated hydrogen moves to the NSM. The importance of activated hydrogen spillover has very recently been the focus of attention [27]. It is considered that the regeneration reaction just after H_2 pulsing is limited by hydrogen spillover because a large amount of hydrogen is supplied for a very short time. The selectivity of the regeneration reaction is determined by the ratio of hydrogen to nitrate (or nitrite). A high ratio favors NH_3 production, and a low ratio favors N_2 and NO. Several factors can determine the ratio, such as the hydrogen activation activity of the PM, concentration of the stored nitrite and nitrate in the NSM, ease of nitrite (or nitrate) reduction, and arrangement of the PM and NSM. Pt and Pd, which have a higher hydrogen activation activity than Rh, exhibited a higher selectivity for NH_3. Potassium and sodium, whose nitrite and nitrate have a lower melting point than the nitrite and nitrate of barium, can be dispersed more readily and widely on an alumina surface. This larger interface area and close distance between the PM and NSM increase the nitrite and nitrate concentration around the PM. The high nitrite and nitrate concentration decreases the selectivity for NH_3. In contrast, for barium, Pt–Ba and Pd–Ba showed a higher selectivity for NH_3.
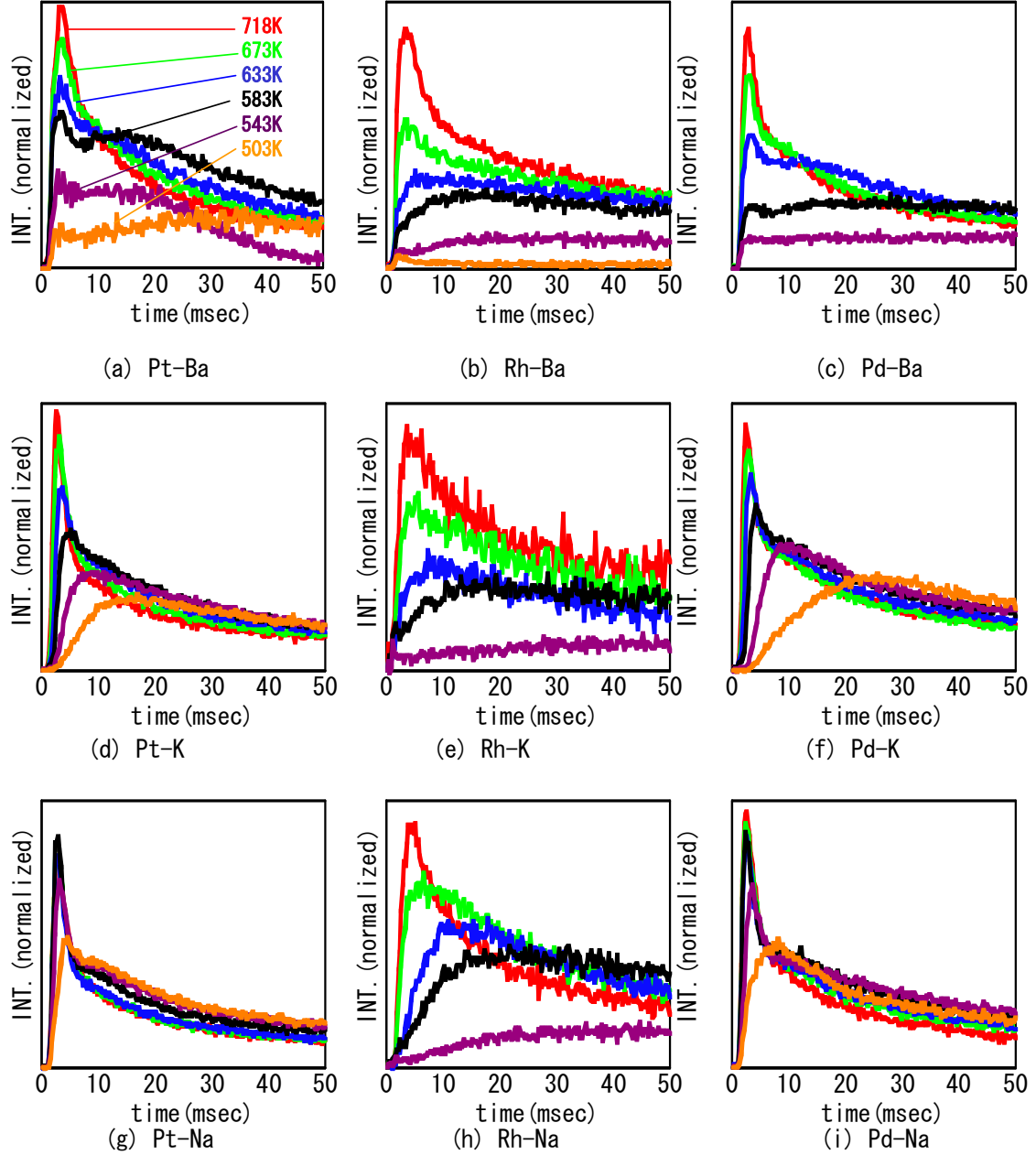
Figure 8. Temperature dependence of the time profiles for $NH_3 + 2N_2 + NO$ production at 583 K. All of the profiles were normalized to their maximum value.

The theoretical curves obtained using this reaction model were fitted to the $[2N_2 + NH_3 + NO]$ profiles using a least squares method.

The two-step reaction model is represented by the following expression [28]:

$$dC/dt = r_1 r_2 / (r_1 - r_2) C_0 (\exp(-r_2 t) - \exp(-r_1 t)), \qquad (7)$$

where t is the time, dC/dt represents the intensity of the $[2N_2 + NH_3 + NO]$, r_1 is the rate constant of the first step, r_2 is the rate constant of the second step, and C_0 is the concentration of stored NOx. All of the data were fitted using this model, and the values of r_1 and r_2 were calculated.

The value of r_1 would be expected to strongly correlate with the release rate of nitrate or nitrite from the NSM in the case of the nitrate (or nitrite) diffusion limiting process. On the other hand, the value of r_1 would be expected to strongly correlate with hydrogen activation on the PM in the case of the activated hydrogen spillover limiting process.

The temperature dependent r_1 curves (Figure 9) clearly show a high release rate of nitrate or nitrite for all of the PM combinations with barium, potassium, and sodium NS materials, and a low release rate in the cases of Rh–K and Rh–Na (Figures 9(c) and (d), respectively). Although the value of r_1 is expected to strongly correlate with the PM and the release rate of nitrate or nitrite (Figure 5), the reason for the low release rates of NOx for these two catalysts is a low catalytic activity to produce activated hydrogen.
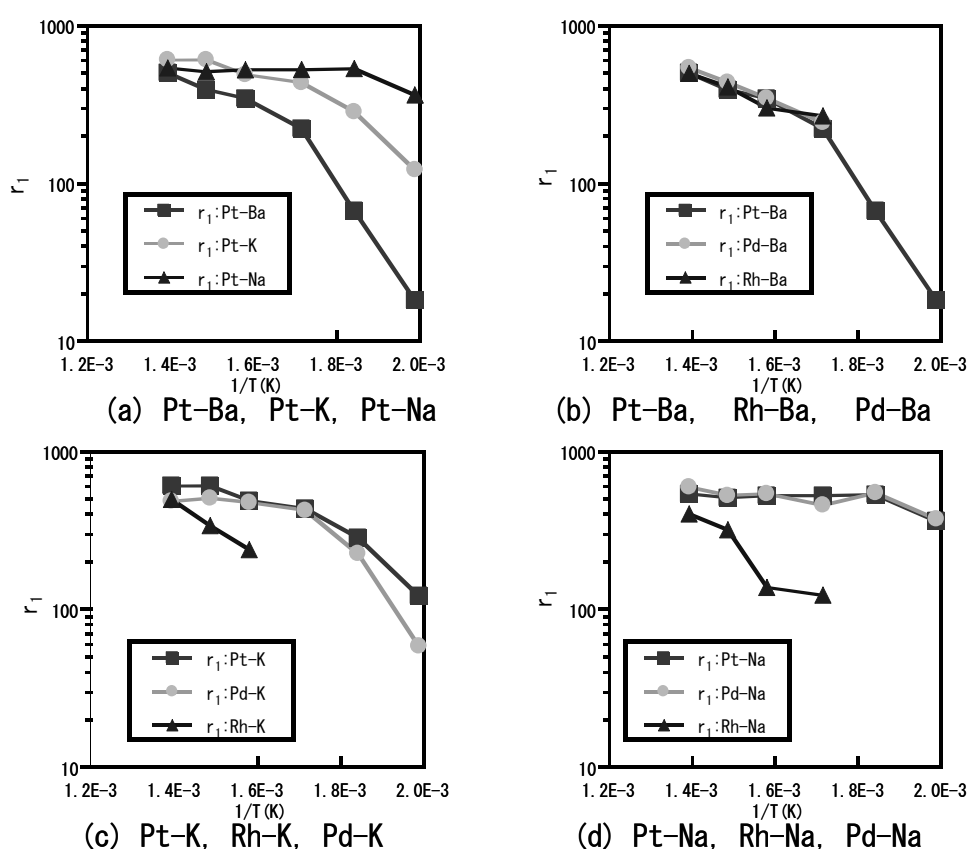
Figure 9. Temperature dependence of r_1 for different NSR catalysts.

It was assumed that r_2 should depend mainly on the PM used for NSR. However, different r_2 values were found for Pt–Ba, Pt–K, and Pt–Na, as shown in Figure 10(a). On the basis of Figure 8(b), it appears that r_2 depends on the NSM. However, different r_2 values were found for the different NSMs, except for potassium. The order of the r_2 curves for the Pt-based catalysts (Figure 10(a)) is similar to that of the r_1 curves shown in Figure 9(a), which implies that r_2 is affected by the nature of both PM and NSM in the catalyst. The catalytic activity of

the PM is strongly influenced by the addition of alkali and alkali earth metals [29,30]. Therefore, the strong interaction between the PM and NSM is the reason why both have a large influence on r_2. It is also thought that r_2 is influenced by both the reaction of the PM in the NOx reduction process and hydrogen spillover.
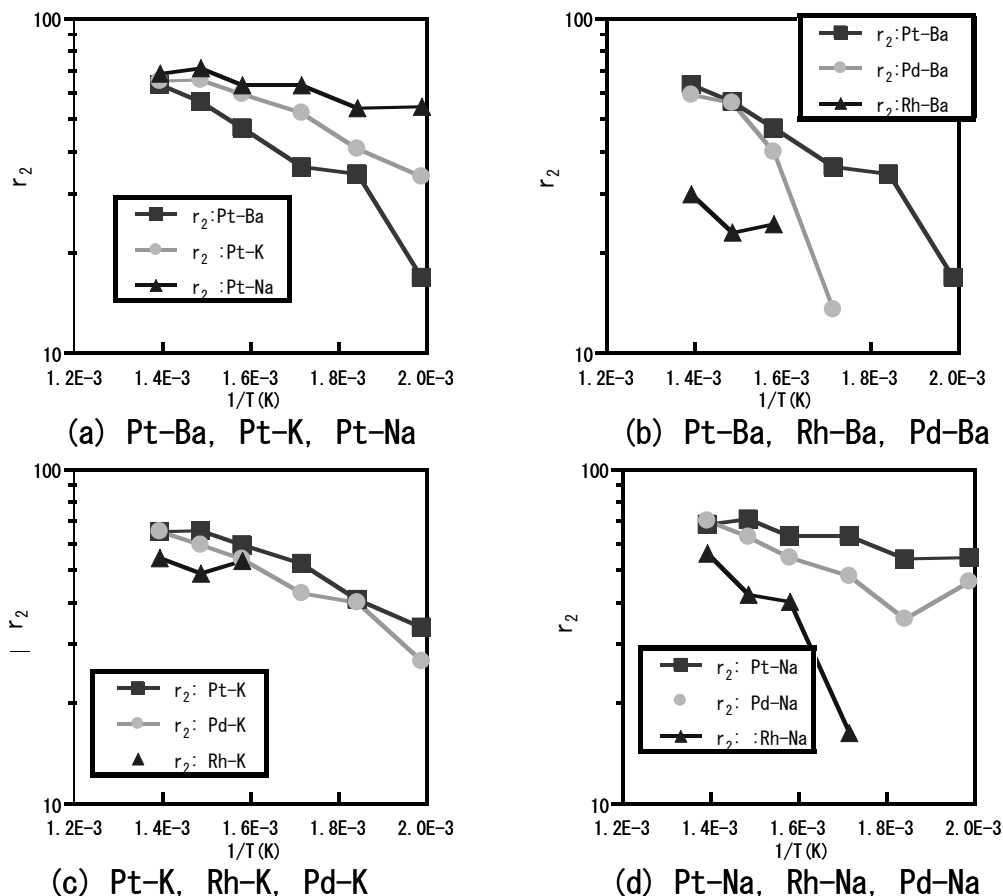
Figure 10. Temperature dependence of r_2 for different NSR catalysts.

The activation energies for r_1 and r_2, which were estimated from Figures 9 and 10, respectively, are shown in Table 2. Some values could not be estimated because of a lack of accuracy. The r_1 curve was estimated in two regions: at high temperature ($r_{1\ High}$) and at low temperature ($r_{1\ Low}$). The value of $r_{1\ High}$ is limited by gas diffusion. Table 2 clearly shows the results and tendencies as described above. For example, the activation energy for $r_{1\ Low}$ was smaller in the order Ba > K > Na, whereas the activation energy for r_2 was smaller in the order Rh > Pt > Pd. Pt/Na/Al$_2$O$_3$ may show high performance with respect to the speed of NOx release because Pt–Na has the lowest activation energy for $r_{1\ Low}$ and r_2.

Table 2 Activation energy of $r_{1\,Low}$, $r_{1\,High}$, and r_2.

	Pt			Rh			Pd		
	r1 Low	r1 High	r2	r1 Low	r1 High	r2	r1 Low	r1 High	r2
Ba	76	20	17	—	21	39	—	17	11
K	39	9	10	60	4	12	30	—	8
Na	22	11	4	22	8	7	33	—	30

5. Conclusions

A comparative study was performed to investigate the effect of PMs (Pt, Pd, and Rh) and NSMs (Ba, K, and Na) on the reduction of stored NOx using transient reaction analysis with submillisecond resolution. The time profiles of the product gases were analyzed for 50 ms after a hydrogen gas pulse. NH_3, N_2, and NO were detected as product gases, and the amount and ratio of these gases differed according to the PM/NSM combination. The reduction rate of stored NOx was in the order Na > K > Ba. Compared with Pt and Pd, Rh produced lesser amounts of NH_3 and larger amounts of NO. The time profile results indicate that the combination of Pt and Na leads to the highest reduction rate of stored NOx.

These differences could be explained with a model that correlates with the spillovers of released NOx from the NSM and the activated hydrogen on the PM. The reduction rate of stored NOx will be affected by both these spillover species. The selectivity for NH_3 will increase with a decrease in the ratio of the rate of NOx spillover to that of activated hydrogen spillover. The lowest activity for hydrogen activation, which was observed for Rh, decreases the ratio and results in low NH_3 selectivity.

References

[1] N. Miyoshi, S. Matsumoto, K. Katoh, T. Tanaka, J. Harada, N. Takahashi, K. Yokota, M. Sugiura, K. Kasahara, SAE Technical Paper 950809, 1995.
[2] S. Matsumoto, Catal. Today 29 (1996) 43–45.
[3] N. Takahashi, K. Yamazaki, H. Sobukawa, H. Shinjoh, Appl. Catal. B 70 (2007) 198–204.
[4] Y. Sakamoto, T. Motohiro, S. Matsunaga, K. Okumura, T. Kayama, K. Yamazaki, T. Tanaka, Y. Kizaki, N. Takahashi, H. Shinjoh, Catal. Today 121, 3-4 (2007) 217–225.
[5] Y. Sakamoto, S. Matsunaga, K. Okumura, T. Kayama, K. Yamazaki, N. Takahashi, T. Tanaka, Y. Kizaki, T. Motohiro, H. Shinjoh, Chem. Eng. Sci. 63 (2008) 5028–5034
[6] J.T. Gleaves, J.R. Ebner, T.C. Kuechler, Catal. Rev.-Sci. Eng. 30 (1988) 49.
[7] J. Pérez-Ramírez, E.V. Kondratenko, Catal. Today 121, 3-4 (2007) 160–169.
[8] T.J. Toops, D.B. Smith, W.P. Partridge, Appl. Catal. B 58 (2005) 245–254.
[9] T.J. Toops, D.B. Smith, W. P. Partridge, Catal. Today 114, 1 (2006) 112–124.

[10] T. Kanazawa, Catal. Today 96 (2004) 171–177.

[11] J.S. Choi, W.P. Partridge, C.S. Daw, Appl. Catal. A 293 (2005) 24–40.

[12] N. Nejar, M.J. Illán-Gómez, Appl. Catal. B 70 (2007) 261–268.

[13] H. Abdulhamid, E. Fridell, M. Skoglundh, Appl. Catal. B 62 (2006) 319–328.

[14] Y. Su, K.S. Kabin, M.P. Harold, M.D. Amiridis, Appl. Catal. B 71 (2007) 207–215.

[15] S. Matsumoto, Y. Ikeda, H. Suzuki, M. Ogai, N. Miyoshi, Appl. Catal. B 25 (2000) 115–124.

[16] H. Hirata, I. Hachisuka, Y. Ikeda, S. Tsuji, S. Matsumoto, Top. Catal. 16/17 (2001) 145–149.

[17] K. Okumura, T. Motohiro, Y. Sakamoto, T. Kayama, Y. Kizaki, H. Shinjoh, Appl. Catal. A, 354 (2009) 111–118.

[18] R.D. Clayton, M.P. Harold, V. Balakotaiah, Appl. Catal. B 81 (2008) 161–181.

[19] P. Forzatti, L. Castoldi, I. Nova, L. Lietti, E. Tronconi, Catal. Today 117 (2006) 316–320.

[20] R.G. Tonkyn, R.S. Disselkamp, C.H.F. Peden, Catal. Today 114 (2006) 94–101.

[21] J. Xu, R. Clayton, V. Balakotaiah, M.P.Harold, Appl.ied Catal. B, 77 (2008) 395.

[22] W.S. Epling, A. Yezerets, N.W. Currier, Appl. Catal. A 74 (2007) 117–129.

[23] V. Medhekar, V. Balakotaiah, M.P. Harold, Catal. Today 121, 3-4 (2007) 226–236.

[24] L. Cumaranatunge, S.S. Mulla, A. Yezerets, N.W. Currier, W.N. Delgass, F.H. Ribeiro, J. Catal. 246, 1 (2007) 29–34.

[25] J.P. Breen, R. Burch, N. Lingaiah, Catal. Lett. 79 (2002) 171–174.

[26] K. Okumura, T. Motohiro, Y. Sakamoto, H. Shinjoh, Surface Science 603 (2009) 2544–-2550.

[27] B.M. Shakya, M.P. Harold, V. Balakotaiah, Catal. Today 184(2012), 27–42.

[28] K. Ohkubo, Y. Igari, S. Tomoda, I. Kusunoki, Surf. Sci. 260 (1992) 44.

[29] M. Konsolakis, N. Macleod, J. Issac, I. V. Yentekakis, R. M. Lambert, J. Catal. 193 (2000) 330–337.

[30] H. Shinjoh, N. Isomura, H. Sobukawa, M. Sugiura, Stud. Surf. Sci. Catal. 116 (1998) 83–91.

Chapter 6.

Adsorption and desorption analysis of NOx and SOx on a Pt/Ba thin film model catalyst

6-1.Intoroduction

Lean-burn engines and diesel engines are widely used to save fuel costs and to decrease vehicle emissions, such as CO_2. However, cleaning up NOx exhaust emissions produced by engines under excess oxygen conditions is difficult. Scientists have been studying NOx elimination systems for many years. Recently, a system using a NOx storage and reduction (NSR) catalyst has been identified and developed as one of the best systems for eliminating NOx under excess oxygen conditions [1,2]. NSR catalysts can eliminate NOx under excess oxygen conditions by storing the NOx in "NOx storage materials," such as barium oxide, sodium oxide, and potassium oxide. The stored NOx is then reduced to N_2 under appropriate conditions involving such reducing gases as H_2, CO, and hydrocarbons. Through repetition of this cycle of NOx storage and reduction, the NSR catalyst purifies the NOx.

NSR catalysts are considered a significant technology for NOx purification and are now widely used. However, NOx stor- age materials have been found to undergo a reaction whereby they also convert SOx to sulfate and thereby lose the ability to store NOx [3]. This so-called "SOx poisoning" is recognized as one of the greatest problems hindering the wider use of NSR catalysts, and ways to overcome the SOx poisoning effect have been widely studied [4,5]. SOx poisoning can be removed using the following reactions, shown here with barium oxide as an example:

$BaSO_4 + H_2 \rightarrow BaO + SO_2 + H_2O$

and

$BaSO_4 + 4H_2 \rightarrow BaO + H_2S + 3H_2O.$

We believe that there are four important reactions besides SOx poisoning and recovery to consider when applying the NSR as an automotive exhaust: NOx adsorption, NOx desorption, SOx adsorption, and SOx desorption. Various studies have investigated these four reactions, leading to the following observations:

• The spillover of NOx between the precious metal and the NOx storage material plays an important role [6–8].
• The desorbed NOx is reduced to N_2 over a precious metal [1,9,10].
• The smaller the crystallite size of the sulfate, the greater the rate of SOx desorption and

recovery of the NO*x* storage material [11–14].

• The inclusion of precious metals accelerates the SO*x* desorption reaction [12–14].

We also need to understand the spillover of NO*x*, SO*x*, and the reducing gas, because the four reactions apparently occur mainly around the precious metal–NO*x* storage material interface. But such studies have not yet been widely performed, with the exception of investigations into the size of the precious metal and the barium oxide particles. Rigorously preparing an adequate model catalyst for the analysis of the spillover and arrange the precious metal and the NO*x* storage material will provide valuable information for developing an NSR catalyst. However, analyzing the geometry has proven difficult, because the commonly used powder catalysts are very complicated and unsuited to investigating the spillover phenomenon. Hence we believed that for this analysis it would be more appropriate to design a simpler model catalyst on a flat substrate using thin film technology.

Our goal in this study is to obtain an image of the NO*x* and SO*x* reactions with reference to the arrangement of the precious metal and the NO*x* adsorption material. In particular, we wish to derive the relationship for the distance between the precious metal and the NO*x* adsorption material for each reaction. These results will be of assistance in developing an NO*x* storage catalyst. Therefore, we performed a study of a simple model catalyst using a flat substrate and a thin film using electron probe microanalysis (EPMA), scanning electron microscopy (SEM), transmission electron microscopy (TEM), electron energy loss spectrometry (EELS), X-ray photoelectron spectroscopy (XPS), and Auger electron spectrometry (AES).

6-2. Experimental

6.2.1. Preparation of model catalysts

Barium oxide was selected as the NO*x* storage material, and platinum was selected as the precious metal. Barium oxide was deposited to a thickness of 200 nm on a Si(110) substrate by a sputtering method using a barium peroxide target. After the barium oxide deposition, a 10 nm thick platinum layer was deposited through a 50 μm square-hole mask composed of Ni with a rectangular shape 0.5 cm in size. The thickness of the barium oxide and the platinum were estimated using a combination of a crystal vibration method and the time taken for deposition. The Si substrate was rotated during the barium oxide deposition for a flat film but was not rotated during the Pt deposition for the shape edge of Pt. Because of the differences in the rotation of the Si substrate, the thickness of the Ba film becomes uniform; however the thickness of each Pt-deposited square island differed depending on location. Fig. 1 illustrates the Pt/BaO*x*/Si model catalyst used for the EPMA, SEM, XPS, and AES analyses
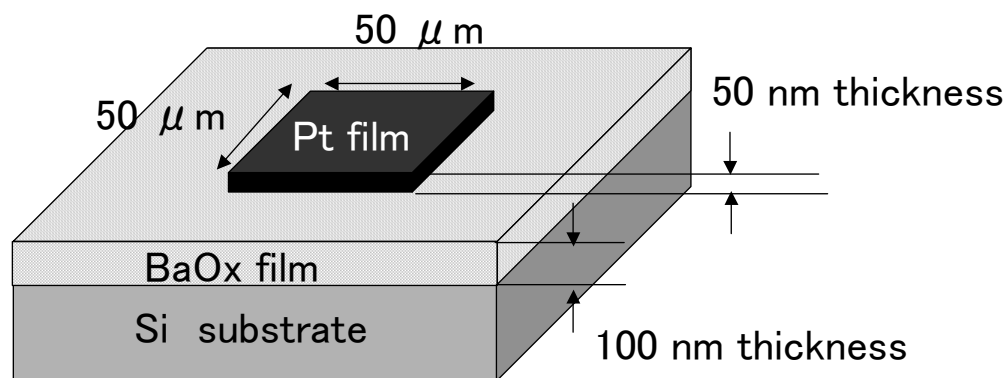
Fig. 1. Pt/BaOx /Si model catalyst for EPMA and AES analysis.

Fig. 2 shows an SEM image of the Pt/BaOx/Si model catalyst in the fresh state before any treatment. The smooth bright area is the site of the Pt deposition, which has a rounded edge. The surface of the area of Ba deposition was not smooth, appearing more like fish scales. The distributions of the Pt and Ba were mapped as an EPMA image, as shown in Fig. 3. The distribution of the Pt on the left side was sharp, whereas the distribution on the right side was broader because the Pt was deposited from the left direction through a shadow mask. The shape of the Pt deposition on the left edge of the shadow mask was clear, but on the right side of the mask the evaporated Pt atoms could encroach into the space between the mask and the Si substrate. The BaOx film was thinner around the edge of the Pt than in the other areas, due to the Pt deposition. The surface distribution of Pt and Ba was mapped by AES (Fig. 4), which is considered an appropriate surface analysis technique. The surface distribution of the Pt was sharper than the bulk distribution measured by EPMA, and Ba was detected in all areas except those in which Pt deposition occurred. Because it is recognized that the model catalyst obtained thusly is almost the same as that shown in Fig. 1 in the micrometer range, we decided to perform further analysis of the NSR catalyst reaction.

AES was originally considered an appropriate method for measuring the distribution of Pt, Ba, N, and S because its sensitivity and spatial resolution are superior to that of EPMA. But in this instance, we had to revise our ideas about using AES as a method for analyzing the distribution of these elements. The electron beam used as the probe in AES caused some blackening of the areas with low distributions of Ba, except for the areas in which Pt was deposited. It is concluded that in our experiment AES can be used for the Pt area analysis but not for the barium area, because the electron beam is believed to damage and contaminate the barium oxide. The electron beam of AES may decompose the barium compound of nitrate, nitrite and sulfides; therefore, EPMA is used as the main analysis technique.
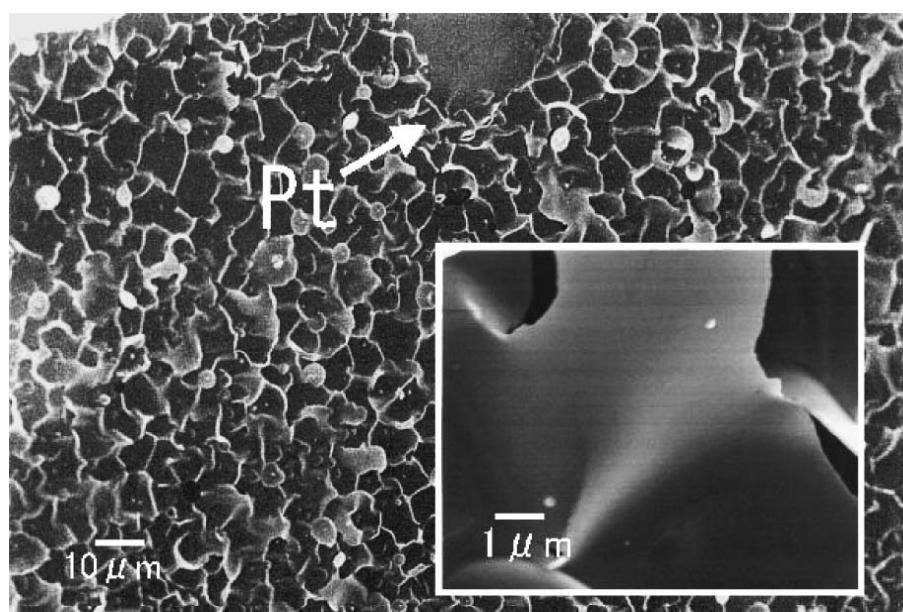
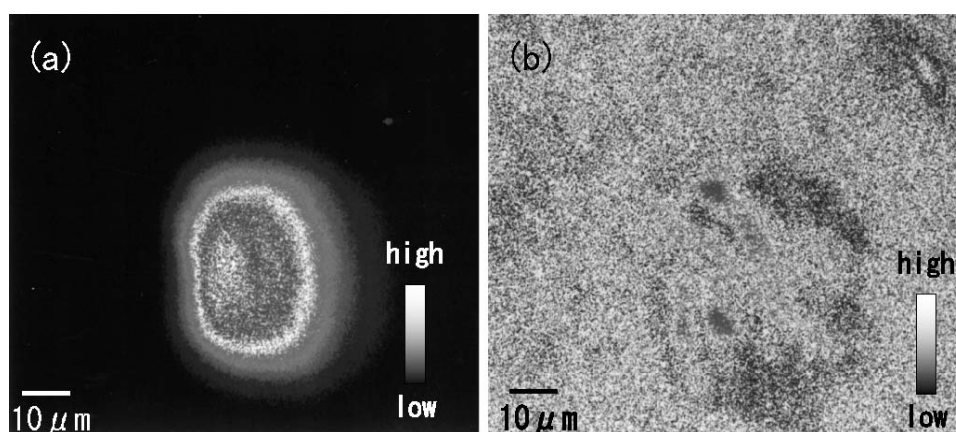Fig. 2. SEM image of Pt/BaOx /Si model catalyst.

Fig. 3. EPMA image of Pt/BaOx /Si model catalyst: (a) Pt and (b) Ba distribution.
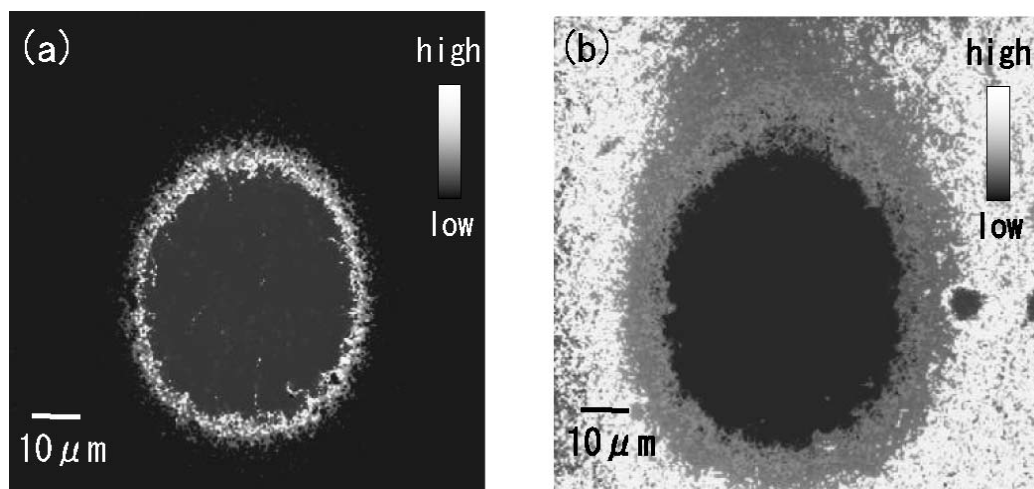
Fig. 4. AES image of Pt/BaOx/Si model catalyst: (a) Pt and (b) Ba distribution.

6.2.2. Gas treatment and characterization of model catalysts

The model catalyst was found to be adequate for our analysis; therefore, we treated the model catalyst with four sets of conditions to simulate the four reactions that are important in the production of a practical NSR catalyst: NOx adsorption, NOx desorption, SOx adsorption, and SOx desorption.

The NOx treatment used to simulate the NOx adsorption was as follows. The Pt/BaOx/Si model catalyst was heated in an NOx atmosphere at 476, 573, and 673 K for 1 h to store NOx in the model catalyst. A reduction process under H$_2$ was then carried out to simulate NOx desorption, as follows. The Pt/BaOx/Si model catalyst that had been heated in NOx was further heated at 523 and 623 K in an H$_2$ atmosphere for 1 h to release the stored NOx from the model catalyst. The details of each of these atmospheres are summarized in Table 1. The surface shapes of these model catalysts were observed using SEM. The bulk distributions of Pt and Ba around each sample were measured using EPMA.

The simulated SOx treatment was as follows. The Pt/BaOx/ Si model catalyst was heated in a SOx atmosphere at 573, 673, 773, and 873 K for 1 h to adsorb SOx onto the model catalyst. After the SOx treatment, the Pt/BaOx/Si model catalyst was heated in an H$_2$ atmosphere at 873, 923, and 973 K for 30 min to simulate the SOx desorption.

After the above treatments, each sample was analyzed using a two-dimensional analysis by EPMA and AES. Each sample diffusions into the BaOx thin film. This depth information was obtained to compare the molar ratios of N/Ba and S/Ba obtained by EPMA and XPS, because EPMA measures to a micrometer depth, whereas XPS measures to a depth of a few nanometers. The molar ratio of N/Ba indicates the ratio of "NOx storage barium

66

oxides" to "free barium oxides" (those not used to store NOx). The same approach was adapted to determine SOx adsorption and release by measuring the molar ratio of S/Ba.

Oxidizing conditions for a few minutes and reducing conditions for a few seconds were alternately repeated to eliminate NOx in exhaust gas simulating realistic engine operation. The treatment duration of our experiment, one hour, seems to be longer than that of realistic engine operation. We suppose that the long duration of our experiment is suitable for a duration test; an automotive catalyst is usually used for about 10,000 h. Analysis of the shorter duration is interesting and is affected more by the surface of barium nitrate [15] and sulfate [16]. The shorter duration time decreases the amounts of nitrate and sulfide, making it more difficult to measure the distribution of N and S. Other methods for surface analysis may be needed.

Regarding gas conditions, practical exhaust gases involve CO_2 and H_2O. The kinds of gas have some affect on NSR [17–19] and merit investigation.We consider the study of treatment duration and gas conditions subjects of future investigation using this model catalyst.

6-3. Results

6.3.1. NOx adsorption and reduction of the Pt/BaOx /Si model catalyst

An appropriate model catalyst was obtained, and the NOx adsorption and reduction over the Pt/BaOx/Si model catalyst were investigated. Fig. 5 shows an SEM image of the model   catalyst after the NOx treatment. The surface of the Ba became smoother and the contrast with the Pt area became weaker than in the fresh state before treatment in the image with the 10-μm scale bar in Fig. 5. Small particle sizes of Ba became visible at higher magnification as shown in the image with the 1-μm scale bar in Fig. 5. Similar picture of small particles on flat large planes after the NOx treatment is also reported as small $Ba(NO_3)_2$ particles on stable flat $Ba(NO_3)_2$ particles in NSR catalyst using BaO/Al2O3 catalyst [20].
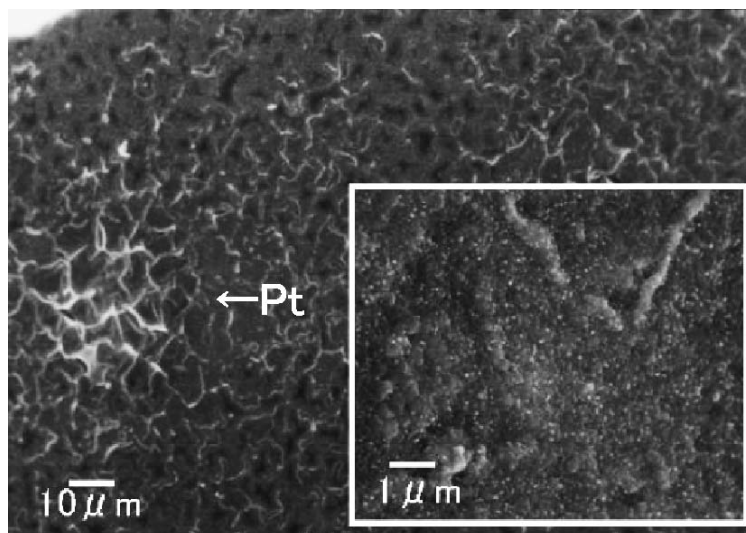
Fig. 5. SEM image of Pt/BaOx /Si model catalysis
after 673 K NOx treatment.

The distributions of Pt, Ba, and N were mapped as an EPMA image, as shown in Fig. 6. The white circle indicates an area in which Pt was detected. N was detected over the entire sample, and the concentration of N seemed to be higher around the edge of the Pt than in the other regions. The edge of the Pt area became blurred in comparison with its appearance before the NOx treatment.

Samples of the Pt/BaOx/Si model catalyst that had been treated by the NOx treatment described above were reduced under H_2 at either 523 or 623 K. The results of these processes are shown in Figs. 7 and 8. The NOx stored in the model catalyst was reduced in and around the Pt area. The width of the reduced material around the Pt was a few micrometers in both cases. When the H_2 treatment temperature was increased to 623 K (Fig. 8), the distribution of Ba became nonuniform.

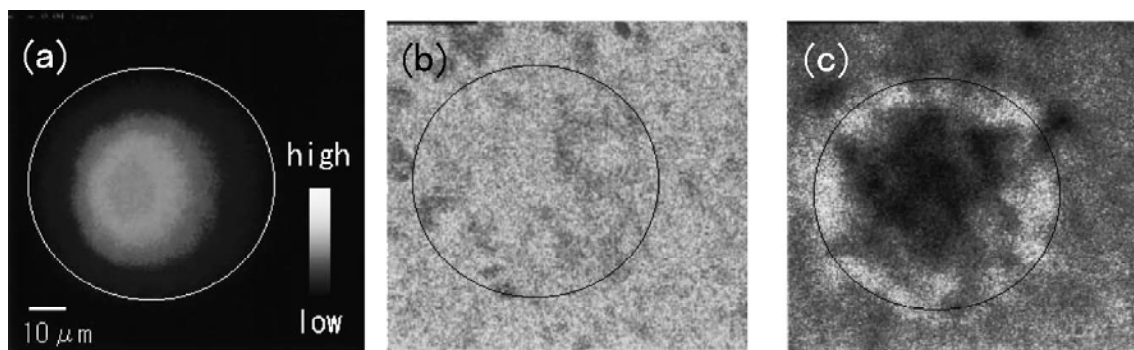Fig. 6. EPMA image of Pt/BaOx/Si model catalyst after 673 K NOx treatment: (a) Pt, (b) Ba and (c) N distribution.
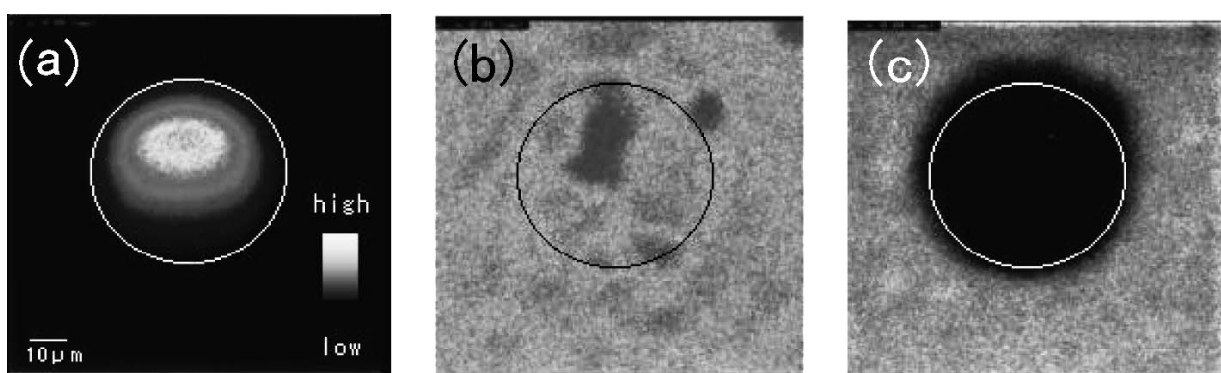

Fig. 7. EPMA image of Pt/BaOx/Si model catalyst after 673 K NOx treatment followed by 523 K H2 treatment: (a) Pt, (b) Ba and (c) N distribution.
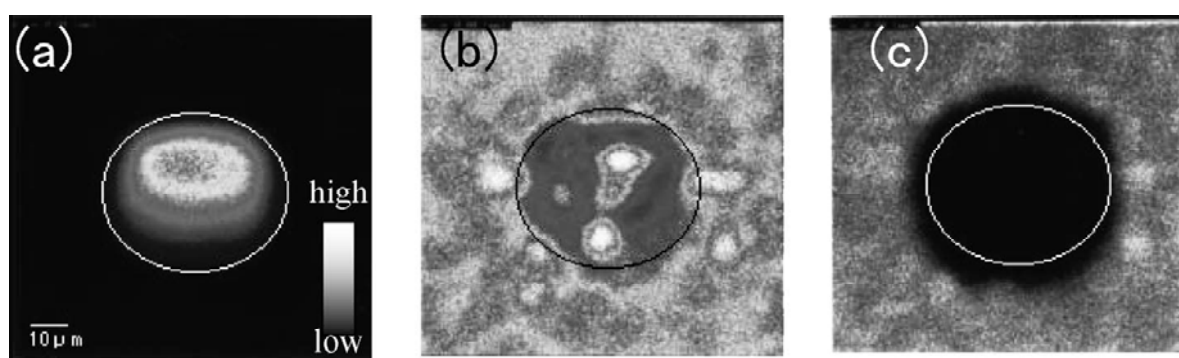

Fig. 8. EPMA image of Pt/BaOx/Si model catalysis after NOx treatment followed by 623 K H2 treatment: (a) Pt, (b) Ba and (c) N distribution.

6.3.2. SOx adsorption and reduction above the Pt/BaOx /Si model catalyst

The SOx adsorption and reduction were also investigated for the Pt/BaOx/Si model catalyst using the same technique used for the NOx adsorption and reduction analysis. Fig. 9 shows an SEM image of the Pt/BaOx/Si model catalyst after the SOx treatment at 673 K. The area around the Pt was blackened, and submicrometer-size particles appeared on the surface of the barium area, as shown in the image with the 1-μm scale bar in Fig. 5. The distribution of the S was mapped as the EPMA image shown in Fig. 10. S was detected all over the sample. We attempted to measure the distribution of S on the Pt using AES, because S may strongly adsorb on the surface of Pt [21,22]. But because no S was detected on the Pt surface, as shown in Fig. 11, we concluded that the S was adsorbed mainly on the barium oxide. Pt played an important role in oxidizing the NO to NO_2 in the NOx adsorption, but did not take part in the SOx adsorption. This finding deactivation of alumina-supported Pt catalysts that found that under lean conditions, SO_2 is oxidized to SO_3 independent of Pt [23].   The Pt/BaOx/Si model catalyst that had undergone the SOx treatment was reduced under H_2 at 873, 923, and 973 K. All of the EPMA results concerning the distributions of Pt, Ba, and S are shown in Fig. 12. The SOx in the model catalyst was further reduced at increasing temperatures. The width of the area of the reduced S around the Pt was below the spatial resolution of the EPMA technique, which measures on a micrometer scale. A detailed analysis of the width of the SOx desorption around the Pt was investigated using a nanoscale TEM analysis of the BaOx/Pt/Al_2O_3 model catalyst.
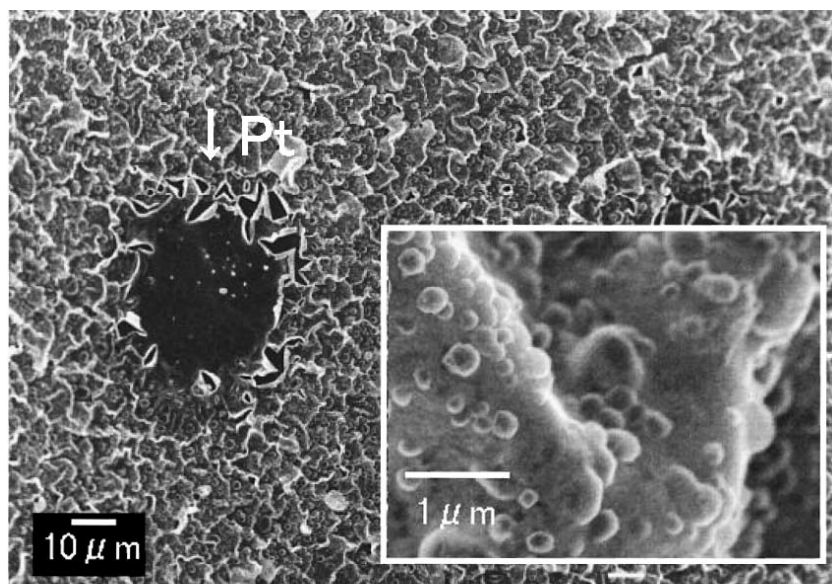
Fig. 9. SEM image of Pt/BaOx /Si model catalyst after 673 K SOx treatment
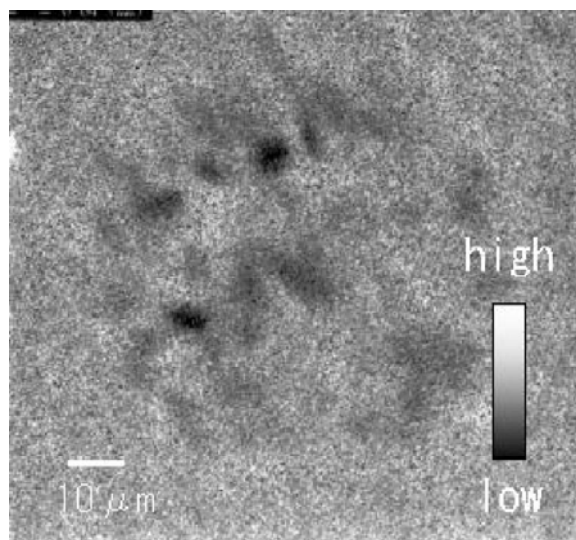
Fig. 10. S distribution measured by EPMA of Pt/BaOx /Si model catalysis after 673 K SOx treatment.
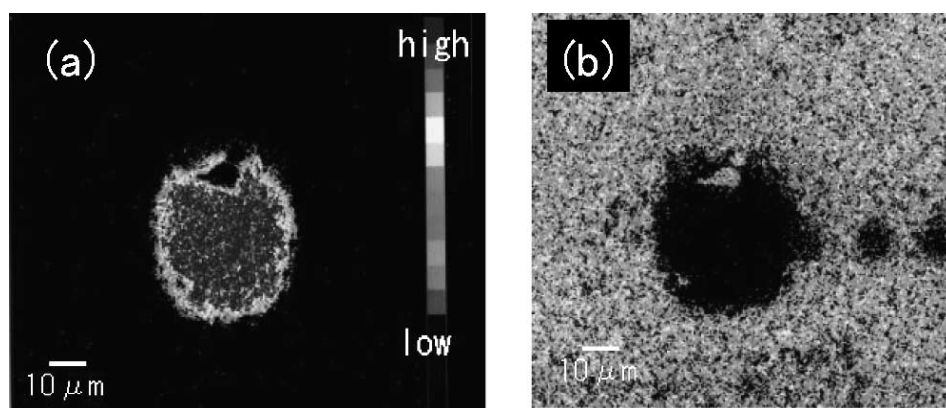
Fig. 11. AES image of Pt/BaOx /Si model catalyst after 673 K SOx treatment:(a) Pt and (b) S distribution.
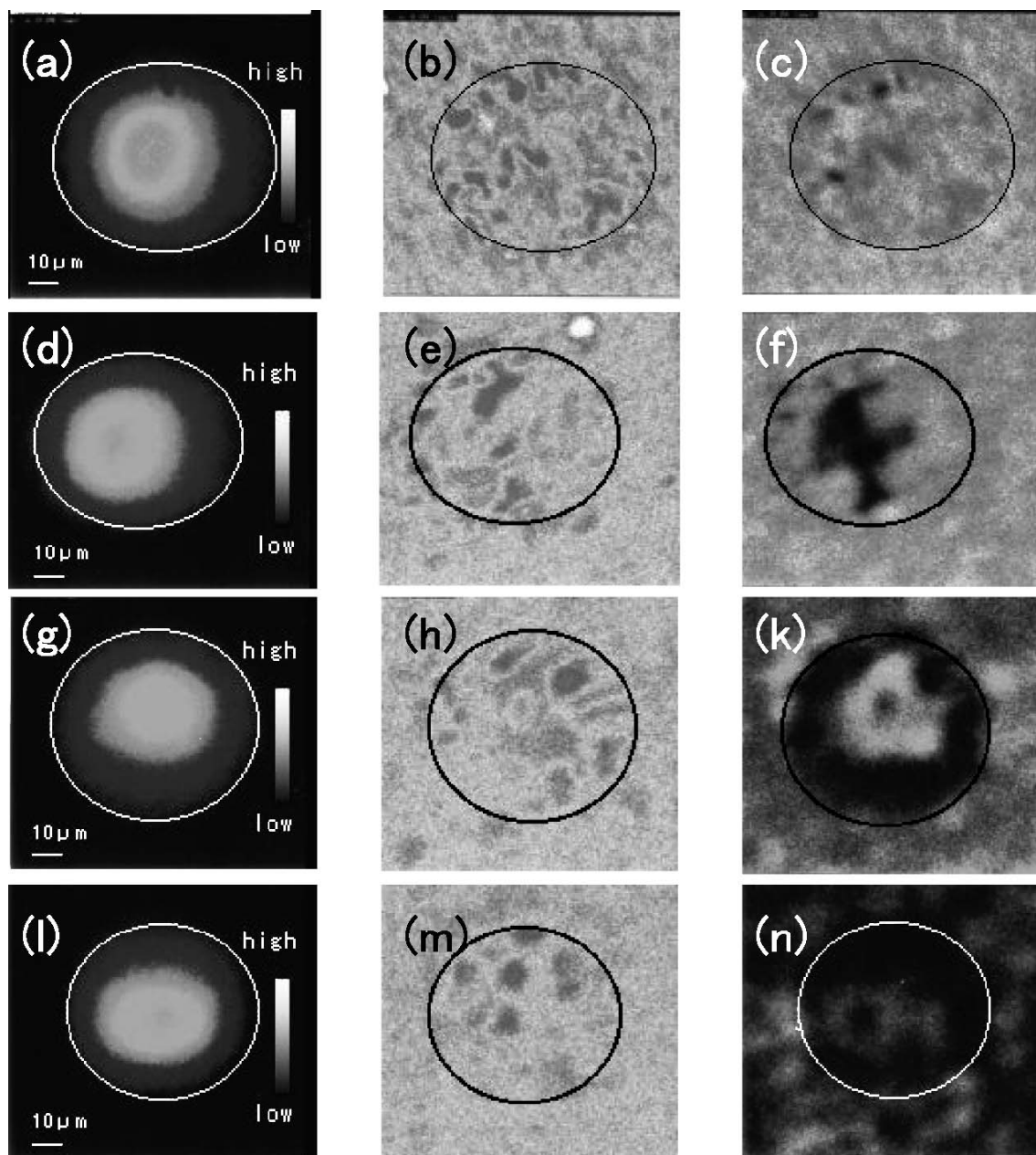
Fig. 12. EPMA image of Pt/BaOx/Si model catalyst; after 673 K SOx treatment, (a) Pt, (b) Ba and (c) S distribution; after the SOx treatment followed by 873 K H$_2$ treatment, (d) Pt, (e) Ba and (f) S distribution; after 923 K H$_2$ treatment, (g) Pt, (h) Ba and (k) S distribution; after 973 K H$_2$ treatment, (l) Pt, (m) Ba and (n) S distribution.

6.3.3. SOx reduction over a BaOx/Pt/Al2O3 model catalyst on an Au mesh

The width of the SOx reduction area of Ba(SO$_4$)$_2$ around the Pt could not be clarified by the EPMA analysis, because it was considered below the micrometer scale based on the resolution of the EPMA instrument. Therefore, the width of the SOx reduction area around the Pt was investigated by TEM analysis with nanometer resolution.

Fig. 13 shows the BaOx/Pt/Al$_2$O$_3$ model catalyst used for the TEM analysis. The model catalyst was produced as follows. An 80 nm film of Al$_2$O$_3$ was deposited by a sputtering method onto a NaCl crystal. The Al$_2$O$_3$ film was peeled off in water, from which the floating Al$_2$O$_3$ film was skimmed off using an Au mesh. This mesh was then treated in air at 873 K for 1 h, after which a 0.2 nm Pt layer was also deposited on the mesh by a sputtering method and treated in air at 873 K for 1 h to create Pt particles. A 1.8 nm layer of barium oxide was then deposited on this Pt/Al$_2$O$_3$ and treated in air at 873 K for 1 h. The Ba/Pt/Al$_2$O$_3$ model catalyst was analyzed by TEM with EELS capability (HF-2200, Hitachi High Technologies) after SOx treatment and subsequent H$_2$ treatment. The SOx treatment was performed at 673 K in SOx atmosphere (as indicated in Table 1) for 30 min, and the subsequent H$_2$ treatment was performed at 873 K in H$_2$ atmosphere for 30 min.

Fig. 14 shows a TEM image and EELS images of the BaOx/Pt/Al$_2$O$_3$ model catalyst after SOx treatment at 673 K. Ba was uniformly deposited, and SOx was adsorbed on the BaOx . Fig. 15 shows a TEM image and EELS images of the BaOx/Pt/Al$_2$O$_3$ model catalyst after SOx treatment at 673 K followed by an H$_2$ treatment at 873 K. Because the area where the Pt existed was almost the same as the area of decreased S (by TEM analysis with nanometer resolution), the SOx desorption was confirmed as occurring easily in a confined area of less than a few nanometers around the Pt.
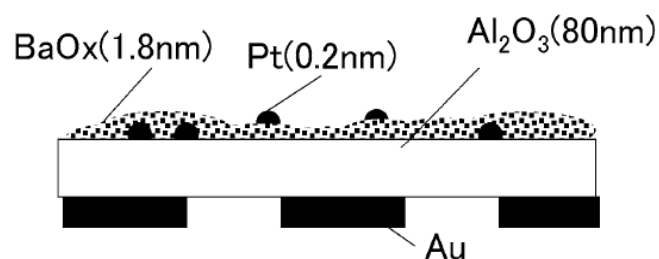

Fig. 13. BaOx /Pt/Al$_2$O$_3$ model catalyst for TEM analysis.
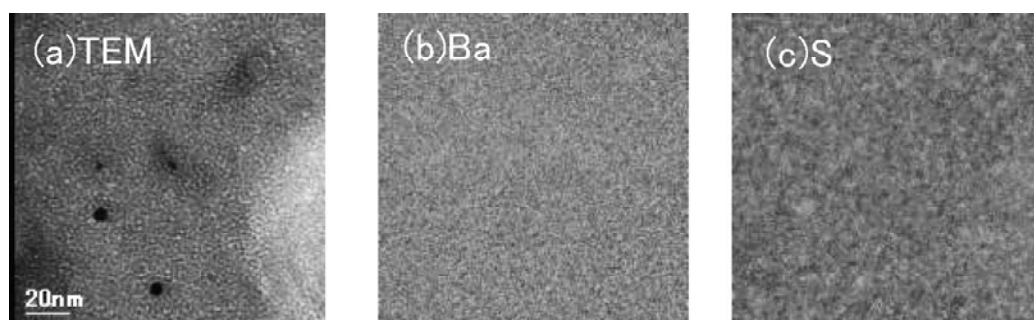
Fig. 14. TEM image and EELS image of BaOx /Pt/Al$_2$O$_3$ model catalyst; after 673 K SOx treatment, (a) TEM, (b) Ba and (c) S distribution; the dark area indicates low concentration.
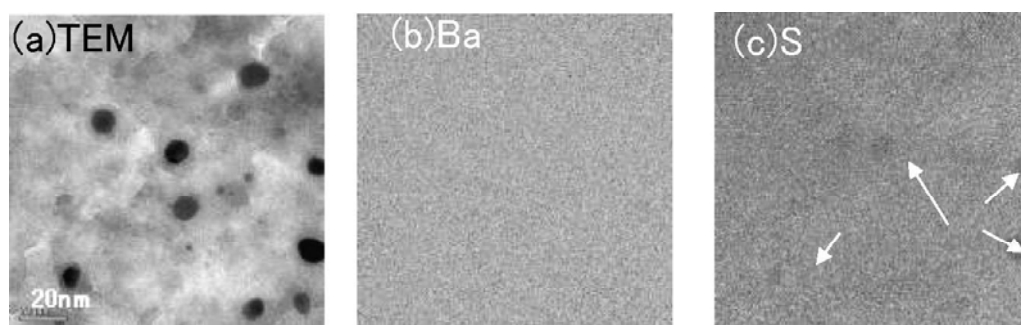
Fig. 15. TEM image and EELS image of BaOx /Pt/Al$_2$O$_3$ model catalyst; after 873 K H$_2$ treatment followed by 673 K SOx treatment: (a) TEM, (b) Ba and (c) S distribution, the dark area indicates low concentration..

6.3.4. Diffusion of NOx and SOx into the BaOx thin film

Fig. 16 shows a comparison between the bulk and the surface distributions of N and S (measured by EPMA and XPS) in the Pt/BaOx/Si model catalyst after the NOx and SOx treatments. The intensities of the N and S signals were normalized to commercially available Ba(NO$_3$)$_2$ and BaSO4 (Kojundo Chemical Laboratory). Surface N/Ba and S/Ba ratio were always considered higher than the bulk ratios, because both NOx and SOx gas were contacted with the Ba oxide surface. The surface distribution of N was almost proportional to the bulk distribution, as shown in Fig. 16a; however, the surface distribution of S was not proportional at low temperature (below 773 K). The bulk distribution of S became proportional to the surface distribution at high temperature (873 K). This fact indicated that NOx was uniformly adsorbed into the BaOx , whereas SOx was adsorbed from the surface of the BaOx at low temperature.

74
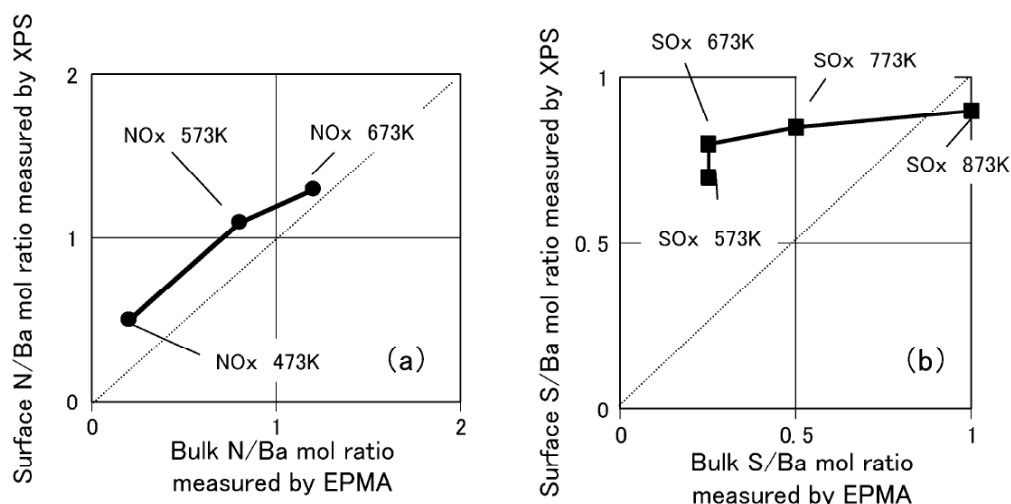
Fig. 16. Comparison between bulk and surface distribution of N and S measured by EPMA and XPS of Pt/BaOx/Si model catalyst.

6-4. Discussion

The differences among four main reactions—NOx adsorption, NOx desorption, SOx adsorption, and SOx desorption— must be considered when designing a practical NSR catalyst for automotive exhaust. NOx adsorption, termed "NOx storage" in this context, occurs as follows. NO is oxidized to NO$_2$, and the NO$_2$ reacts with barium oxides or barium carbonate to form barium nitrate. This mechanism is adapted for the SOx adsorption. SOx adsorption, termed "SOx poisoning" in this context, reduces NOx storage capability.

The strongest adsorption sites for NOx and SOx are considered to be those around the Pt. NOx seemed to be adsorbed more readily around Pt than at the other sites (Fig. 7c); however, SOx was adsorbed on the BaOx regardless of the presence or absence of Pt.

The decomposition of Ba(NO$_3$)$_2$ was suggested to occur first within a few micrometers around the Pt (Fig. 8). This image, shown in Fig. 17, may provide insight into why only 20% of the Ba compound seems to work as an NOx storage material immediately after the catalysts are produced [24]. The amount of NOx storage depends on the number and size of the precious metal particles. When the amount of precious metal increases, the Ba(NO$_3$)$_2$ decomposition area increases, and when the particle size increases, the NOx reduction area decreases. It has also been recently suggested that a "special area" of NOx decomposition exists around the Pt particles [6,14,25].

75

Fig. 17. View of reduction of Ba(NO$_3$)$_2$ around Pt.

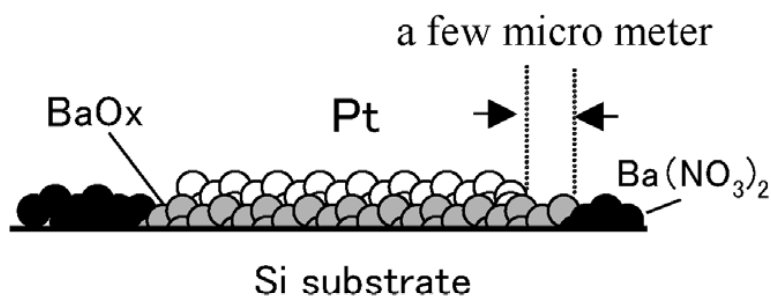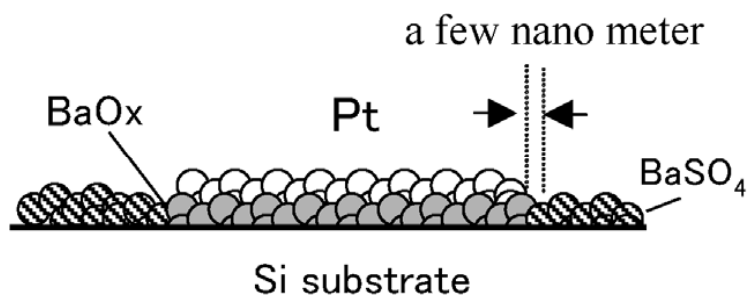Fig. 18. View of reduction of BaSO$_4$ around Pt.

It has been suggested that the reduction of BaSO4 occurs within a few nanometers around the Pt as opposed to within a few micrometers of the Ba(NO$_3$)$_2$ decomposition. Two types of barium sulfates have been identified, bulk and surface, and platinum does not influence the reduction of bulk barium sulfates [17,26]. The difficulty eliminating S from BaSO4 is reportedly caused by the formation of BaS on reducing condition, which is stable even at high temperature (1073 K) [11]. The reduction scheme for the BaSO$_4$ could be as illustrated in Fig. 18. The amount of Ba compounds that act as NOx storage materials decreases under normal engine operation, including the SOx regeneration process. Barium compounds within a few nanometers around the Pt can ultimately work as NOx storage materials. The differences in the decomposition processes of Ba(NO$_3$)$_2$ and BaSO4 can be attributed to a spillover of hydrogen atoms. The currently accepted hydrogen spillover mechanism involves the migration of hydrogen atoms from a metal, which enables the dissociation of hydrogen molecules toward the acceptor material [27,28]. In particular, the decomposition of small BaSO4 crystallites can be affected by hydrogen spillover [26]. The active hydrogen atoms are created on the Pt site and the spillover hydrogen atoms move toward the surface of the Ba(NO$_3$)$_2$ or BaSO4. This model is essentially the same as that for H$_2$ on Pt/TiO$_2$ [29,30]. The difference in area between these two kinds of reduction may be caused by the mobility of the hydrogen atoms and the reactivity of the hydrogen atoms with the Ba(NO$_3$)$_2$ or the BaSO4. Alternatively, the differences may be due to the differences in NO$_2$ and SO$_3$ spillover, because it has been reported that NO migration may originate from the decomposition of barium nitrate to the noble metal sites via spillover [7]. For an NOx storage catalyst to maintain a high activity as an NSR catalyst, the interface area between the

Pt and the barium compounds must remain high.

Finally, we discuss in more detail the bulk and surface distributions of N/Ba and S/Ba ratio in the Pt/BaOx/Si model catalyst after NOx and SOx treatments, as shown in Fig. 16. It is well known that in the presence of SO$_2$, bulk sulfate is readily formed in these systems [14–16,21,27]. However, under normal operating conditions of oscillating lean/rich cycles, there is little evidence that bulk nitrates are formed [20,31]. At first glance, these findings seem to contradict those shown in Fig. 16; however, these differences can be reconciled by distinguishing between the surface of particles and the surface (top) of film. The film of barium oxide in the model catalyst is composed of small barium oxide particles, and the findings in the literature are adapted to these small particles. The small particles can readily become bulk sulfate in sequence from the surface of the film in the SOx . It is difficult for SOx to reach the bottom of film. On the other hand, only the surface of each particle can form nitrate. The BaOx film gradually becomes barium nitrate from the top to the bottom at low temperature.

6-5. Conclusion

Thin film was designed as a NOx storage catalyst and investigated with respect to NOx and SOx adsorption/desorption using EPMA, AES, XPS, and EELS. NOx and SOx were adsorbed all over the model catalyst; however, NOx desorption occurred preferentially in an area a few micrometers around the platinum and was suppressed at all other sites, whereas SOx desorption occurred preferentially in an area a few nanometers wide around the platinum.

References

[1] N. Takahashi, H. Shinjoh, T. Iijima, T. Suzuki, K. Yamazaki, K. Yokota, H. Suzuki, N.Miyoshi, S. Matsumoto, T. Tanizawa, T. Tanaka, S. Tateishi, K. Kasahara, Catal. Today 27 (1996) 63.

[2] W.S. Epling, L.E. Campbell, A. Yezerets, N.W. Currier, J.E. Parks, Catal. Rev. Sci.-Eng. 46 (2) (2004) 163.

[3] P. Engström, A. Amberntsson, A. Skoglundh, E. Fridell, G. Smedler, Appl. Catal. B 22 (1999) L241.

[4] S. Matsumoto, Catal. Today 90 (2004) 183.

[5] K. Yamazaki, T. Suzuki, N. Takahashi, K. Yokota, M. Sugiura, Appl. Catal. B 30 (2001) 459.

[6] L. Olsson, E. Fridell, M. Skoglundh, B. Andersson, Catal. Today 73 (2002) 263.

[7] S. Salasc, M. Skoglundh, E. Fridell, Appl. Catal. B 36 (2002) 145.

[8] P.T. Fanson, M.R. Horton,W.N. Delgass, J. Lauterbach, Appl. Catal. B 46 (2003) 393.

[9] R. Burch, J.A. Sullivan, J. Catal. 182 (1999) 489.

[10] R. Burch, A.A. Shestov, J.A. Sullivan, J. Catal. 182 (1999) 497.

[11] S. Poulston, R.R. Rajaram, Catal. Today 81 (2003) 603.

[12] A. Amberntsson, M. Skoglundh, M. Jonsson, E. Fridell, Catal. Today 73 (2002) 279.

[13] S. Matsumoto, Y. Ikeda, H. Suzuki, M. Ogai, N. Miyoshi, Appl. Catal. B 25 (2000) 115.

[14] Z. Liu, J.A. Anderson, J. Catal. 224 (2004) 18.

[15] Y. Su, M.D. Amiridis, Catal. Today 96 (2004) 31.

[16] Z. Liu, J.A. Anderson, J. Catal. 228 (2004) 243.

[17] S. Elbouazzaoui, E.C. Corbos, X. Courtois, P. Marecot, D. Duprez, Appl. Catal. B 61 (2005) 236.

[18] W.S. Epling, J.E. Parks, G.C. Campbell, A. Yezerets, N.W. Currier, L.E. Campbell, Catal. Today 96 (2004) 21.

[19] S. Balcon, C. Potvin, L. Salin, J.F. Tempère, G. Djéga-Mariadassou, Catal. Lett. 60 (1999) 39.

[20] J. Szanyi, J.H. Kwak, J. Hanson, C. Wang, T. Szailer, C.H.F. Peden, J. Phys. Chem. B 109 (2005) 7339.

[21] Ch. Sedlmair, K. Seshan, A. Jentys, J.A. Lercher, Catal. Today 75 (2002)413.

[22] A. Amberntsson, M. Skoglundh, S. Ljungström, E. Fridell, J. Catal. 217(2003) 253.

[23] V. Meeyoo, D.L. Trimm, N.W. Cant, Appl. Catal. B 19 (1998) L101.

[24] I. Nova, L. Castoldi, L. Lietti, E. Tronconi, P. Forzatti, Catal. Today 75(2002) 431.

[25] D. James, E. Fourre, M. Ishii, M. Bowker, Appl. Catal. B 45 (2003) 147.

[26] X. Wei, X. Liu, M. Deeba, Appl. Catal. B 58 (2005) 41.

[27] M. Boudart, Adv. Catal. 20 (1969) 153.

[28] W.C. Conner Jr., G.M. Pajonk, S.J. Teichner, Adv. Catal. 34 (1986) 1.

[29] D.D. Beck, J.M. White, J. Phys. Chem. 88 (1984) 174.

[30] D.D. Beck, J.M. White, J. Phys. Chem. 88 (1984) 2764.

[31] P. Broqvist, H. Grönbeck, E. Fridell, I. Panas, Catal. Today 96 (2004) 71.

Chapter 7

NOx decomposition on PtAu electrode of amperometric NOx sensor

7-1.Intoroduction

An amperometric NOx sensor based on a zirconia electrochemical cell can be used to measure the pumping current that is produced as the oxide ions associated with the electrochemical reduction of NOx gas. In order to detect NOx gas selectively in the presence of excess O_2 and H_2O, multi-electrode type sensors, in which more than two zirconia cells are connected in series, have been proposed [1–6]. In these types of sensor, the oxygen concentration in the gas being tested is preferentially lowered in the first cell, before the concentration of the NOx is detected in a subsequent cell. Either gold or a platinum–gold alloy is typically employed as the working electrode in the first cell, because it is well known that a gold-containing electrode reduces the NO decomposition and enables the preferential oxygen pumping at the low applied voltage below 0.4V [2,4,6]. However, the mechanism for the preferential pumping of oxygen on a Pt–Au alloy electrode has not yet been clarified. It is important for the construction of amperometric
NOx sensors with a high selectivity for NOx that we elucidate the mechanism for the preferential pumping of O_2 on Pt–Au electrodes, as well as having an understanding of the mechanism for the electrochemical reduction of NO on various other types of electrodes.

The mechanism for the electrochemical reduction of NOx on various noble metal electrodes has mainly been studied up to now with respect to the electro catalytic removal of NOx [7–9]. Since the aim of those studies was to achieve the preferential decomposition of NO in the presence of excess O_2, the mechanism for the preferential pumping of oxygen was not emphasized. Hibino et al. correlated the capability for the
NO decomposition with that for the oxygen pumping by using a solid electrolyte spectroscopy (SEP) method. However, the reasons why the decomposition of NO was reduced on the Au electrode were not discussed in detail [8]. In addition, their study utilized a conventional electrochemical method to investigate the mechanism, which did not have the ability to obtain information about the transient phenomena that occur on the electrode. We consider that it is important to observe these transient phenomena in the electrochemical decomposition of NO to fully understand the process.

Motohiro et al. developed a dynamic vacuum system for the transient analysis of the surface catalytic reactions. This is equipped with four pulsed valves and a time-of-flight mass spectrometer (TOF-MS) [10,11]. It was found that time transient information relating

to the catalytic surface reactions

on planar samples could be obtained with an adequate   signal intensity by using this system. We modified this   system with reference to the TAP (temporal analysis of   products) reactor [12] for the transient analysis of the   electro catalytic reaction in electrochemical cells at temperatures

up to 973 K, so that the reaction products on the   electrodes and the cell current could be measured simultaneously   on a millisecond timescale. This paper deals with   the mechanism for the electrochemical reduction of NO on   Pt and Pt–Au alloy electrodes using our new approach. It   will be shown that our method provides significant information   on the mechanisms for the electrochemical reduction of   NO and for the preferential oxygen pumping on the Pt–Au   alloy electrode in an amperometric NOx sensor.

7-2.Experimental

A sample of zirconia cell (length: 30 mm, width: 3.2 mm, thickness: 0.4 mm) was fabricated by firing a YSZ (YSZ, 8 mol% Y2O3 doped ZrO_2) green sheet at 1753 K for 1 h in air, after thick film electrodes had been printed on both sides of the green sheet. A Pt–10 wt.% YSZ paste and a Pt–1 wt.% Au–10 wt.% YSZ paste (customordered from Tokuriki Chemical Co. Ltd.) were used for printing the thick film electrodes. The YSZ powder was mixed into the noble metal paste in order to improve current stabilities. In the cell sample, the same paste was utilized for the anode and the cathode. The thickness of the electrode was approximate 10 mm regardless of   the electrode species. No differences were observed by a scanning electron microscope in the microstructure and the thickness between a Pt electrode and a Pt–Au electrode. Pt wires were attached to both the anode and the cathode respectively to form the output terminals.

Four of these zirconia cells and three thin plates of alumina (length: 34 mm, width: 3.4 mm, thickness: 0.2 mm) were stacked alternately, and were inserted into a quartz tube with a 4.5 mm internal diameter and a length of 38 mm, as shown in Fig. 1a. The alumina plateswere used as insulation between

the zirconia cells. The spacing between a zirconia cell and an alumina plate was approximate 0.1 mm. The wires from the cathodes were all linked together, as were the wires from the anodes, so that the voltage could be applied to the 4 cells in parallel. Silica wool was stuffed into both ends of the quartz tube.
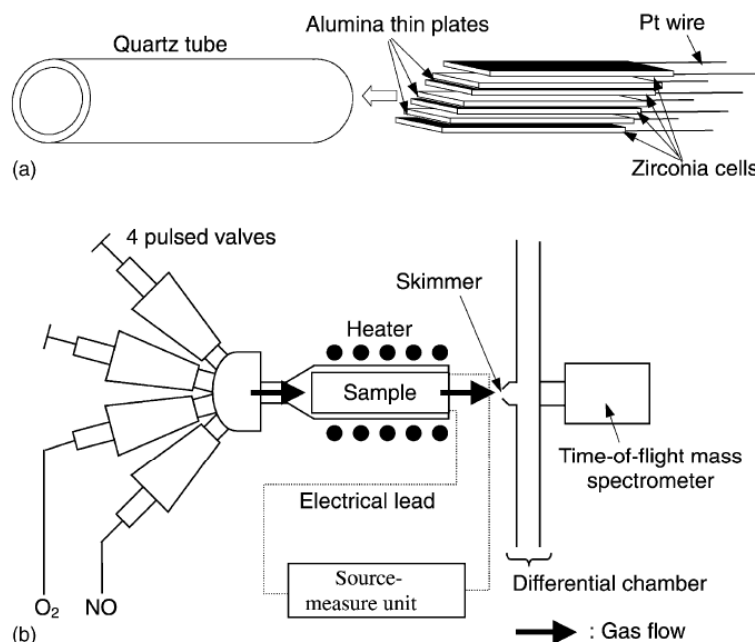
80

Fig. 1. Schematic drawings of (a) the alignment of zirconia cells and (b) measuring system for the electrochemical NO reduction.

Fig. 1b shows a simplified schematic diagram of the measuring system, which was equipped with four pulsed valves, two cryopumps and two turbopumps for differential chambers and a TOF-MS [10]. The quartz tube containing the zirconia cells was installed in this vacuum system, evacuated down to 5×10^{-7} Pa, and then heated by an external heater up to 973 K. The platinum wires from the zirconia cells were connected to a source-measure unit (Model 236, KEITHLEY). In this study, two of the pulsed valves were utilized. One was for the pulsed injection of NO and the other for the pulsed injection of O_2.

In a typical experiment, data from 30 operating cycles were accumulated to improve the S/N ratio. One cycle consisted of gas injection, re-evacuation, and the data acquisition process, which took no more than 5 s in total. The experimental flow of each cycle, which contained the Fig. 1. unique data acquisition and processing methods, was described in detail in a previous paper [11]. At the start of each cycle, the pulsed valve that controlled the flow of NO gas (1 kg/cm2) was actuated for 0.5 ms, and a resulting
narrow pulse of NO gas (about 0.2 cm3) was injected into the evacuated quartz tube containing the zirconia cells, onto which a constant voltage of between 0 V and 1 V was applied. The gas flow exiting the quartz tube was detected through the differential chambers by the TOF-MS, and the current across the cells was measured simultaneously. The system was pumped down again to the 5×10^{-7} level within 5 s in advance of the second cycle. After the 30 cycles were finished, the averaged data of the N_2 generation and the cell currents were determined as a function of time on a millisecond timescale. The resulting transient responses of the reacted gas and the cell currents reflect the kinetic process of the

electrochemical reduction of NO that occurred on the electrodes of the zirconia cells. In the experiment where a pulse of O_2 was injected, only the cell current was measured.

Since the distance between the cells and the ionization chamber of the mass spectrometer is approximate 15 cm, it takes several dozen microseconds for the reacted gases to get to the ionization chamber. The time of flight of the reacted gases from the cells to the chamber of the TOF-MS is negligible in the measurement of the mass spectra on the millisecond timescale.

7-3. Results and discussion

7.3.1. NO decomposition process on the Pt electrode

Simultaneous measurements of the N_2 gas generation and the cell currents corresponding to the NO pulse injections were carried out at 973 K in the cells with the Pt electrodes and in the cells with the Pt–Au electrodes. Measurements of the cell currents for the O_2 pulse injections were also carried out. The resulting time transient profiles are shown in Fig. 2. The cell currents do not start at zero just after the NO and O_2 pulse injections when a constant voltage was applied to the cell, as can be seen in Fig. 2b, c, e and f. This is because they are the averaged data from 30 cycles in which the cell currents do not decay back to zero.
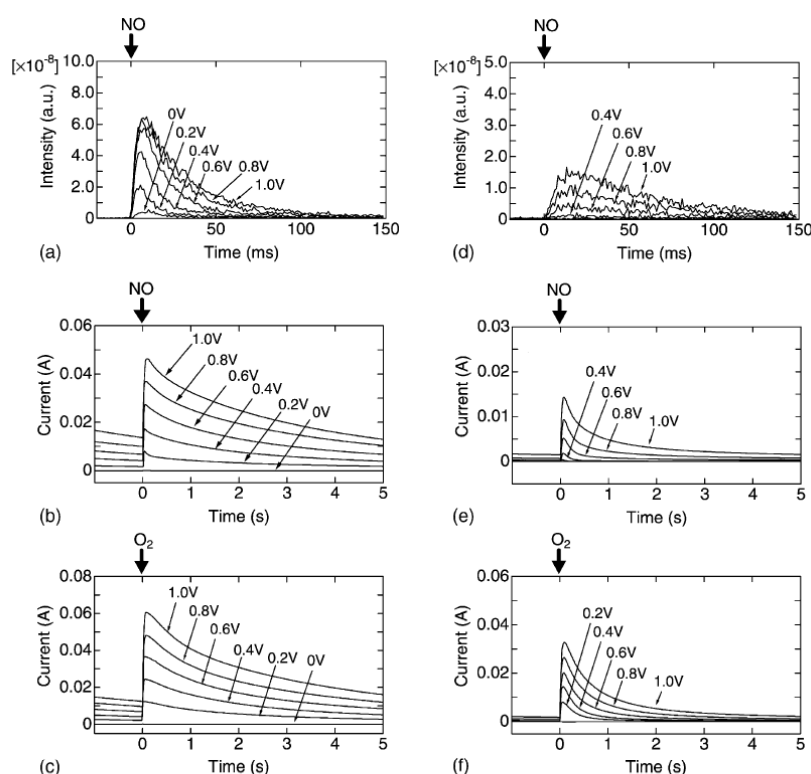
Fig. 2. Time profiles for N_2 generation (a, d) and cell currents (b, c, e, f) measured in the cells with the Pt electrodes (a–c) and in the cells with the Pt–Au electrodes (d–f) at 973 K, just after NO or O_2 pulse injections as indicated by the thick line arrows.

Firstly, we discuss the NO decomposition process on the Pt electrode on the basis of Fig. 2a, b, and c. In all of the experiments for the NO pulse injections, steep variations in the rate of N_2 generation and the cell current synchronized with the NO injection. It was found that the generation of N_2 associated with the electrochemical reduction of NO could be observed for no more than 150 ms after the NO pulse injection, while the decay of the cell currents could be observed for more than 5 s. To concretize the relationships between the transient profiles of the N_2 generation and the cell currents, the amount of N_2 that was generated, as derived from the integration of the corresponding transient profiles, was plotted as a function of the electric charge derived form the integration of the transient profile of the cell current, as shown in Fig. 3. It can be seen form Fig. 3 that the amount of generated N_2 is proportional to the electric charge, which means that the cell currents are attributed to the flux of oxide ions derived from the NO gas. The electrochemical NO reduction process is supposed to involve the dissociative adsorption of NO on the cathode surface, desorption of N_2 to the gas phase, diffusion of adsorbed oxygen atoms to the electrode/electrolyte boundary, and electrochemical reduction of the adsorbed oxygen atoms to oxide ions in the electrolyte [7]. The oxide ions are then transported through the solid electrolyte from the cathode to the anode. Here, the transient profile for the N_2 generation can be attributed to the process of dissociative current decay profile for the O_2 injection to that for the NO injection suggests that the time transient profiles of the cell currents for the NO injection can be attributed to the process of diffusion of the adsorbed oxygen atoms, their ionization to oxide ions, and transportation of the oxide ions from the cathode to the anode. The relationships between the transient profiles of the cell currents and the N_2 generation observed in this study reveal that the dissociative adsorption of NO and the N_2 desorption occur quite rapidly, followed by the gradual diffusion and ionization of the adsorbed oxygen atoms in the electrochemical reduction of NO. This is the first time that the process of electrochemical reduction of NO has been directly observed, being separated into the N_2 generation and the subsequent electrochemical reduction of the adsorbed oxygen atoms.

The generation of N_2 was enhanced by an increase in the applied voltages, but the above-mentioned NO reduction process was unchanged. The mechanism for the enhancement of N_2 generation with increasing applied voltage is   discussed in a later section.
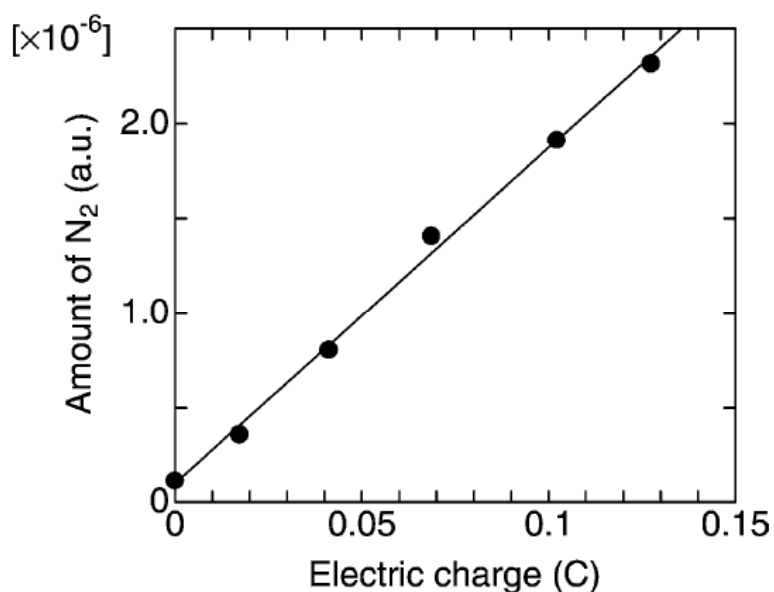
Fig. 3. Dependency of the amount of N$_2$ generated on the electric charge.

7.3.2. Effect on NO decomposition of the addition of Au to the Pt electrode

The amount of N$_2$ that was generated is shown in Fig. 4 as a function of the applied voltage. It can be seen from Fig. 4 that the capability for the electrochemical reduction of NO lowered on the Pt–Au electrode, compared with the capability on the Pt electrode when the applied voltage was between 0 V and 1 V. However, it is remarkable that the process of the electrochemical reduction of NO, in which the gradual reduction of the adsorbed oxygen atoms follows the N$_2$ desorption, was unchanged on the Pt–Au electrode, as seen from Fig. 2d and e. Although the oxygen pumping capability was also lowered on the Pt–Au electrode, as seen from a comparison between Fig. 2c and f, the degree of lowering was much larger in the electrochemical reduction of NO especially at the applied voltages below 0.4 V where the first cell of the mulit-electrode type NOx sensor was operated for the preferential oxygen pumping.
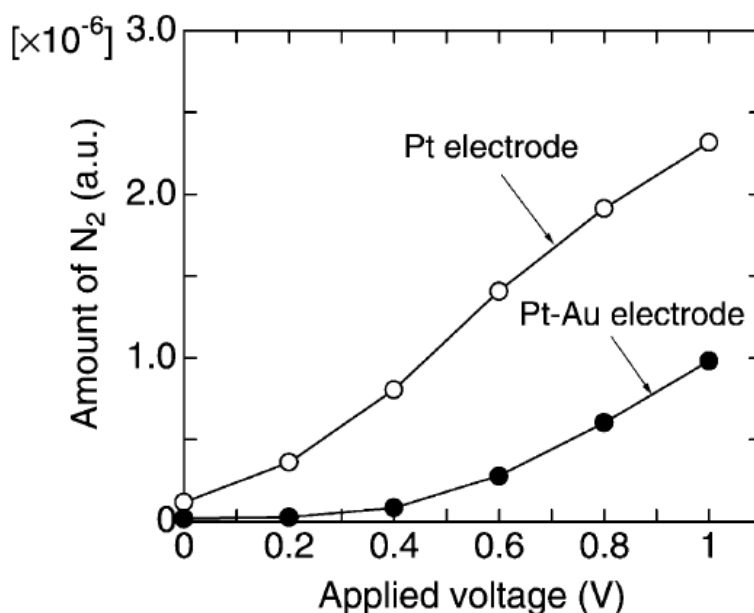
Fig. 4. Dependency of the amount of N_2 generated on the applied voltage.

On the basis of these results, we discuss the mechanisms for the decrease in the NO decomposition capability and for the preferential pumping of oxygen. It is well known that Au metal has a poorer affinity for oxygen than that of Pt metal. Therefore, the addition of Au to the Pt electrode results in a lowering of the affinity for oxygen of the Pt electrode, which is supported by the fact that the cell currents decayed faster on the Pt–Au electrode, as shown in Fig. 2e and f. The decrease in the affinity for oxygen causes a decrease in the available surface area where O_2 or NO can absorb dissociatively, which is suggested to be the cause of the decrease in both the oxygen pumping capability and the capability for electrochemical NO reduction.

To confirm the influence of lowering the affinity for oxygen on the rate of dissociative NO adsorption, free from the influence of the amount of N_2 generation, the time profiles for the N_2 generation and the cell currents were compared between the Pt and P–Au electrodes under conditions where the amount of N_2 generated on each electrode was comparable. Fig. 5 shows a comparison of the time transient profiles measured in between the cells with the Pt electrodes at an applied voltage of 0.2 V and the cells with the Pt–Au electrodes at an applied voltage of 0.8 V. The rate of N_2 generation on the Pt–Au alloy electrode was slower than that on the Pt electrode, despite the fact that larger amounts of N_2 were generated in the cells with Pt–Au electrodes under those conditions. In addition, N_2 continued to be generated for longer on the Pt–Au electrode. This finding shows that the rate of dissociative adsorption of NO decreases on the Pt–Au electrode. Since the decrease in the rate of diffusion and ionization of the adsorbed oxygen atoms is common to both the oxygen

85

pumping capability and the electrochemical NO reduction capability, it is suggested that the decrease in the rate of dissociative NO adsorption is the main reason for the preferential pumping of oxygen at the applied voltages below 0.4 V.
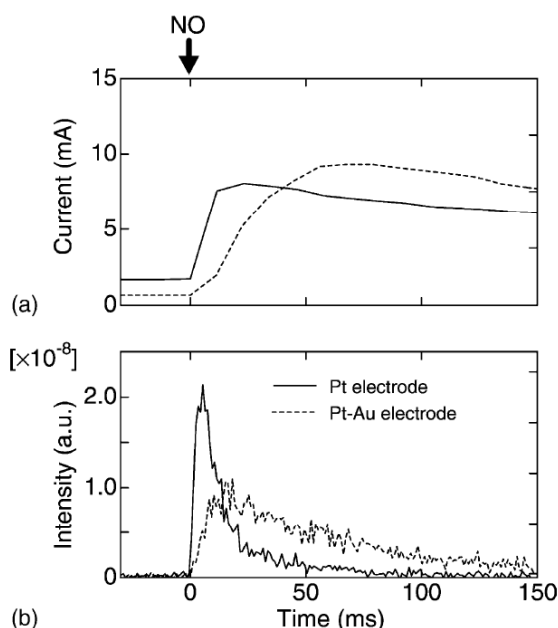

Fig. 5. Comparison of time profiles for (a) cell currents and (b) N_2 generation between zirconia cells with the Pt electrodes at an applied voltage of 0.2 V and those with the Pt–Au electrodes at an applied voltage of 0.8 V.

7.3.3. Effect of applied voltage on NO decomposition

As the applied voltage was raised, the amount of N_2 that was generated progressively increased on both the Pt and the Pt–Au electrodes, as shown in Fig. 4. Here, we discuss a possible mechanism to explain this result. The increase in the decomposition of NO with increasing applied voltage suggests the following two possibilities. Firstly, the more rapid progress of the electrochemical reduction of the adsorbed oxygen atoms at the higher applied voltage could produce a larger available electrode surface free of adsorbed oxygen, where the NO can adsorb dissociatively. Secondly, the breaking of the N–O bond of the NO could be assisted by an electric field on the cathodic polarised electrode. To distinguish experimentally between these two possibilities, the dependency of the amount of N_2 generated on the temperature was investigated. The results are shown in Fig. 6. The slopes of the logarithm of the amount of N_2 generated versus 1/T were almost constant, irrespective of the values of the applied voltages for both electrodes. This finding indicates that the value of the applied voltage does not affect the activation energy for NO dissociation but does affect the frequency factor of the reaction. Here, the frequency factor of the reaction can be interpreted as the requency of encounters between the available surface area free of adsorbed oxygen atoms and the NO. The fact that the activation energy is not affected by the value of the applied voltage

excludes the second possibility mentioned above. Therefore, it was concluded that the increase in the available surface area by the effective electrochemical reduction of the adsorbed oxygen atoms enhances the capability for the electrochemical decomposition of NO at high applied voltages.

Fig. 6 also provides significant information on the effects of the electrode species. The activation energies for N_2 generation were estimated from Fig. 6 as 58 kJ/mol (0.6 eV) for the Pt–Au electrode and 24 kJ/mol (0.25 eV) for the Pt electrode, respectively. These values are reasonable in magnitude when compared with the value of 55.7 kJ/ mol on Pt foil reported by Amirnazmi and Boudart [13]. It is suggested that this increase in activation energy results in the decrease in the rate of N_2 generation mentioned in the previous section.
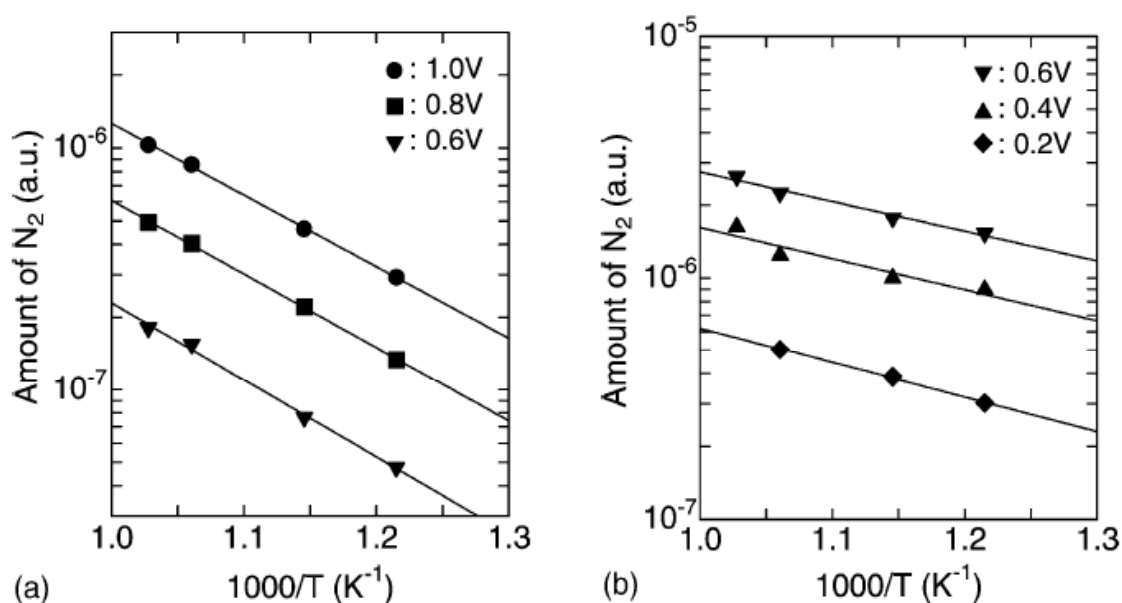
Fig.6. Temperature dependence of the amount of N_2 generated (a) on the Pt–Au electrode and (b) on the Pt electrode.

As mentioned above, the addition of Au to the Pt electrode causes a decrease in the surface area available for the dissociative adsorption of NO or O_2 and an increase in the activation energy for the dissociation of NO. The former affects both the oxygen pumping capability and the electrochemical NO reduction capability to the same degree, and the latter lowers the electrochemical NO reduction capability, which enables selective oxygen pumping on the Pt–Au electrode.

7.3.4. Influence of O_2 on NO decomposition
Fig. 7 presents the results of the pulsed injections of O_2 followed by pulsed injections of NO into the cells with the Pt electrodes and the Pt–Au electrodes respectively at 973 K.

The intervals between the pulsed injections of O_2 and NO were varied from 300 ms to 900 ms at an applied voltage of 0.4 V. The time profiles for the N_2 generation were drawn up based on the timing of the NO pulse injections, while the profiles for the cell currents were based on the timing of the O_2 pulse injections. When the interval between the pulse injections was longer, increased N_2 generation could be observed on the Pt electrode. This finding indicates that an area on the electrode surface free of adsorbed oxygen atoms is required for NO decomposition. This result agrees with the fact that the NO decomposes after the oxygen pumping is completed, which was reported by Hibino et al.[8]. On the other hand, only a small amount of N_2 was generated on the Pt–Au electrode, even at an interval of 900 ms, which directly indicates the preferential oxygen pumping in the cells with the Pt–Au electrodes.
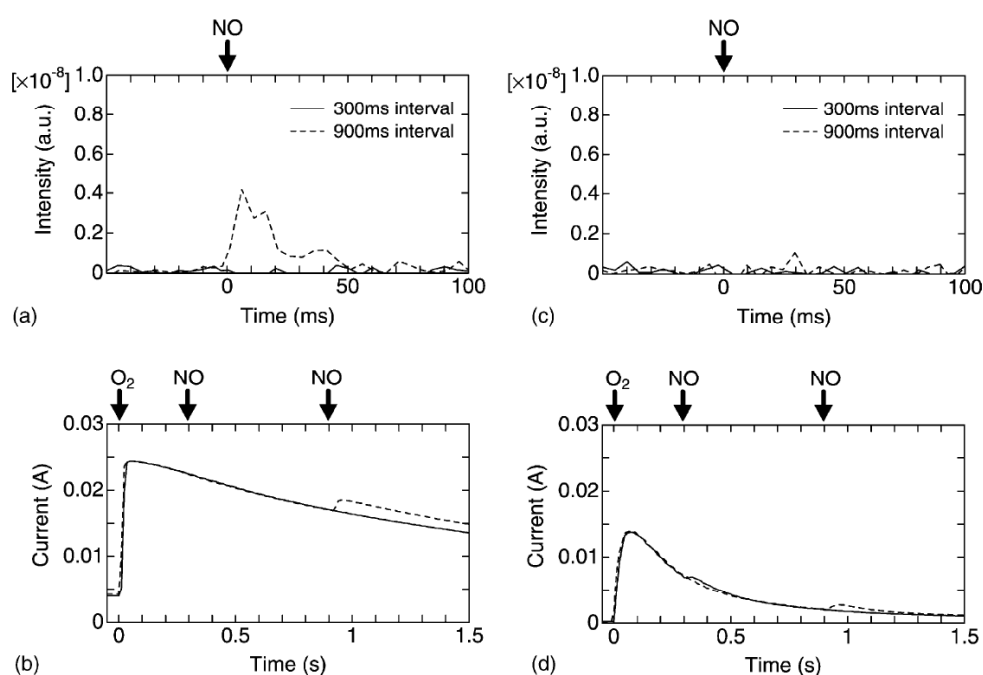

Fig. 7. Time profiles for N_2 generation (a, c) and cell currents (b, d) measured in the cells with the Pt electrodes (a, b) and in the cells with the Pt–Au electrodes (c, d) at the applied voltage of 0.4 V at 973 K, which were triggered by sequential pulse injections of O2 and NO as indicated by the thick line arrows.

7.4. Conclusion

The mechanism for the electrochemical reduction of NO on noble metal electrodes was discussed on the basis of simultaneous measurements of N_2 generation and cell currents corresponding to NO pulse injections on a millisecond timescale. It was clarified that the electrochemical reduction of NO proceeds as follows, regardless of the electrode species. Initially, the dissociative adsorption of NO on the electrode and the desorption of N_2 to the gas phase occur quite rapidly, followed by the gradual diffusion and ionization of the adsorbed oxygen atoms. The rate of NO decomposition on the Pt–Au alloy electrode was much slower than that on the Pt electrode. From an estimation of the activation energies

88

for N_2 generation, it was concluded that a decrease in the rate of dissociative adsorption of NO due to an increase in the activation energy for NO dissociation enabled the preferential pumping of oxygen on the Pt–Au electrode.

References

[1] N. Kato, K. Nakagaki, N. Ina, Thick film ZrO_2 NOx sensor, SAE paper (1996) 960334.

[2] N. Kato, Y. Hamada, H. Kurachi, Performance of thick film NOx sensor on diesel and gasoline engines, SAE paper (1997) 970858.

[3] S. Somov, G. Reinhardt, U. Guth, W. Go¨pel, Gas analysis with arrays of solid state electrochemical sensors: implications to monitor HCs and NOx in exhaust, Sens. Actuators B 35-36 (1996) 409–418.

[4] S. Somov, G. Reinhardt, U. Guth, W. Go¨pel, Tubular amperometric high-temperature sensors: simultaneous determination of oxygen, nitrogen oxides and combustible components, Sens. Actuators B 65(2000) 68–69.

[5] G. Reinhardt, I. Rohlfs, R. Mayer, W. Go¨pel, Selectivity-optimization of planar amperometric multi-electrode sensors: identification of O_2, NOx and combustible gases in exhausts at high temperatures, Sens. Actuators B 65 (2000) 76–78.

[6] T. Hibino, K. Ushiki, Y. Kuwahara, Electrochemical oxygen pump using CeO_2-based solid electrolyte for NOx detection independent of O_2 concentration, Solid State Ionics 93 (1997) 309–314.

[7] K.J. Walsh, P.S. Fedkiw, Nitric oxide reduction using platinum electrodes on yttria-stabilized zirconia, Solid State Ionics 93 (1997)17–31.

[8] T. Hibino, K. Ushiki, Y. Kuwahara, Mechanism of NO decomposition in a solid electrolyte reactor by SEP method, Solid State Ionics 98 (1997) 185–190.

[9] K.J. Walsh, P.S. Fedkiw, Nitric oxide reduction using iridium electrodes on yttria-stabilized zirconia, Solid State Ionics 104 (1997)97–108.

[10] T. Motohiro, Y. Kizaki, Y. Sakamoto, K. Higuchi, Y. Watanabe, S.Noda, Time-resolved time-of-flight mass spectrometry with molecular- pulse-probes for analysis of dynamic process in surface catalytic reactions in millisecond range (I), Appl. Surf. Sci. 121/122 (1997) 319–322.

[11] T. Motohiro, Y. Kizaki, Y. Sakamoto, K. Higuchi, T. Tanabe, N. Takahashi, K. Yokota, H. Doi, M. Sugiura, S. Noda, Timeresolved time-of-flight mass spectrometry with molecular-pulseprobes for analysis of dynamic process in surface catalytic reactions in millisecond range (II), Appl. Surf. Sci. 121/122 (1997) 323–326.

[12] S.O. Shekhtman, G.S. Yablonsky, S. Chen, J.T. Gleaves, Thin-zone TAP-reactor—theory and application, Chem. Eng. Sci. 54 (1999) 4371–4378.

[13] A. Amirnazmi, M. Boudart, Decomposition of nitric oxide on platinum, J. Catal. 39 (1975) 383–394.

Chapter 8.   Summary and general conclusion

8-1 Summary

  This thesis describes the transient reaction analysis for automotive catalysts using a newly developed apparatus called TM+ and flat model catalysts. The transient reaction analysis is enormously complex from the view both of material and reaction. This thesis provides some suitable method for the analysis to simplify material and reaction.

  Chapter 1 mentions the general introduction of this thesis. Some reasons why the transient reaction for automotive catalysts is so complicated were shown. The motivation for developing the newly developed apparatus called TM+ is also shown.

  Chapter 2 shows the design and construction of new apparatus. This new apparatus can detect transient reaction products from small surface area samples such as film catalysts to real catalysts with high surface area on the millisecond range resolution. It is also more robust and tolerant for dynamic changes of vacuum conditions than the conventional UHV surface science apparatus.

  Chapter 3 deals with the evaluation of oxygen release from Pt/CeO_2 catalyst. The new measurement method for OSC was proposed to evaluate the MS-OSC of oxygen release on a millisecond time scale. This result is consistent with a previous engine test results, which could not be explained by the conventional OSC measurement results.

  Chapter 4 demonstrates the transient analysis of the release and reduction of NOx using a $Pt/Ba/Al_2O_3$ catalyst. As a result of NOx regeneration, NO, N_2, NH_3 and H_2O, were detected from a flat 5 $nmPt/Ba(NO_3)_2/$cordierite catalyst, though no products were detected from $Ba(NO_3)_2/$cordierite. It was found that Pt plays an important role in the NSR reaction and that NO was produced from decomposition of $Ba(NO_3)_2$ in the catalyst. In this experiment, a TAP type reactor was introduced for the transient reaction analysis. NOx regeneration in an NSR catalyst with H_2 gas was investigated on a millisecond time scale. We can analyze the NOx regeneration process to separate two steps of the NOx release and reduction by a detailed analysis of the time profiles using a two-step reaction model.

  Chapter 5 presents discussion about the effect of precious metals and NOx storage materials on hydrogen reduction of stored NOx. The effect of precious metals (PMs) and NOx storage materials (NSMs) on the reduction of stored NOx over $PM/NSM/Al_2O_3$ (PM = Pt, Rh, Pd; NSM = Ba, K, Na) catalysts was studied via transient reaction analysis using pulsed gases with submillisecond resolution. The time profiles of the product gases were analyzed with a high time resolution of 0.25 ms for the first 50 ms after supplying a hydrogen gas pulse. These results were explained with a model that correlates with the spillovers of

released NOx species from the NSM and the activated hydrogen on the PM. The catalyst Pt/Na/Al$_2$O$_3$ had the highest reduction rate of stored NOx among the nine catalysts examined.

Chapter 6 reveals the analysis for adsorption and desorption of NOx and SOx using a flat model catalyst. Thin film was designed as a NOx storage catalyst and investigated with respect to NOx and SOx adsorption/desorption using EPMA, AES, XPS, and EELS. NOx and SOx were adsorbed all over the model catalyst; however, NOx desorption occurred preferentially in an area a few micrometers around the platinum and was suppressed at all other sites, whereas SOx desorption occurred preferentially in a few nanometers wide area around the platinum. The visualization for adsorption and desorption of NOx and SOx demonstrated here would be helpful to design high performance NSR catalysts with high NSR reaction and endurance for SOx poisoning.

Chapter 7 concerns with NOx decomposition on a Pt–Au electrode of amperometric NOx sensor. Our analysis clarified the mechanism of the electrochemical reduction of NO on a Pt electrode. The dissociative adsorption of NO on the electrode and the desorption of N$_2$ to the gas phase occur quite rapidly, followed by the gradual ionization of the adsorbed oxygen atoms. The same reaction process could be observed on a Pt–Au electrode, except that the rate of N$_2$ generation on the Pt–Au electrode was slower than that on the Pt electrode. From an estimation of the activation energies for N$_2$ generation, it was concluded that an increase in the activation energy for NO dissociation enables the preferential oxygen pumping on the Pt–Au electrode. The high sensitivity of TM+ enabled us to analyze the electrode reaction with low surface area, and the high time response of TM+ can elucidate current flow and time profile of products as surface reaction.

8-2 Characteristic of TM+

Below is a table that compares TM+ with some of other analysis methods for transient reactions analysis. It is true that TM+ and Temporal Analysis of Product (TAP) can also analyze the transient reaction of real catalysts such as metal dispersed catalysts. However there are some differences among them.

Table 1 Comparison of apparatus for transient reaction analysis.

	Molecular Beam Scattering (MBE)	Temporal Analysis of Product (TAP)	TM+ (this apparatus)
reactant gas source (amount of gas per msec)	ultra sonic molecular beam source (very small 10^{-12} moles)	Pulsed valve (large 10^{-10} moles)	Pulsed valve (huge $10^{-10} - 10^{-12}$ moles)
pumping system of reaction chamber (method)	static (Ion pump, Liquid nitrogen shroud)	dynamic (Oil diffusion pump)	dynamic (cryopump)
differential pumping system	three stage for gas source	two stage for mass spectroscopy	two stage for mass spectroscopy
Sample type	flat	tube	flat and tube
type of mass spectroscopy	quadrupole mass spectrometer	quadrupole mass spectrometer	time-of-flight mass spectrometry

There are three enormous differences among these methods as follows;

(1) Time resolution for detection of each component

It is impossible for a quadrupole mass spectrometer (QMASS) to detect several kinds of mass species with mille second time resolution. It may be possible to detect only one kind of mass with mille second time resolution. On the other hand, time-of-flight mass spectrometry (TOFMASS) can detect many kinds of mass species, for examples, from 0 to 150 mass within about $20\,\mu$ sec. The time resolution can be upgrade to $100\,\mu$ sec even considering the extra time for signal detection, data analyzing, and ionization repetition rate. The higher time resolution of TM+ is a large advantage. According to this advantage, an installation of TOFMASS to TAP has been started very recently in 2011 [3].

(2) Available type of samples

TM+ can treat both types of sample forms, flat and tube type. The strong adsorbents, such as H_2O and CO_2, are often difficult to measure due to the strong adsorption on catalysts with large surface areas and micro pores. This difficulty becomes conspicuous when using a tube type reactor.   TM+ using flat type samples can measure products of strong adsorbents while decreasing the difficulty.

(3) Partial pressure of the catalyst surface

Because of the high sensitivity and tolerance for high pressure, TM+ covers the meaningful area for the research and development of automotive catalyst as shown in Figure 1, where the pressure is the peak value when pulsed gases are supplied to the catalyst surface. MBE makes only the lower partial pressure of the catalyst surface nevertheless they achieve high sensitive measurement. TAP can create high partial pressure however it shows the lower sensitivity. The pressure of TM+ about 10 Pa corresponds approximately to a few hundreds ppm that is the same order of the harmful component concentration involving automotive exhausts gases.

From above considerations, it is found that TM+ is a very unique method to evaluate the catalysis reaction occurred on real automotive catalyst under the real usage condition with sufficient time resolution corresponding to fluctuations of engine emissions.
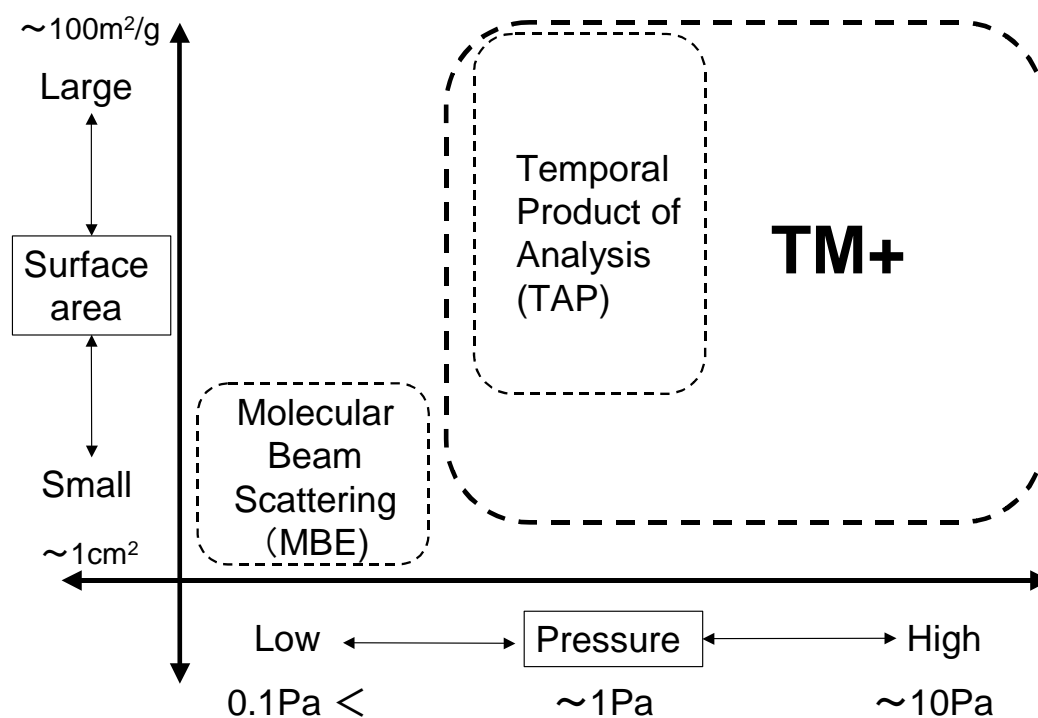

Figure 1 Comparison between catalysis reaction analysis.

8-3 General conclusion

We developed the world's first successful apparatus named TM+, which was specially designed to detect multi products of catalytic reactions on the millisecond time scale under atmospheric pressure. The component of automotive exhaust gas is fatefully and always fluctuated on the millisecond time scale by the active and/or passive engine control. TM+ can emulate such a fast fluctuation and make it possible to track the unsteady automotive catalytic reactions on the millisecond time scale, since TM+ intelligently composed of hardware such as the pulse valves, the cryopumps, the two types of sample holders, and the time of flight mass spectrometer, and software to manage the combination of the complicated parts as a whole apparatus system and huge number of data acquisition and analysis.

This millisecond time resolution of TM+ gave us some important insights of the unsteady reaction rates, for example, (i) the oxygen storage and release rate in the three way catalysts, and (ii) the rate of the nitrogenous production caused by a millisecond reducing gas spike in the NOx storage and reduction catalysts, which provide us more precise understanding of the catalysis. These results have never been obtained by any conventional methodologies. It should be notable that the development of TM+ with the present new concept and function enabled us to find out a new material design and a new reaction pass beyond the thermodynamic equilibrium limitation. The most significant contribution of this thesis would be the clear and successful demonstration that the utilization of the TM+ aids us to understand the "actual nature of catalysis" even if the multifarious complicated reactions are mixed up in the "real world".

8-4 Perspectives

Some transient reactions concerning automotive catalysis were understood in this thesis. Here, we will present next challenges to improve our analysis as follows.

1. Numerical kinetic analysis

Chapter 3 shows the possibility for direct evaluation of OSC release rate. E. V. Kondratenko et al. investigated the oxygen release rate using original TAP instead of TM+ flat type reactor [1,2]. They measured CO_2 production profiles of the same samples shown in Chapter 3. It was difficult to evaluating directly the OSC release rate as CO_2 production amount because of the strong adsorption of CO_2 on CeO_2. As a result of considerations, they proposed a new indicator to evaluate the OSC release rate as the peak position of CO_2 production profile. However the TAP analysis rate has not yet led to evaluate the OSC release rate directly and quantitatively.

K. Okumura et al. have already made a numerical kinetic analysis for $NO+H_2$ reaction using TM+ [3](Figure 2). Though they applied the numerical kinetic analysis only for simple film type catalysts, it was applied both for flat type and TAP type reactor. By applying and evaluate this numerical kinetic analysis for powder catalysts, it will permit the numerical evaluation of the OSC release rate.
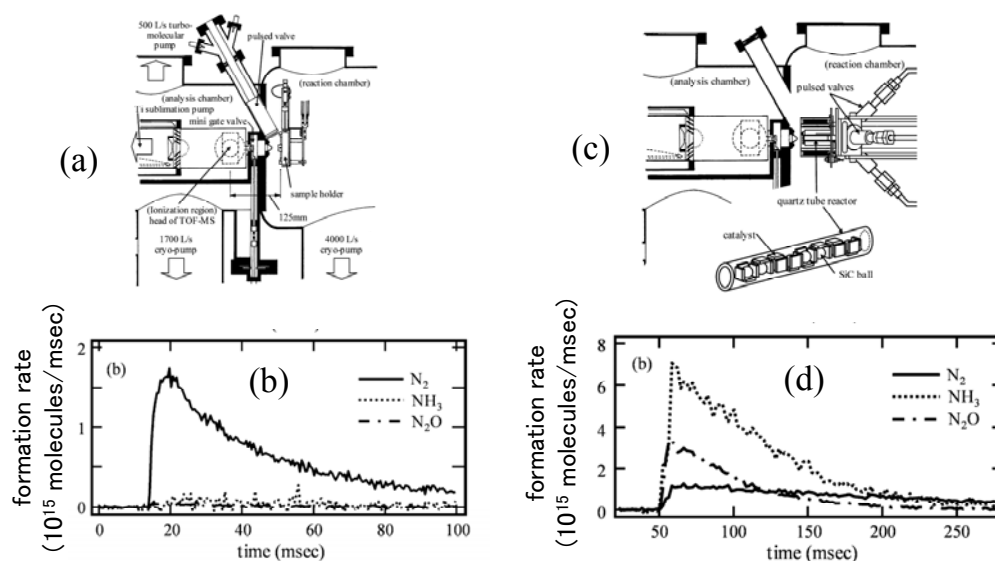

Figure 2 Reactors and $NO+H_2$ reaction analysis for Pt-Al_2O_3 thin film on Si substrate. (a)flat type reactor, (c)TAP type reactor and (c), (d) their reaction products at 400°C[4].

2. The combination with surface or bulk state analysis at high pressure

It is possible to obtain fruitful knowledge by investigating the surface condition of the active catalytic site by monitoring the both reactants and products simultaneously. The shape of the planar catalyst of TM+ will be adequate for the surface analysis method, such as sum of frequency generation spectroscopy (SFG), infrared reflection absorption spectroscopy (IRAS) and ultraviolet photoemission spectroscopy (UPS).

3.Water effect

The automotive exhaust gas contains 10-20 % of water. The water is related strongly to reactions in automotive catalysts. The influence of water should be investigated if we want to utilize newly-discovered catalyst and catalysis for automotive exhaust purifications. However water is usually incompatible with ultra high vacuum systems, it may be possible to coordinate the system with the conditions involving water by improvement of the apparatus such as heating chambers and water traps.

At last we would like to attempt a bird's-eye view of developing newly-discovered catalysis for automotives. Model catalysts have developed from single crystal to integrated catalysts that are sophisticated by a lithography technology [5-7]. On the other hands, real catalysts for automotive exhaust gas were improved to three-way catalyst. It will be difficult that only three-way catalyst overcomes future strict regulations for automotive emission, especially diesel engine emission. It is necessary to utilize new catalysis using transient reaction such as NOx storage and release, ammonia selective reduction and particulates molecule oxidation. Combining new transient reaction analysis of TM+ with new type model catalyst of integrated catalyst will develop sophisticated catalysts.
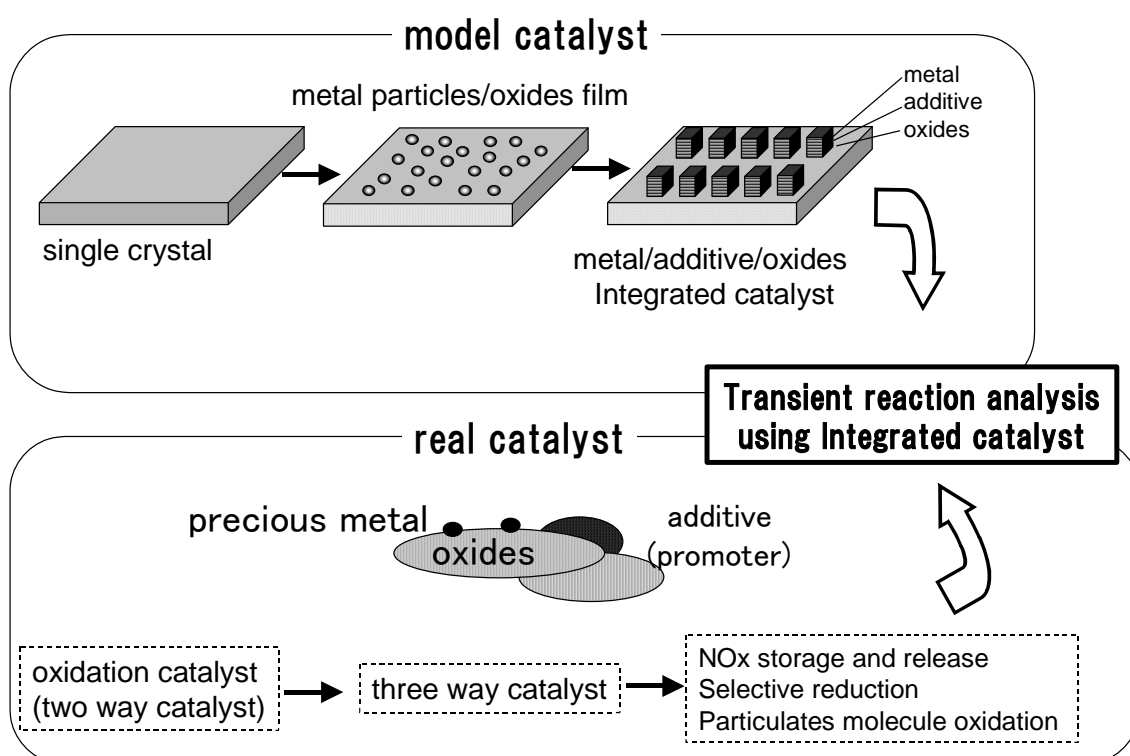

Figure 3 Future strategy for designing new catalysis.

[1] E. V. Kondratenko, Y. Sakamoto, K. Okumura, H. Shinjoh, Catalysis Today 164 (2011) 46.

[2] E. V. Kondratenko, Y. Sakamoto, K. Okumura, H. Shinjoh, Applied Catal. B, 89 (2009) 476.

[3] A. Goguet, C. Hardacre, N. Maguire, K. Morgan, S. O. Shekhtman, S. P. Thompson, 136Analyst(2011)155.

[4] K. Okumura, T. Motohiro, Y. Sakamoto, T. Kayama, Y. Kizaki, H. Shinjoh, Applied Catalysis A: General 354 (2009) 111.

[5I. Zuburtikudis and H. Saltsbulg, Science, 258(1992)1338.

[6]A. Katoh, the llth surf. Sci. Seminar Text, pp. 26-28,Surf. Sci. Soc. Jpn., June ,1991, Tokyo.

[7] S. Suzuki, Y. Ohminami and K. Asakura, Petrotec, 26, (2003)206.

Publication list

Chapter 2 Design and construction of a new apparatus

[1] Time-resolved time-of-flight mass spectrometry with molecular-pulse-probes for analysis of dynamic process in surface catalytic reactions in the millisecond range (I), Applied Surface Science, Volumes 121-122, 2 November 1997, Pages 319-322, T. Motohiro, Y. Kizaki, Y. Sakamoto, K. Higuchi, Y. Watanabe, S. Noda

[2] Time-resolved time-of-flight mass spectrometry with molecular-pulse-probes for analysis of dynamic process in surface catalytic reactions in millisecond range (II), Applied Surface Science, Volumes 121-122, 2 November 1997, Pages 323-326,T. Motohiro, Y. Kizaki, Y. Sakamoto, K. Higuchi, T. Tanabe, N. Takahashi, K. Yokota, H. Doi, M. Sugiura, S. Noda

Chapter 3 Evaluation of oxygen release from Pt/CeO_2 catalyst

[3] New Method of Measuring the Amount of Oxygen Storage/Release on Millisecond Time Scale on Planar Catalyst,Journal of Catalysis, Volume 211, Issue 1, 1 October 2002, Pages 157-164, Y. Sakamoto, K. Kizaki, T. Motohiro, Y. Yokota, H. Sobukawa, M. Uenishi, H. Tanaka, M. Sugiura

Chapter 4 NOx release reaction analysis

[4] Transient analysis of the release and reduction of NOx using a $Pt/Ba/Al_2O_3$ catalyst, Catalysis Today, Volume 121, Issues 3-4, 30 March 2007, Pages 217-225, Y. Sakamoto, T. Motohiro, S. Matsunaga, K. Okumura, T. Kayama, K. Yamazaki, T. Tanaka, Y. Kizaki, Naoki Takahashi, H.i Shinjoh

Chapter 5 NOx release reaction analysis

[5] Comparison between the NOx release–reduction reaction for $Pt/Ba/Al_2O_3$ and $Pt/K/Al_2O_3$ on a millisecond time scale, Chemical Engineering Science, Volume 63, Issue 20, October 2008, Pages 5028-5034, Y. Sakamoto, S. Matsunaga, K. Okumura, T. Kayama, K. Yamazaki, N. Takahashi, T. Tanaka, Y. Kizaki, T. Motohiro, H. Shinjoh.

[6] Effect of precious metals and NOx storage materials on hydrogen reduction of stored NOx on millisecond time scale, Volume 445–446, 11 August 2012, Pages 133–142, Applied Catalysis;A   Y. Sakamoto, S. Matsunaga, K. Okumura, T. Kayama, K. Yamazaki, N. Takahashi, T. Tanaka, Y. Kizaki, T. Motohiro, and H. Shinjoh.

Chapter 6 Analysis for adsorption and desorption of NOx and SOx using a flat model catalyst

[7] Adsorption and desorption analysis of NOx and SOx on a Pt/Ba thin film model catalyst, Journal of Catalysis, Volume 238, Issue 2, 10 March 2006, Pages 361-368, Y. Sakamoto, K. Okumura, Y. Kizaki, S. Matsunaga, N. Takahashi, H. Shinjoh.

[8] NOx decomposition mechanism on the electrodes of a zirconia-based amperometric NOx sensor, Sensors and Actuators B: Chemical, Volume 93, Issues 1-3, 1 August 2003, Pages 214-220, T. Nakamura, Y. Sakamoto, K. Saji, J. Sakata

Related papers

[1]Time-resolved in situ UV/vis spectroscopy for analyzing the dynamics of surface and bulk redox processes in materials used as oxygen storage capacitors, Catalysis Today, Volume 164, Issues 1, 1 April 2011, Pages 46-51, K. V. Evgenii, Y. Sakamoto, K. Okumura, H. Shinjoh.

[2]Transient analysis of oxygen storage capacity of Pt/CeO_2-ZrO_2 materials with millisecond- and second-time resolution, Applied Catalysis B, Volume 89, Issues 3-4, 1 July 2009, Pages 476-483, K. V. Evgenii, Y. Sakamoto, K. Okumura, H. Shinjoh.

Related book

Trends in Catalysis Research(Editors: Lawrence P. Bevy, Nova Science Publishers),
Chapter 6. Transient Reaction Analysis of an Automotive Catalyst on a Millisecond Time Scale; pp. 191-220, (Yoshiyuki Sakamoto and Tomoyoshi Motohiro et al., Toyota Central R&D Labs. Inc., Japan) Pub. Date: 2005,   ISBN: 1-59454-659-2.

Related presentation

[1]Int. Symp. Surf. Nano-Control Environ. Catal. Relat. Mater., Tokyo, (Spons. by Surf. Sci. Soc. Jpn.), 25/11/1996, "Time-Resolved Time-of-Flight Mass Spectrometry with Molecular-Pulse-Probes for Analysis of Dynamic Process in Surface Catalytic Reactions in Milisecond Range (II)".

[2]220th ACS Nat. Meet., Washington, D.C.,   20/08/2000, "OSC Measurement of Pt/Ceria Catalyst in Millisecond Time Range".

[3]International Conference on Unsteady-State Processes in Catalysis (USPC-4), 26/10/2003, "Direct Evolution of Oxygen Storage/Release Capacity on Millisecond Time Scale".

[4]5th Int. Conf. on Unsteady-state Processes in Catal. (USPC-5), 12/22/2006, "Comparison between the NOx Release-reduction Reaction for $Pt/Ba/Al_2O_3$ and $Pt/K/Al_2O_3$ on a Millisecond Time Scale".